UNIVERSITY OF CALIFORNIA, SAN DIEGO

Frequency Tunable Antennas and Novel Phased Array Feeding Networks for Next Generation Communication Systems

A dissertation submitted in partial satisfaction of the
requirements for the degree
Doctor of Philosophy

in

Electrical Engineering (Electronic Circuits and Systems)

by

Bilgehan Avser

Committee in charge:

Professor Gabriel M. Rebeiz, Chair
Professor Gert Cauwenberghs
Professor William Hodgkiss
Professor Vitaliy Lomakin
Professor Daniel Sievenpiper

2015

The dissertation of Bilgehan Avser is approved, and it is acceptable in quality and form for publication on microfilm and electronically:

_____

_____

_____

_____

_____

Chair

University of California, San Diego

2015

DEDICATION

To my mother and father,
who sacrificed a lot so that I can have a better life.

EPIGRAPH

The beautiful thing about learning is nobody can take it away from you.

—B.B. King

TABLE OF CONTENTS

LIST OF FIGURES

LIST OF TABLES

ACKNOWLEDGEMENTS

This thesis would not be possible without the help and support of many people. I would like to take this opportunity to thank them.

I remember my first weekly meeting at the TICS group with Professor Rebeiz. We were all sitting around the large table at our sixth floor office. As usual, other members of the group presented the work they had done the past week as well as the scheduled work for the present week. I was sitting on the far end of the table from Prof. Rebeiz, anxiously listening to other people present while holding the slides that I had spent the weekend preparing. I was feeling lost since I didn't understand most of the material being discussed and also was very nervous as to whether Prof. Rebeiz would like the work that I had done. When it was finally my turn, he called my name and I moved to the chair on his right. He looked at the slides and from the look on his face I could tell he was not happy. The scales were off, the fonts were too small, and there were too many graphs. I felt terrible. I remember coming home that day and wondering whether I was going to be able to do this for the next five years of my life. But after a couple of hours, I looked at the slides again. I realized that Prof. Rebeiz was right about everything. The scales were unnecessarily large, the fonts were too small, and most of the simulations were redundant. I spent the next week working harder. This time at the meeting there was less criticism. As I joined more meetings, I started to understand much more of what was going on at the table. I even started to comment on and contribute to other peoples projects. My slides got a lot better, there was less criticism and more jokes and funny stories. The weekly meetings at TICS group were the times that I learned the most. It was a privilege to observe Prof. Rebeiz solving problems and I learned a lot from him, not only about engineering but also about business, management, and family. I will truly miss working with him. But I know when I encounter a problem too hard to tackle on my own, he will be more than happy to share his experience with me.

I would also like to thank my dissertation committee members, Prof. Gert Cauwenberghs, Prof. William Hodgkiss, Prof. Vitaliy Lomakin and Prof. Daniel Sievenpiper and my co-authors Richard Frazita and John Pierro for their time, interest, and valuable comments about my research.

Additionally, I would like to thank Prof. Vakur B. Erturk for his guidance. When I met him, I was a sophomore enrolled in his linear algebra and differential equations course at Bilkent University. I was very inspired by one of his lectures and asked him if I could work with him on a research project. That project sparked my interest in electromagnetics and eventually

led me to pursue a PhD in this field.

One of the hardest parts of my graduate studies was adjusting to living in a country on the opposite side of the world from my home. There were lonely and desperate times but my friends were there to help me. I met Brandon Nichols and Masoud Jalali at my first week at San Diego. Since then, we have shared a lot of happy moments and a few sad ones. Our drunken late night cooking and multiple failed start-up projects are some of my most precious memories at UCSD. I also would like to thank Karen Nichols, Brandon's mom, for letting us spend the Thanksgiving holiday of 2011 at her home. Holidays are the toughest times for foreign students, and her kind gesture made us feel at home that day. I also would like to thank the White family for always making me feel at home at their place. Especially to Sandy and Alan White for all of their help during my move to San Diego.

I would like to thank Ozan Dogan Gurbuz for the discussions about strange problems that we came up with. I have learned a lot from him about antennas and microwaves. I also would like to thank him for his friendship and being a designated driver for life. I want to thank Tumay Kanar, for always being the first one to offer help when I needed it, and also for being a great gym brah; Samet Zihir, for feeding me amazing food and not letting me starve during all-nighters – I probably owe him a room full of snacks; Fatih Golcuk, for his friendship but also for being a big brother in times of need. After my move to the Bay Area, my life would have been a lot harder if he was not there. Furkan Kavasoglu, for encouraging me at times when I was upset and for our legendary FIFA rivalry; Ozgur Inac, for the most amazing conversations about science, politics and beer; Mehmet Uzunkol, for his sincere life advice and for all the amazing parties he threw; Kevin Ho, for his constructive criticisms of my work. I learned a lot from him about microwaves and PCB design.

I also would like to thank others who have been a big part of my experience at UCSD: Abdullah Alazemi, Alper Sinan Akyurek, Arda Suha, Aslihan Buner, Baris Aksanli, Baxtiyar Neyman, Berke Cetinoneri, Bhaskara Rao Rupakula, Brent Palmer, Cathleen Uzunoglu, Can Bal, Can Karakus, Chenhui Niu, Chih-Hsiang Ko, Dilara Onur, Doruk Beyter, Efe Can, Gulen Ozkula, Hasan Alrubaye, Hosein Zareie, Hsin-Chang Lin, Hyun-Ho Yang, Hyunchul Chung, Kerim Kibaroglu, Melis Okter, Meric Uzunoglu, Merve Oney, Michael Sharifi, Mike Luck, Mustafa Sayginer, Ozgur Yigit Balkan, Peter Weigel, Russell Brent, Selin Dag, Seymus Cacina, Steven Von Sofsrud Jackson, Tufan Gokirmak, Umut Kodak and Yang Yang.

Further, nothing I have accomplished in my life would be possible without the support of my family. I have seen them selflessly sacrifice a lot over the years and I will never be able

repay them for all the things they have done for me. However I also know that they did all they did for me without wanting anything in return. My mother, Mine Avser, has always been very patient and understanding towards me and always let me be myself. I know I can talk about anything with her. If there is one thing I am sure of, it is her selfless love for me. My father, Kubilay Avser, has always been my biggest mentor. We got into a lot of arguments when I was a teenager, but I think his perfectionism and persistence are what taught me to never give up and keep on working hard. Now that I am older, I understand him better and respect him so much. I want to thank my sister, Gozde Avser, for bringing joy into my life. I have always tried to be a better person around her, because I knew that she looked up to me. I must have done something right, because I am incredibly proud of the person she has become. And I want to thank my brother, Arda Camur. Since we were little kids playing on the street, he has always been there to talk when everything went wrong. Our routine of staying up late and talking till the sun came up turned into long distance skype calls at awkward hours of the day when I moved to the United States. But I know no matter what part of the world I live in, he will always be there for me.

Finally, I would like to thank Shannon Clark for her unending support and encouragement, and especially for putting up with my mood shifts when I was writing this thesis. Meeting her has changed me in ways I thought were not even possible and I am forever grateful for it.

The material in this dissertation is based on the following papers which are either published, or has been submitted for publication.

Chapter 2 is based on and mostly a reprint of the following papers:

- B. Avser, and G. M. Rebeiz, "Tunable Dual-Band Antennas for 0.7–1.1-GHz and 1.7–2.3-GHz Carrier Aggregation Systems," IEEE Trans. Antennas and Propag., vol. 63, no. 4, pp. 1498-1504, Apr. 2015.
- B. Avser, and G. M. Rebeiz, "Low-profile 700–970 MHz and 1600–2200 MHz dual-band tunable antenna for carrier aggregation systems," IEEE Antennas and Propagation Society International Symp., July 2014, pp. 999-1000.

Chapter 3 is based on and mostly a reprint of the following paper:

- B. Avser, J. Pierro and G. M. Rebeiz, "Random Feeding Networks for Reducing the Number of Phase Shifters in Limited-Scan Arrays," submitted for publication in IEEE Trans. Antennas and Propag., Oct. 2015.

Chapter 4 is based on and mostly a reprint of the following paper:

- B. Avser, R. Frazita and G. M. Rebeiz, "Interwoven Feeding Networks with Aperture Sinc-Distribution for Limited-Scan Phased Arrays and Reduced Num-

ber of Phase Shifters," submitted for publication in IEEE Trans. Antennas and Propag., Nov. 2015.

The dissertation author was the primary author of the work in these chapters, and coauthors (Prof. Gabriel M. Rebeiz, John Pierro, and Richard Frazita) have approved the use of the material for this dissertation.

VITA AND PUBLICATIONS

2007 - 2011	B. S. in Electical and Electronics Engineering (Fields and Waves), Bilkent University, Ankara, Turkey
2011 - 2013	M. S. in Electrical Engineering (Electronic Circuits and Systems), University of California, San Diego, La Jolla, California
2013 - 2015	Ph. D. in Electrical Engineering (Electronic Circuits and Systems), University of California, San Diego, La Jolla, California

B. Avser, R. Frazita, and G. M. Rebeiz, "Interwoven Feeding Networks with Aperture Sinc-Distribution for Limited-Scan Phased Arrays and Reduced Number of Phase Shifters," *IEEE Transactions on Antennas and Propagation*, submitted for publication, November 2015.

B. Avser, J. Pierro, and G. M. Rebeiz, "Random Feeding Networks for Reducing the Number of Phase Shifters in Limited-Scan Arrays," *IEEE Transactions on Antennas and Propagation*, submitted for publication, October 2015.

A, J. Alazemi, B. Avser, and G. M. Rebeiz, "Low-Profile Multi-band Tunable Antennas Using Series and Shunt Tuning Devices" *IEEE Transactions on Antennas and Propagation*, submitted for publication, November 2015.

B. Avser and G. M. Rebeiz, "Tunable Dual-Band Antennas for 0.7–1.1-GHz and 1.7–2.3-GHz Carrier Aggregation Systems," *IEEE Transactions on Antennas and Propagation*, vol. 63, no. 4, pp. 1498-1504, April 2015.

B. Avser and G. M. Rebeiz, "Low-profile 700–970 MHz and 1600–2200 MHz dual-band tunable antenna for carrier aggregation systems," *IEEE Antennas and Propagation Society International Symp.*, July 2014, pp. 999-1000.

B. Avser and V. B. Erturk, "A new method for the prognosis of scan blindness angle in finite phased arrays of printed dipoles," *IEEE European Conference on Antennas and Propagation*, April 2011, pp. 1014-1017.

ABSTRACT OF THE DISSERTATION

Frequency Tunable Antennas and Novel Phased Array Feeding Networks for Next Generation Communication Systems

by

Bilgehan Avser

Doctor of Philosophy in Electrical Engineering (Electronic Circuits and Systems)

University of California, San Diego, 2015

Professor Gabriel M. Rebeiz, Chair

The thesis presents three dual-band frequency tunable antennas for carrier aggregation systems and two new feeding networks for reducing the number of phase shifters in limited-scan arrays. First, single- and dual-feed, dual-frequency, low-profile antennas with independent frequency tuning using varactor diodes are presented. The dual-feed planar inverted F-antenna (PIFA) has two operating frequencies which are independently tuned at 0.7–1.1 GHz and at 1.7–2.3 GHz with better than 10 dB impedance match. The isolation between the high-band and the low-band ports is $>$ 13 dB; hence, one resonant frequency can be tuned without affecting the other. The single-feed contiguous-dual-band antenna has two resonant frequencies, which are independently tuned at 1.2–1.6 GHz at 1.6–2.3 GHz with better than 10 dB impedance match for most of the tuning range. And the single-feed dual-band antenna has two resonant frequencies, which are independently tuned at 0.7–1.0 GHz at 1.7–2.3 GHz with better than 10 dB impedance

match for most of the tuning range. The tuning is done using varactor diodes with a capacitance range from 0.8 to 3.8 pF, which is compatible with RF MEMS devices. The antenna volumes are $63 \times 100 \times 3.15\ mm^3$ on $\epsilon_r = 3.55$ substrates and the measured antenna efficiencies vary between 25% and 50% over the tuning range. The application areas are in carrier aggregation systems for fourth generation (4G) wireless systems.

Next, a new phased array feeding network that employs random sequences of non-uniform sub-arrays (and a single phase shifter for each sub-array) is presented. When these sequences are optimized, the resulting phased arrays can scan over a wide region with low side-lobe levels. Equations for analyzing the random arrays and an algorithm for optimizing the array sequences are presented. Multiple random-solutions with different number of phase shifters and different set of sub-array groups are analyzed and design guidelines are presented. The performance of the random array feeding scheme is compared to the conventional uniform sub-arraying for multiple cases. It is shown that with the random feeding networks, the number of phase shifters can be reduced up to 30% while preserving the system performance. This results in more affordable and more reliable systems. The proposed feeding network is demonstrated for a 30 element array of slot- fed patch antennas at 7.9 GHz. The fabricated array uses 12 phase shifters, has a half power beamwidth (HPBW) of 4^o and can scan up to $\pm 14^o$ with sidelobe levels less than -15 dB.

Another phase shifter reducing method, the interwoven feeding networks, is investigated. These passive feeding networks are composed of power dividers, couplers and resistive attenuators. In this configuration, each phase shifter feeds all of the antennas and creates a sinc-like current distribution over the array elements which results in a boxcar function-like element pattern. This element pattern is used to cancel the grating lobes. By changing the inter-element spacing and the coupling and attenuation coefficients of the feed network, it is possible to adjust the width of the scan region. Different network configurations along with theoretical limitations are investigated to determine the scanable region, side-lobe level and power loss. For the demonstration, two prototype linear arrays with 28 elements are fabricated. Both of the arrays operate at 7.9 GHz. The first array employs 14 phase shifters, has a half power beamwidth (HPBW) of 4^o and can scan up to $\pm 24^o$ with sidelobe levels less than -15 dB. The second array uses 7 phase shifters, has a half power beamwidth (HPBW) of 4^o and can scan up to $\pm 11^o$ with sidelobe levels less than -15 dB. Both of these arrays show state-of-the-art performance in terms of reducing the number of phase shifters while still keeping a low sidelobe level and reducing the effect of the grating lobes.

Chapter 1

Introduction

1.1 Frequency Tunable Dual-Band Antennas

The rapidly increasing amount of content on the Internet and the expanding user database create a demand for higher data-rate communication systems. New communication standards that allow higher data-rates require devices to simultaneously operate at several channels distributed over multiple frequency bands. Hence, new generation antennas need to operate over multiple wide bands with high radiation efficiency. At the same time, they need to be compact enough to fit inside the slim profile of modern mobile devices.

Multi-band antennas based on the planar inverted F-antenna (PIFA) have been extensively used in modern wireless platforms such as smart phones and pads [1–10]. These antennas are compact in size and can be designed with multiple resonances so as to provide either wide band operation or several distinct operating bands covering the 700 MHz to 2700 MHz range. However, the performance of these antennas are limited by a fundamental trade-off between antennas size, bandwidth and efficiency [11]. One way to overcome this limit is using low-profile frequency tunable antennas with high efficiencies and tuning the operating frequencies of the antennas to the desired communication channels. Such antennas can be built by loading the PIFAs with devices having a variable capacitance such as switched capacitor arrays, varactor diodes and RF MEMS variable capacitors. This results in tunable operation, thereby optimizes the antenna radiation efficiency for different bands [12–16]. In fact, tear-downs on several popular smart phones show that PIFAs with switched capacitors are readily being used on modern devices [17–19].

A new standard in the 3GPP (3rd Generation Partnership Project) Long-Term Evolu-

tion (LTE) consortium is carrier aggregation (CA) [20–22]. In the first implementation of the CA standard, two receive frequencies are used to improve the download data rate. One of the receive frequencies is always paired with the transmit frequency (as a standard W-CDMA pair), and the other frequency can be located anywhere. In this thesis, three low-profile dual-band antennas with single- and dual-feed configurations are presented. The antennas operate at 0.7-1.1 GHz, 1.2-1.6 GHz and 1.7-2.3 GHz bands and are compatible with CA systems.

1.2 Limited Scan Phased Arrays

Phased-array systems have been widely used since the 1970s for radar and communications systems, with their unique ability to scan the antenna beam electronically [23]. Since the early stages of this technology, phase shifters are regarded as the most expensive, sensitive and complex elements of these systems. The exponential increase of the computation power in the past decade has allowed the development of phased-array design processes using powerful full-wave numerical techniques and computational optimization methods [24, 25]. Also on the hardware side, the advancements in the MMIC and the RF MEMS technologies has allowed the production of more reliable and relatively inexpensive phase shifters. However, phase shifters still constitute the most complex and expensive parts of these systems. And the design of large-scale phased-array systems remains a challenging task due to the complex phase control networks, mutual coupling between array elements and the corporate feeding networks between phase shifters and the antennas.

Phased-array systems are mostly employed in the fields of defense and space for high-data rate communication and radar applications [26–28]. These applications require narrow beams with very low sidelobe levels that can scan precisely in a wide field of view. Hence, high performance is a more important design criteria than low-cost. However, in the recent years, phased array systems are starting to be widely used for commercial applications such as automotive radars [29–31] and advanced movement and robotic sensors. These applications can work withe a narrower field of view and can tolerate higher side lobe levels. However, due to the commercial nature of these applications, criteria such as low cost, integrability and low complexity are very important. In this thesis, two new feeding networks that can reduce the number of phase shifter in limited-scan arrays are presented.

1.3 Thesis Overview

The thesis presents three dual-band frequency tunable antennas for carrier aggregation systems and two new feeding networks for reducing the number of phase shifters in limited-scan arrays.

Chapter 2 presents single- and dual-feed, dual-frequency, low-profile antennas with independent frequency tuning using varactor diodes. The dual-feed planar inverted F-antenna (PIFA) has two operating frequencies which are independently tuned at 0.7–1.1 GHz and at 1.7–2.3 GHz. The isolation between the high-band and the low-band ports is ¿13 dB; hence, one resonant frequency can be tuned without affecting the other. The single-feed contiguous-dual-band antenna has two resonant frequencies, which are independently tuned at 1.2–1.6 GHz at 1.6–2.3 GHz. And the single-feed dual-band antenna has two resonant frequencies, which are independently tuned at 0.7–1.0 GHz at 1.7–2.3 GHz. The tuning is done using varactor diodes with a capacitance range from 0.8 pF to 3.8 pF, which is compatible with RF MEMS devices. The antenna volumes are $63 \times 100 \times 3.15mm^3$ on $\epsilon_r = 3.55$ substrates (Rogers RO4003) and the measured antenna efficiencies vary between 25% and 50% over the tuning range. The application areas are in carrier aggregation systems for fourth generation (4G) wireless systems.

Chapter 3 presents a new phased array feeding network that employs random sequences of non-uniform sub-arrays (and a single phase shifter for each sub-array). When these sequences are optimized, the resulting phased arrays can scan over a wide region with low sidelobe levels. Equations for analyzing the random arrays and an algorithm for optimizing the array sequences are presented. Multiple random-solutions with different number of phase shifters and different set of sub-array groups are analyzed and design guidelines are presented. The performance of the random array feeding scheme is compared to the conventional uniform sub-arraying for multiple cases. It is shown that with the random feeding networks, the number of phase shifters can be reduced up to 30% while preserving the system performance. This results in more affordable and more reliable systems. The proposed feeding network is demonstrated for a 30 element array of slot- fed patch antennas at 7.9 GHz. The fabricated array uses 12 phase shifters, has a half power beamwidth (HPBW) of 4^o and can scan up to $\pm 14^o$ with sidelobe levels less than -15 dB.

Chapter 4 presents another novel feeding network design (interwoven feeding network) that reduces the number of phase shifters in limited-scan arrays. In this passive feed network, each phase shifter feeds all of the antennas and creates a sinc-like current distribution over the array elements which results in a boxcar function-like element pattern. This element

pattern is used to cancel the grating lobes. By changing the inter-element spacing and the coupling and attenuation coefficients of the feed network, it is possible to adjust the width of the scan region. Different network configurations along with theoretical limitations are investigated to determine the scanable region, side-lobe level and power loss. For the demonstration, two prototype linear arrays with 28 elements are fabricated. Both of the arrays operate at 7.9 GHz. The first array employs 14 phase shifters, has a half power beamwidth (HPBW) of 4^o and can scan up to $\pm 24^o$ with sidelobe levels less than -15 dB. The second array uses 7 phase shifters, has a half power beamwidth (HPBW) of 4^o and can scan up to $\pm 11^o$ with sidelobe levels less than -15 dB. Both of these arrays show state-of-the-art performance in terms of reducing the number of phase shifters while still keeping a low sidelobe level and reducing the effect of the grating lobes.

The thesis concludes with a summary of the work and suggestions for future work.

Chapter 2

Tunable Dual-Band Antennas for 0.7–1.1-GHz and 1.7–2.3-GHz Carrier Aggregation Systems

2.1 Introduction

A new standard in the 3GPP (3rd Generation Partnership Project) Long-Term Evolution (LTE) consortium is carrier aggregation (CA) [20–22]. In the first implementation of the CA standard, two receive frequencies are used to improve the download data rate. One of the receive frequencies is always paired with the transmit frequency (as a standard W-CDMA pair), and the other frequency can be located anywhere. Fig. 2.1 presents several cases with different combinations of the receive frequencies. The selection of frequencies depends on the carriers and countries of use, and a first introduction of CA is the use of a single low-band (LB: 700-950 MHz) and a single mid-band (MB: 1700-2200 MHz) frequency pair, as shown in Fig. 2.1(b).

From an antenna point of view, the CA standard can be implemented in two ways: a) use of a wideband antenna, albeit at a lower efficiency, or b) use of a tuned antenna, but with tuning at two different frequencies. The latter case can also be implemented with a single feed or a dual-feed (one feed for LB and one feed for MB). The dual-feed antenna can also result in a high isolation between the low-band and high-band ports, and allow the use of tunable notch filters at the two antenna ports so as to reduce the effect of non-linearities between the LB and the MB ports. For example, for a 700 MHz Tx/Rx (band 17) and a 2100 MHz Rx combination (band 4), the third harmonic from the 700 MHz transmitter which is created in the antenna switch

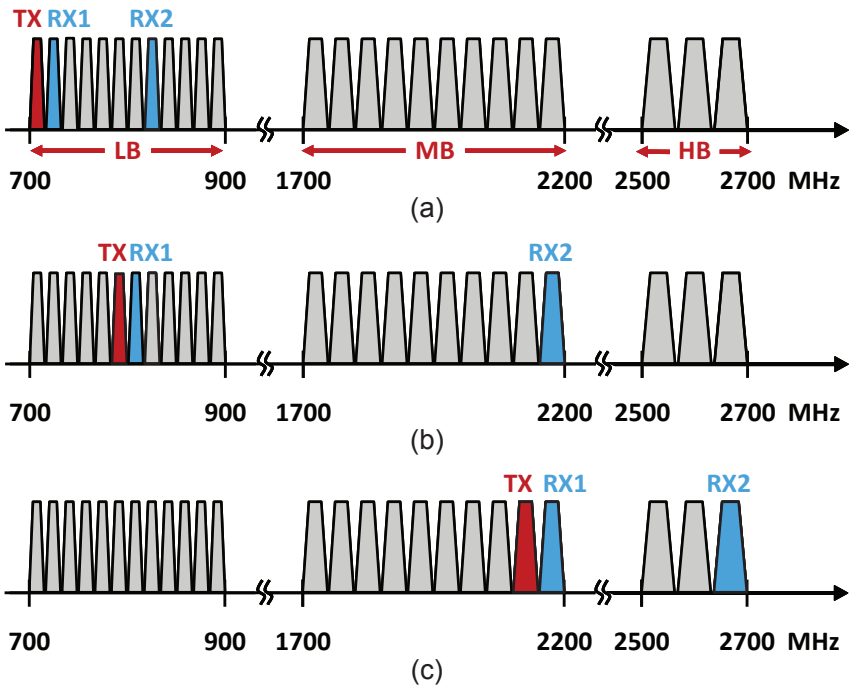

Figure 2.1: One transmit, two receive frequency carrier-aggregation system configurations using (a) two low-band frequencies (ex: Band 5 + Band 17), (b) one low-band and one mid-band frequency (ex: Band 5 + Band 1) and, (c) one mid-band and one high-band frequency (ex: Band 1 + Band 7).

module can directly interfere with the 2100 MHz Rx channel, causing a detrimental effect to the Rx sensitivity.

This chapter includes three different low-profile dual-band antennas with independent frequency tunability. Firstly, a dual-band dual-feed tunable PIFA covering the 0.7-1.1 GHz and 1.7-2.3 GHz bands for CA systems is presented. The antenna is designed so that the tuning of the LB arm does not affect the resonance of the other arm, and vice-versa, thereby providing high isolation between the two different arms. The frequency is tuned by changing the bias voltage on the varactor diodes. Then, using the same design principles, a dual-band single-feed antenna with high tuning isolation, is demonstrated at the contiguous band of 1.1-2.3 GHz (1.1-1.7 GHz and 1.7-2.3GHz). Lastly, a dual-band single-feed antenna operating at 0.7-1.1 GHz and 1.7-2.3 GHz bands with high tuning isolation is demonstrated. We believe that such antennas will become useful for the 3GPP LTE CA standard.

2.2 Planar Inverted F-Antenna with Series Tuning Capacitance

A PIFA can be modeled as a shorted microstrip line with an open-end (Fig. 2.2) [2]. One way to tune this antenna is using a series capacitance, and the fundamental resonance occurs when the impedance seen from the short is zero ($Z_y = 0$) where

$$Z_y = Z_2 \frac{Z_x + jZ_2 \tan(\beta L_2)}{Z_2 + jZ_x \tan(\beta L_2)} \tag{2.1}$$

$$Z_x = \frac{1}{j\omega C} + \frac{Z_1}{j\tan(\beta L_1)}. \tag{2.2}$$

Z_x can be rewritten as

$$Z_x = \frac{Z_1}{j\frac{Z_1 \omega C \tan(\beta L_1)}{\tan(\beta L_1) + Z_0 \omega C}} \tag{2.3}$$

and is equivalent to an open-terminated transmission line with characteristic impedance Z_0, propagation constant β and length L_{new} where

$$L_{new} = \frac{1}{\beta} \tan^{-1} \left(\frac{Z_1 \omega C \tan(\beta L_1)}{\tan(\beta L_1) + Z_1 \omega C} \right). \tag{2.4}$$

The PIFA resonance with a series tuning capacitance will occur when

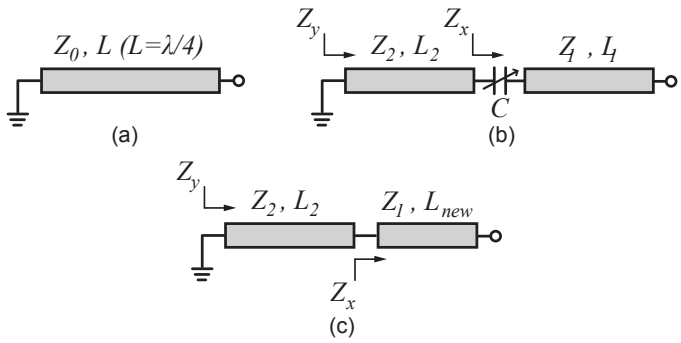

Figure 2.2: Transmission line models of (a) microstrip PIFA, (b) tunable microstrip PIFA with series capacitance and, (c) equivalent model of PIFA with series capacitance.

$$\beta(L_{eff}) = \beta(L_2 + L_{new}) = \pi/2. \tag{2.5}$$

Therefore by changing the tuning capacitance C, it is possible to control the effective antenna length and tune its resonance frequency. The position of the tuning capacitance, and the lengths L_1 and L_2 play an important role in the antenna performance. The goals to consider when selecting these parameters are the tunable frequency range and center frequency.

To analyze the effect of the capacitance position on the tunable range and center frequency, an antenna with constant length $L_{total} = L_1 + L_2 = 0.43\lambda_0$ (at 1 GHz) and $Z_1 = Z_2 = Z_0$ is considered. For capacitance values C_{min} and C_{max}, the resonance frequencies f_{max} and f_{min} are defined. The center frequency f_{center} and tunable range T are

$$f_{center} = \sqrt{f_{max} f_{min}} \tag{2.6}$$

and

$$T = \frac{f_{max} - f_{min}}{f_{center}}. \tag{2.7}$$

Fig. 2.3 presents the tunable range and center frequency with respect to the capacitance position for $C_{min} = 1$ pF and $C_{max} = 4$ pF, and for different Z_0 values. The $Z_1 = Z_2$ assumption is used to simplify the analysis. If they are assumed to be different, the conclusion will still be same. As the tuning capacitance is moved closer to the short (i.e., L_1 is increased and L_2 decreased), the variation in L_{new} is higher for the same ΔC, and moving the capacitance closer to the short increases the antenna tunable range. However, this also increases the antenna resonance

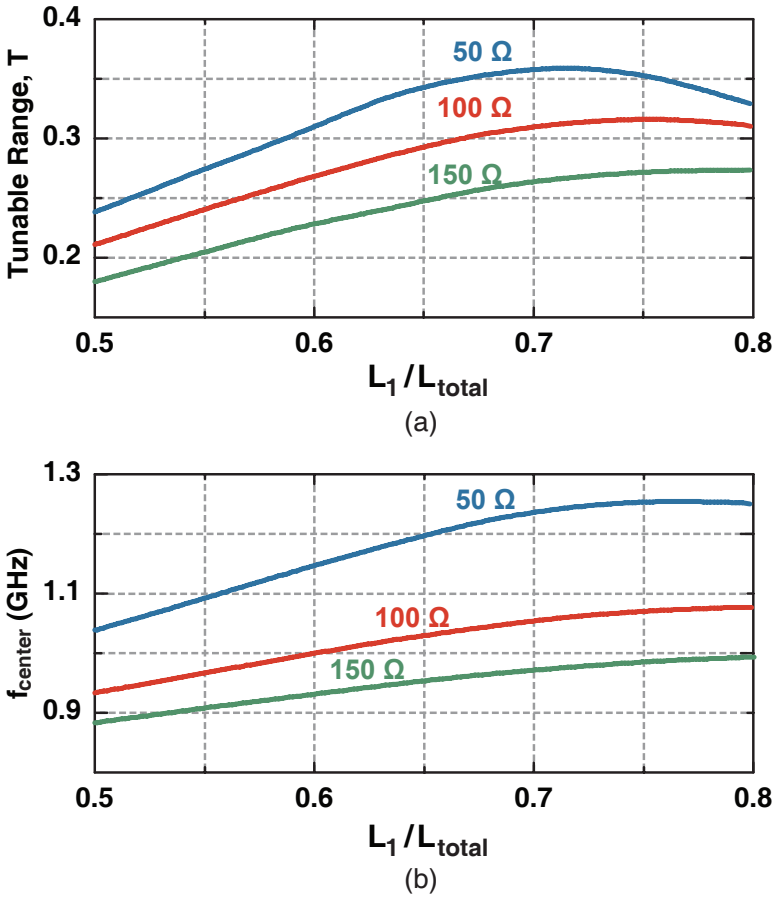

Figure 2.3: (a) Tunable range and (b) center frequency of PIFA with series capacitance for different characteristic impedances.

frequency because the decrease in L_2 is faster than the increase in L_{new}. This is shown in Fig. 2.3 for $50\Omega < Z_0 < 150\Omega$ and $0.5 < L_1/L_{total} < 0.8$. A $Z_0 = 100\Omega$ and $L_1/L_{total} = 0.65$ is selected for a 30% tunable range as the basis of the antenna designs.

2.3 Dual-Feed Dual-Band Antenna

2.3.1 Design

The dual-feed dual-band antenna is shown in Fig. 2.4. The antenna resonance frequency is controlled using two varactor diodes (Skyworks SMV1232-040LF, C_{tot}= 0.8-3.8 pF, V_{bias} = 0-20 V). The antenna is printed on a $63 \times 100 \times 3.15$ mm^3 substrate stack which is formed by two 1.524 mm thick Rogers RO4003C substrates ($\epsilon_r = 3.55, tan\delta = 0.0027$ at 2.5 GHz) joined by a 0.101 mm Rogers RO4450B bond ply ($\epsilon_r = 3.54, tan\delta = 0.004$ at 10 GHz). In several other implementations, the antenna is made of sheet copper and suspended in air or printed on a low-ϵ_r plastic carrier [1, 3, 4, 6–8]. The choice of the substrate here is only for research/demonstration purposes since it is low cost and provides mechanical robustness for soldering.

The PIFA has two feeds that are used for low-band (feed 1) and high-band (feed 2) operation. Note that in this paper, all frequencies above 1.7 GHz are referred to as high-band (that is the mid-band and high-band are lumped together into one band). Shorting vias of the LB and HB PIFAs are combined together and placed between the feeds. The inductance of the six shorting vias is simulated using ANSYS HFSS [32] to be 0.17 nH, and results in a high isolation between the LB and HB PIFA arms. This makes it possible to independently tune the two resonance frequencies.

Fig. 2.4 (c) presents the transmission-line model, and is based on the tunable PIFA model described Chapter 2.2. Two tunable PIFAs are merged together at their short circuit sections and the inductive effects of the shorting vias are captured as L_s in the transmission-line model. The LB and HB resonances are controlled by varactor diodes C_1 and C_2, respectively. To reduce the antenna size, short sections of open-ended transmission lines are added to the LB PIFA. These sections act as fixed capacitances and their effects are captured as C_{p1} and C_{p2} in the transmission-line model. Adding shunt capacitances on each side of a TLIN also has a similar effect to meandering, since it makes it appear electrically longer. In this case the L_{11} section of the LB PIFA, with shunt capacitances C_{p1} and C_{p2} on each side appears to be 40% longer than L_{11}. This method is favored over meandering since it results in a higher simulated

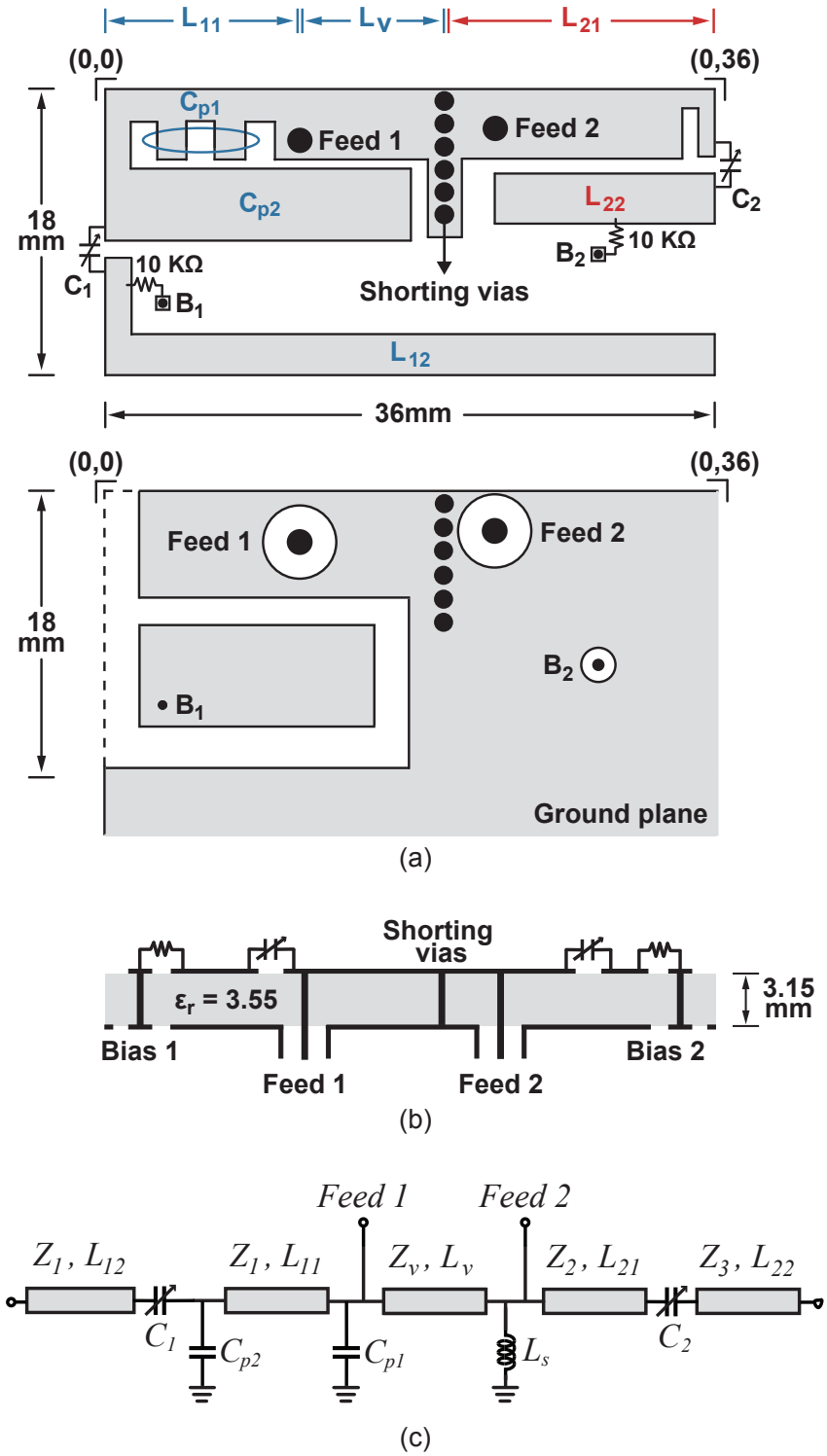

Figure 2.4: Dual-feed dual-band antenna geometry (a) top metal plate and groung plate, (b) cross section. All dimensions are in mm. (c) Transmission-line model.

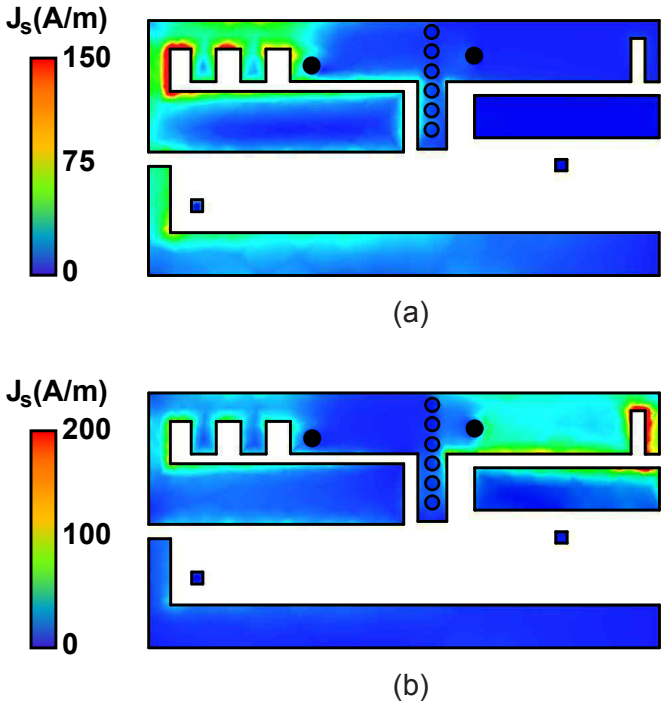

Figure 2.5: Dual-feed dual-band antenna current distribution at (a) low-band operation (0.8 GHz) and at (b) high-band operation (1.8 GHz).

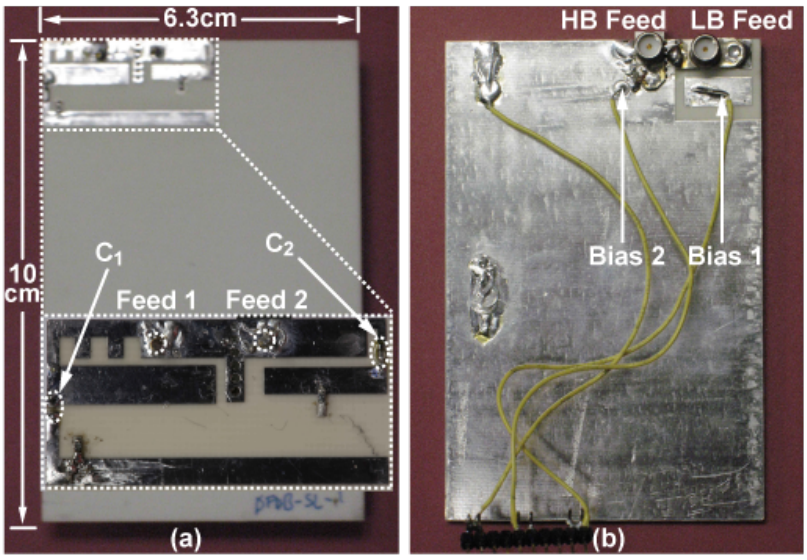

Figure 2.6: Fabricated dual-feed dual-band antenna for carrier aggregation. (a) Top plane and (b) ground plane.

efficiency. Slots are introduced on the ground plane under the LB PIFA to enhance the fringing fields and increase the antenna efficiency [33]. The varactor diodes are biased at points B_1 and B_2 using 10 kΩ resistors. The resistors are placed on the top metal plate and soldered between the PIFA arms (L_{12}, L_{22}) and the biasing pads so as to isolate the antenna from the biasing via inductance and its parasitic capacitance to the ground. The transmission-line model is utilized as a tool to understand the tuning mechanisms of the antennas and to form a basis for the initial design. The final design is optimized using electromagnetic simulation software.

The tuning characteristics were simulated with surface impedance boundary conditions at the tuning device ports using ANSYS HFSS. The low-band operation, using feed 1, covers the 0.7-1.1 GHz band whereas the high-band operation, using feed 2, covers the 1.7-2.3 GHz band. Fig. 2.5 (a) and (b) show the current distributions over the antenna at low-band and high-band operation, respectively. The current is concentrated on the low-band arm at the low-band operation and on the high-band arm at the high-band operation which results in high tuning isolation. During the high-band operation, a small amount current is observed on the low-band portion. This is because the second resonance of the LB PIFA coincides with the first resonance of the HB PIFA. The fabricated antenna is shown in Fig. 2.6.

2.3.2 Results and Discussion

The antenna two-port S-parameters are measured in an anechoic chamber for all combinations of the low-band (port 1) and high-band (port 2) bias states with an Agilent E5071B vector network analyzer.

Fig. 2.7 presents the S-parameter measurements when the bias on the low-band diode is changed (0-20 V) and the bias on the high-band diode is held constant at 0 V, or 5 V, or 10 V. The center frequency of the low-band antenna varies from 0.75-1.05 GHz as the low-band bias varies from 0-20 V. The center frequency of the high-band is constant at 1.7 GHz (0 V), 2.05 GHz (5 V) and 2.17 GHz (10V) independent of the bias on the LB diode. The -7 dB S_{11} bandwidth is 25 MHz to 70 MHz for the LB antenna as it tunes from 750 to 1050 MHz, respectively.

Fig. 2.8 presents the S-parameter measurements when the bias on the high-band diode is changed (0-20 V) and the bias on the low-band diode is held constant at 0 V, or 5 V, or 10 V. The center frequency of the high-band varies from 1.7-2.2 GHz as the high-band bias varies from 0-20 V. The center frequency of the low-band is constant at 0.75 GHz (0 V), 0.95 GHz (5 V) and 1.0 GHz (10V) independent of the bias on the LB diode. The -7 dB S_{22} bandwidth is 60 MHz to 90 MHz for the HB antenna as it tunes from 1700 to 2200 MHz, respectively.

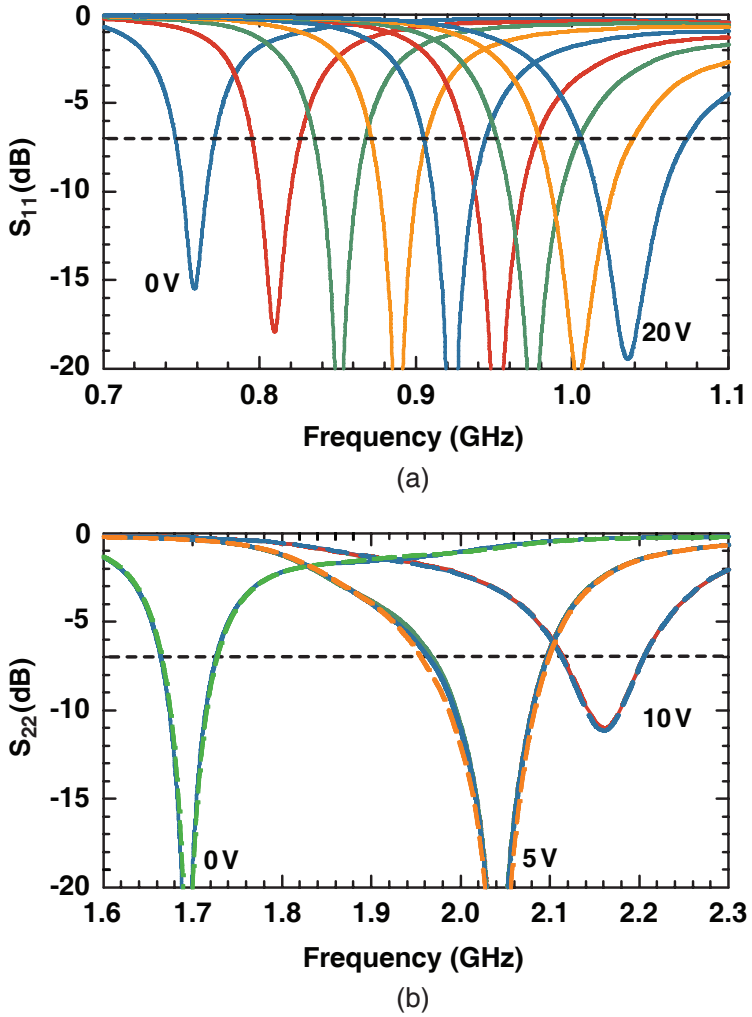

Figure 2.7: Dual-feed dual band antenna, LB tuning, measured (a) S_{11} and (b) S_{22}.

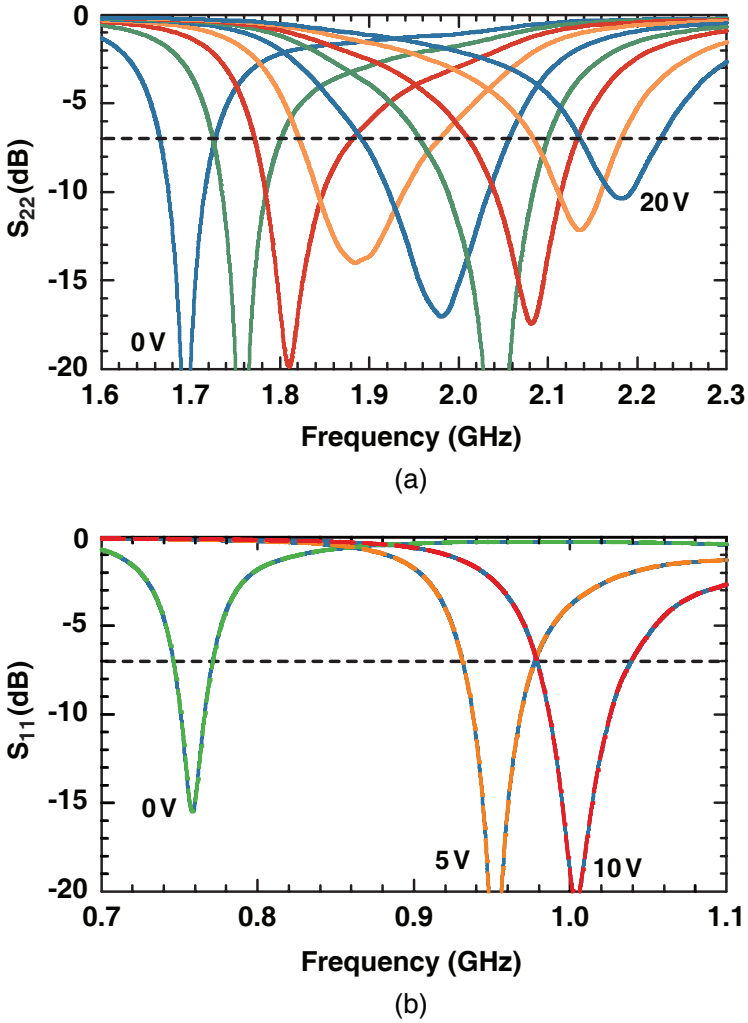

Figure 2.8: Dual-feed dual band antenna, HB tuning, measured (a) S_{22} and (b) S_{11}.

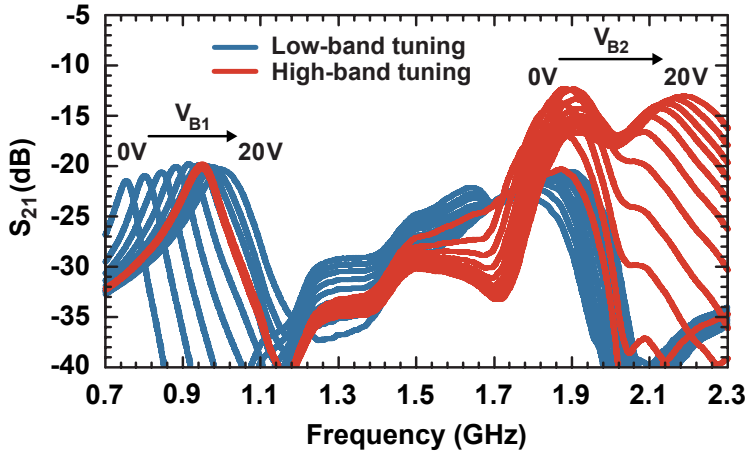

Figure 2.9: Dual-feed dual-band antenna isolation: worst case for low-band tuning (V_{B1} : $0-20$ V, V_{B2} : 5 V) and worst case for high-band tuning (V_{B1} : 5 V, V_{B2} : $0-20$ V).

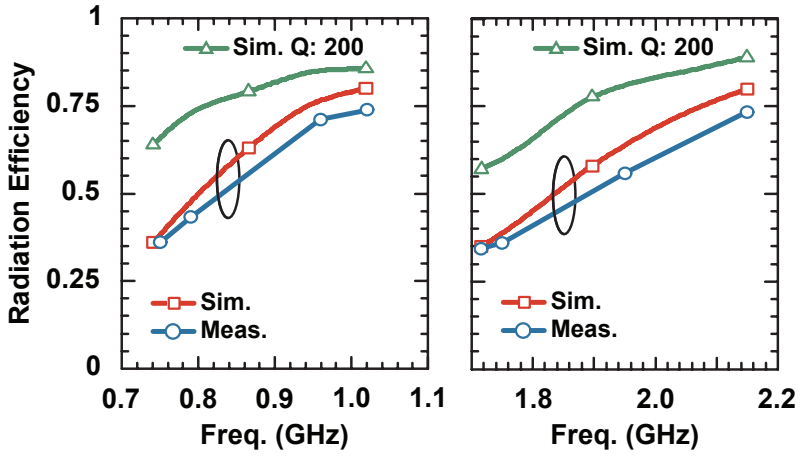

Figure 2.10: Dual-feed dual-band antenna simulated and measured efficiency.

Fig. 2.9 represents the measured isolation (S_{21}) between the two ports at the worst cases of tuning. The isolation is worst when the HB frequency is tuned at around two times the LB frequency, since the first HB PIFA mode couples to the second LB PIFA mode. The isolation between the ports is $S_{21} < -20$ dB at 700-950 MHz and $S_{21} < -13$ dB at 1.7-2.3 GHz for all tuning states. This allows the antenna to be used as a tunable duplexing circuit between LB and HB ports [1].

The radiation patterns of the antenna were measured using a Satimo SG32 spherical near-field chamber (gain error $\leq \pm 0.75dB$) [34]. The measured and simulated radiation effi-

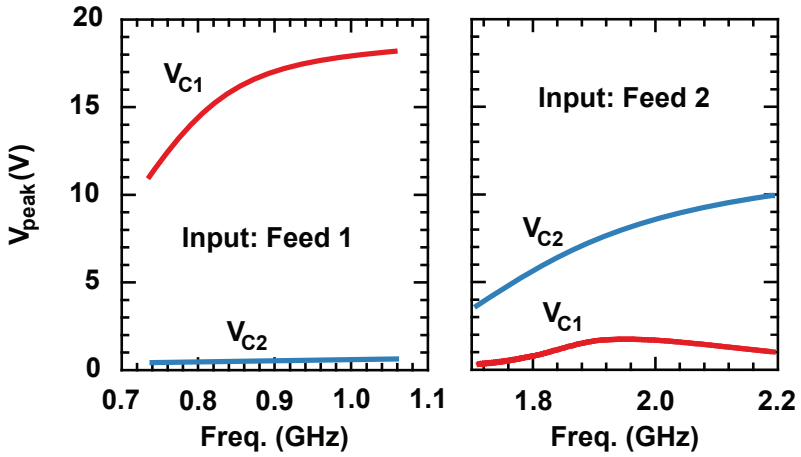

Figure 2.11: Dual-feed dual-band antenna peak voltages on tuning devices.

ciency is plotted in Fig. 2.10. The efficiency increases as the antenna is tuned to higher frequencies. This is because the antenna radiation Q decreases with frequency and the varactor diode Q increases as the capacitance decreases (i.e., with frequency). The antenna Q is calculated as $1/BW$ where BW is the 3-dB bandwidth of the antenna VSWR. The LB antenna Q is estimated to be 39-20 at 0.75-1.1 GHz and the HB antenna Q is estimated to be 26-16. at 1.7-2.2 GHz. A series RLC boundary condition ($C = 0.8 - 3.8$ pF, $R_s = 2\Omega$, $L = 0.45$ nH) is used to model the varactor diodes in the HFSS simulation. The varactor diode Q is 28-85 at 0.75-1.1 GHz (LB) and 12-45 at 1.7-2.2 GHz (HB). The simulated efficiency fits well with the measured efficiency. Radiation patterns are mostly isotropic for all of the tuning cases and as expected from PIFAs (Fig. 2.12).

For an input power of 20 dBm the maximum peak voltages across the LB and HB tuning devices are simulated as 18 V and 10 V (Fig. 2.11). Such voltage levels will shift the bias state of the varactors and thus the antenna center frequency [35]. This problem can be solved using RF MEMS switched-capacitors [36, 37]. The use of RF MEMS devices will also increase the efficiency. The simulated efficiencies with Q=200 at 0.7-1.0 GHz and 1.7-2.2 GHz devices which corresponds to RF MEMS switched capacitors are presented in Fig. 2.10.

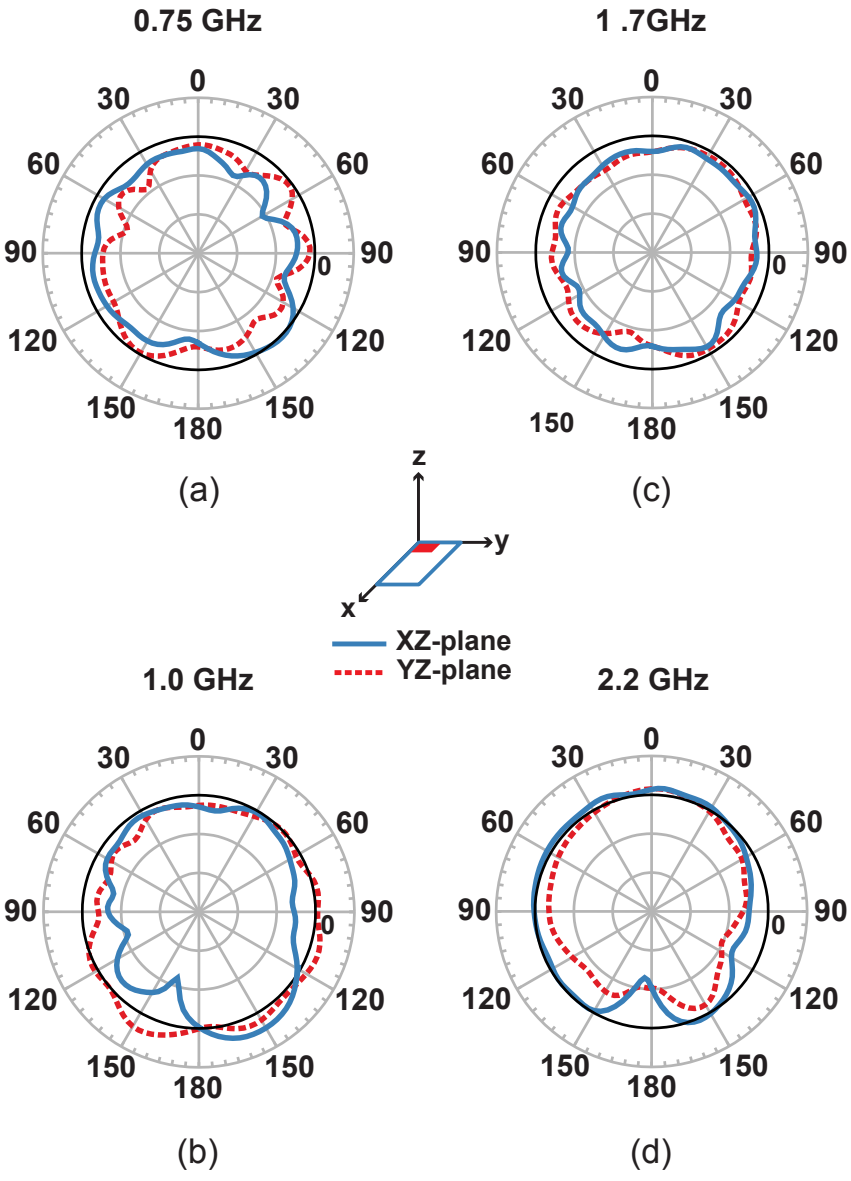

Figure 2.12: Dual-feed dual-band antenna normalized radiation patterns at (a) 0.75 GHz, (b) 1.0 GHz low-band operation and (c) 1.7 GHz, (d) 2.2 GHz high-band operation. Concentric circles correspond to 10 dB increments.

2.4 Single-Feed Contiguous-Band Antenna

2.4.1 Design

Fig. 2.13 presents the single-feed dual contiguous-band antenna. The antenna is printed on the same $63 \times 100 \times 3.15$ mm^3 substrate with $\epsilon_r = 3.55$ similar to the dual-feed dual-band antenna and same varactor diodes (Skyworks SMV1232-040LF) are used tune the antenna. 10 kΩ resistors are used to bias the varactor diodes at points B_1 and B_2. The same substrate and biasing pad configuration as the dual-feed dual-band antenna are used.

Similarly to the dual-feed dual-band antenna, the single feed antenna has two branches: one resonating at the low-band and one resonating at the high-band. Fig. 2.14 (a) and (b) show the current distributions at low-band and high-band operations, respectively. During the high-band operation, a small amount of current leaks on the low-band branch. This is because the second resonance of the low-band coincides with the first resonance of the high band. This causes the tuning isolation between the two antenna arms to decrease and causes a small variation (± 5 MHz) in the-high-band frequency as the low-band resonance frequency is tuned. This shift in the high-band frequency can be compensated by changing the bias voltage on the high-band varactor and effectively having a tuning voltage table for every combination of the low-band and high-band frequencies.

The transmission-line model for the antenna is presented in Fig. 2.13 (b). The varactor diode capacitances C_1 and C_2 are used to tune the two different antenna resonant frequencies. The lower resonance frequency can be tuned from 1.2 to 1.6 GHz and the higher resonance frequency can be tuned from 1.6 GHz to 2.3 GHz. These frequencies do not coincide with the traditional LB, MB and HB regions for CA standards (see Fig. 2.1), and were chosen to demonstrate a dual-tuned antenna with near-contiguous tuning, covering a 1.2-2.3 GHz range. The fabricated antenna is shown in Fig. 2.15.

2.4.2 Results and Discussion

The antenna impedance is measured in an anechoic chamber at all combinations of the low-band and high-band bias states with an Agilent E5071B network analyzer. The S-parameter measurements for the case when the bias on the low-band diode is changed (0-20 V) and the bias on the high-band diode is held constant at 20 V are presented in Fig. 2.16. The center frequency of the low-band PIFA arm varies from 1.2 to 1.6 GHz as the low-band bias voltage is changed. The -7 dB S_{11} bandwidth is 20-53 MHz as the antenna is tuned from 1200 to 1600

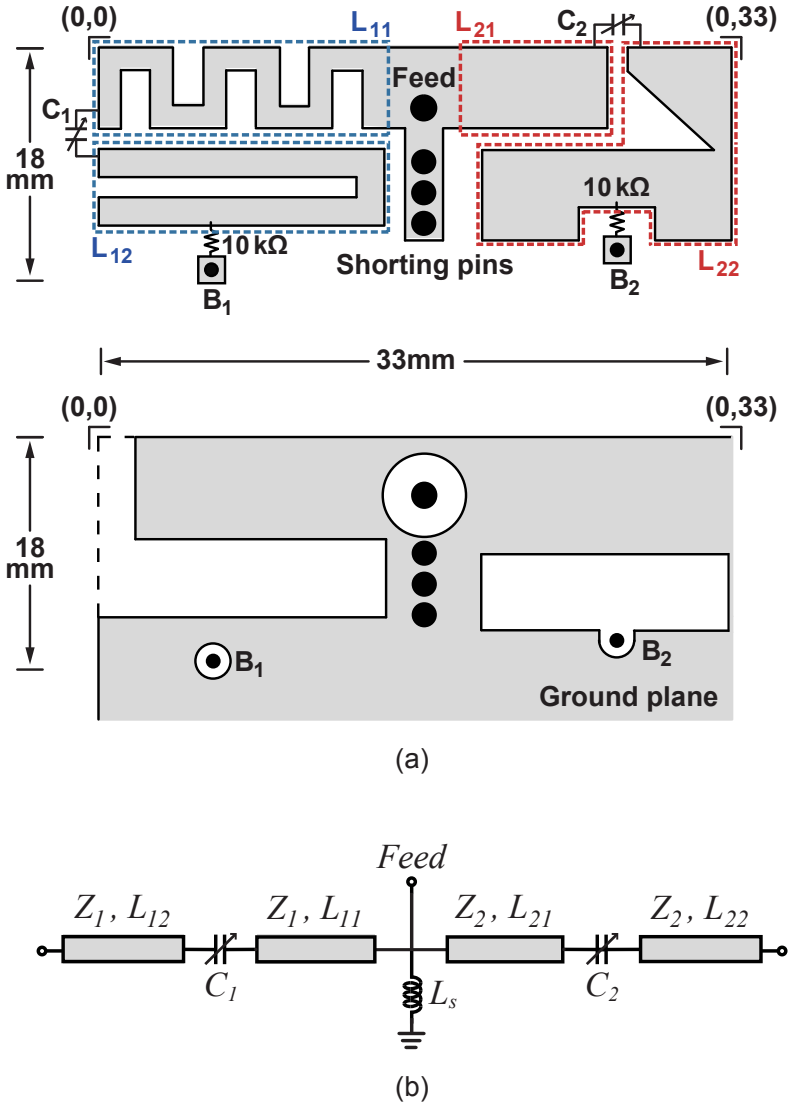

Figure 2.13: Single-feed contiguous-band antenna geometry: (a) top view and bottom view. All dimensions are in mm. (b) Transmission line model.

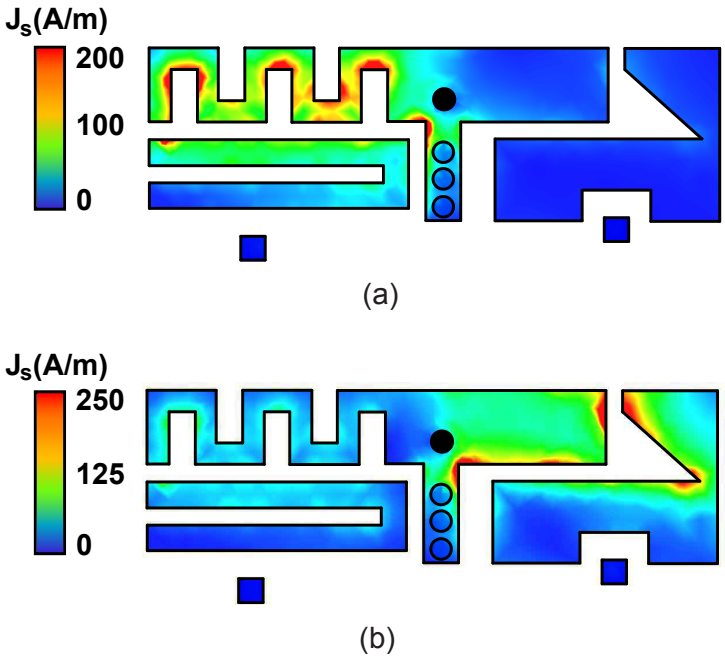

Figure 2.14: Single-feed contiguous-band antenna current distribution at (a) low-band operation (1.4 GHz) and at (b) high-band operation (1.9 GHz).

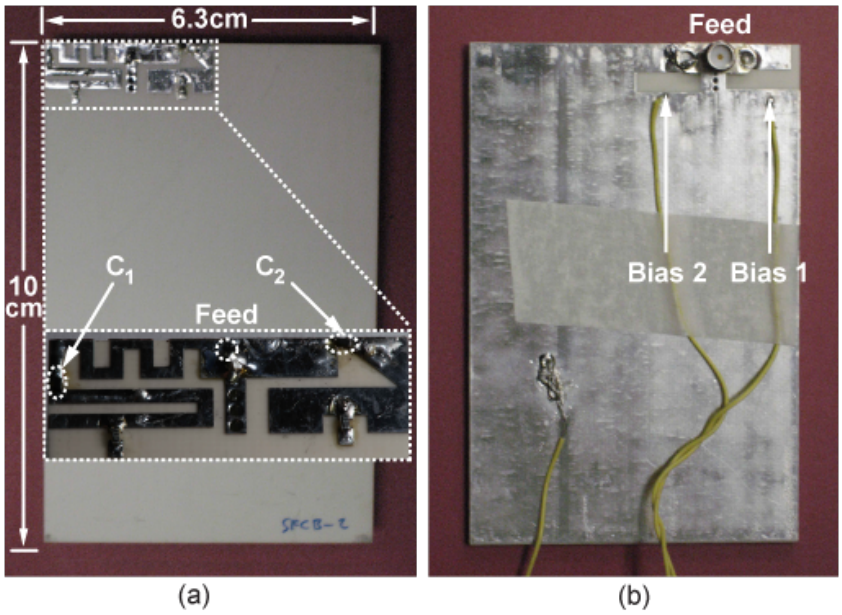

Figure 2.15: Fabricated single-feed contiguous band-antenna.

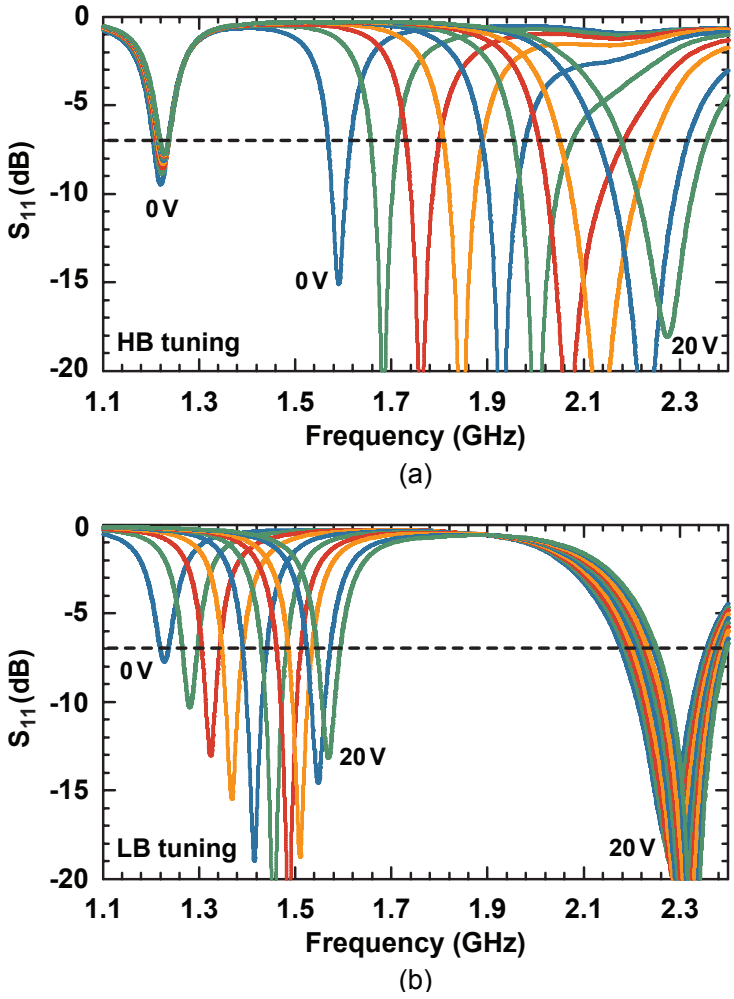

Figure 2.16: Single feed contiguous-band antenna measured S_{11} for (a) high band and (b) low band tuning.

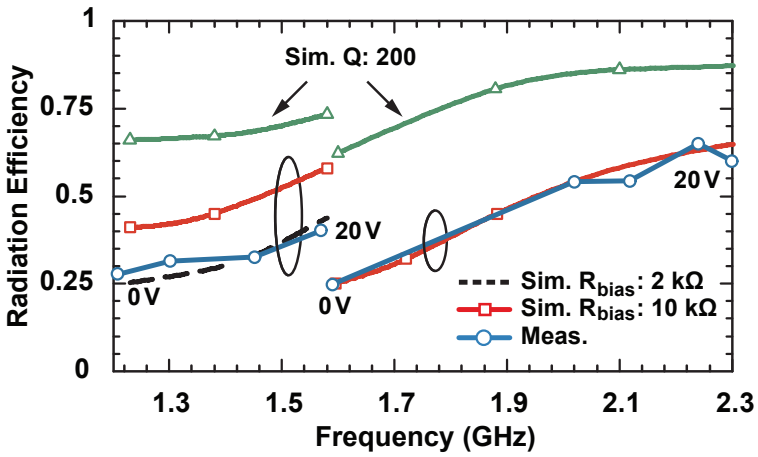

Figure 2.17: Single-feed contiguous-band antenna simulated and measured efficiency.

MHz, respectively. The S-parameter measurements for the case when the bias on the low-band diode is held constant at 0 V and the bias on the high-band is changed (0-20 V) are presented in Fig. 2.16. The center frequency of the high-band tunes from 1.6 to 2.3 GHz as the high-band bias voltage is changed, and the low-band resonance remains constant at 1.2 GHz. The -7 dB S_{11} bandwidth is 22-160 MHz for as the antenna is tuned from 1600 to 2200 MHz, respectively.

The radiation patterns of the antenna were measured using a Satimo SG32 spherical near-field chamber (gain error $\leq \pm 0.75dB$). Fig. 2.17 presents the measured and simulated radiation efficiency. Similarly to the double feed dual-band antenna, the efficiency increases as the antenna is tuned to higher frequencies inside each respective band. This is because the varactor diode Q increases as the capacitance decreases. The diode Q is 18-62 at 1.2-1.6 GHz (low-band) and 13-43 at 1.6-2.3 GHz (high-band). The measured efficiency agrees well with simulated efficiency on the high band. However it is lower than the simulated efficiency at the low band. We suspect that the 10 kΩ biasing resistor on the LB arm is acting as a $\sim$ 2 kΩ resistor due to its parasitic capacitance, and reducing the antenna Q. In fact, if a 2 kΩ resistor is used in simulations, the results agree well with the measurements (Fig. 2.17). For an input power of 20 dBm the maximum peak voltages across the LB and HB tuning devices are both simulated as 11 V (Fig. 2.18). As discussed in Chapter 2.4.2 these voltage levels might shift the bias state of the varactor diode also the antenna efficiencies are limited by the Q of the varactor diodes. Hence by using RF MEMS devices with Q=200, the bias shifting problem can be avoided also the efficiency can be increased to $>$ 60% for all of the tuning cases (Fig. 2.17).

Fig. 2.19 presents the measured radiation patterns. Radiation patterns are similar for

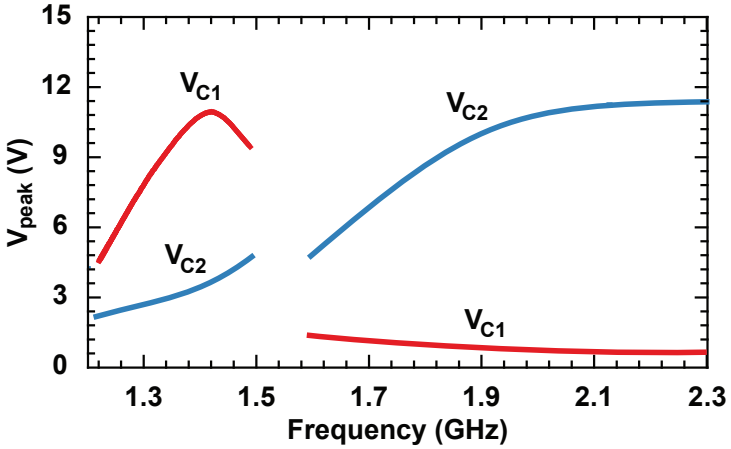

Figure 2.18: Single-feed contiguous-band antenna peak voltages on tuning devices.

all of the tuning cases and they are nearly isotropic as expected from a low profile antenna.

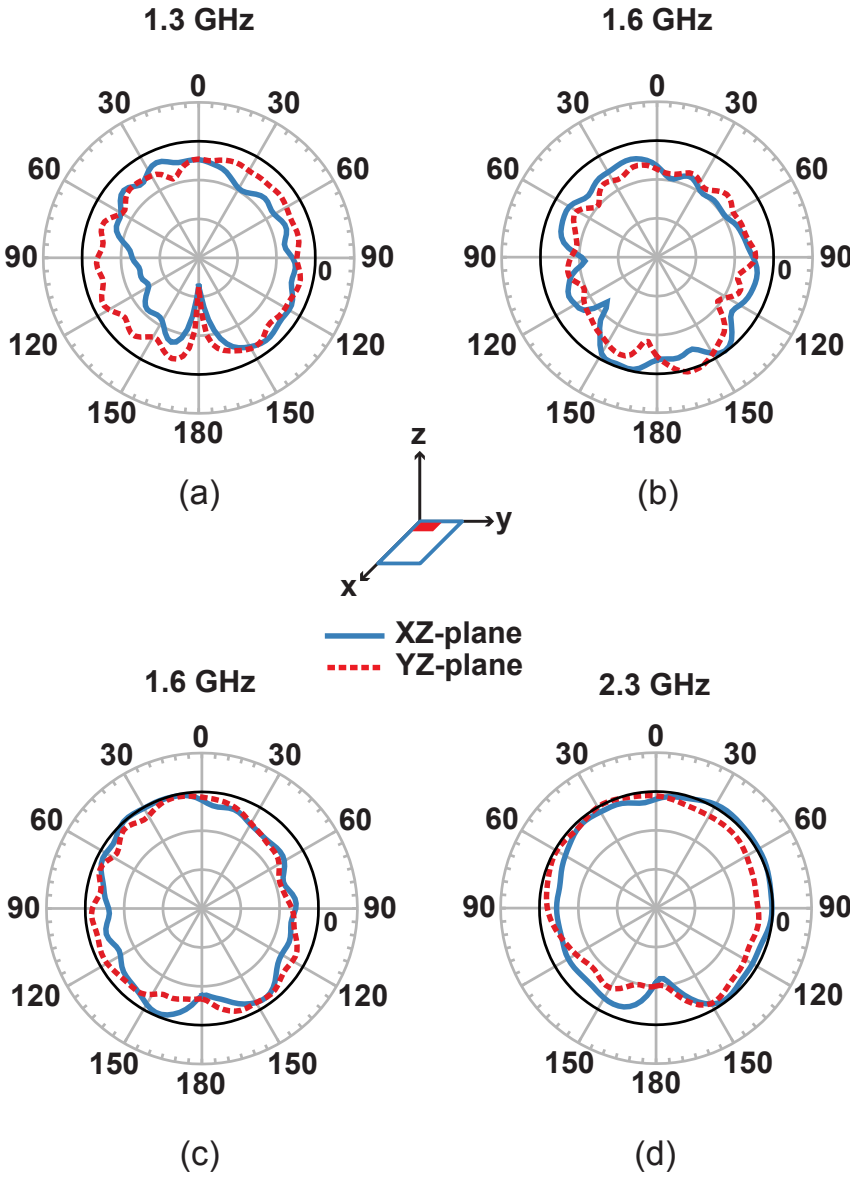

Figure 2.19: Single-feed contiguous-band antenna normalized radiation patterns at (a) low-band and (b) high-band. Concentric circles correspond to 10 dB increments.

2.5 Single-Feed Dual-Band Antenna

2.5.1 Design

The single-feed dual-band antenna is shown in Fig. 2.20. Similarly to the antennas presented in Chapters 2.3 and 2.4, the antenna resonance frequency is controlled using two varactor diodes (Skyworks SMV1232-040LF, C_{tot}= 0.8-3.8 pF, V_{bias} = 0-20 V) and the antenna is printed on a $63 \times 100 \times 3.15$ mm^3 substrate stack which is formed by two 1.524 mm thick Rogers RO4003C substrates ($\epsilon_r = 3.55, tan\delta = 0.0027$ at 2.5 GHz) joined by a 0.101 mm Rogers RO4450B bond ply ($\epsilon_r = 3.54, tan\delta = 0.004$ at 10 GHz). The PIFA has a single feed that is used for both low-band (0.7-1 GHz) and high-band (1.7-2.3 GHz) operation. Fig. 2.20 (b) presents the transmission-line model. The varactor diodes are biased at points B_1 and B_2 using 10 kΩ resistors. Similarly to the previous antennas, single-feed dual-band antenna also composes of two arms: one resonating at the high-band, one resonating at the low-band. The shorting vias in between is used to isolate the two radiating arms. The fixed capacitor, C_f, between the low band region and the ground (through the shorting pins) is used to further decrease the coupling between the high-band and the low-band regions, hence to achieve independent tuning of the two bands. The final design is optimized using electromagnetic simulation software. The fabricated antennas is presented in Fig. 2.21

2.5.2 Results and Discussion

Fig. 2.22(a) and Fig. 2.22(b) present the measured S_{11} and the simulated tuning range during the low-band and high band tuning, respectively. The antenna can continuously be tuned to any frequency inside the desired frequency range. Fig. 2.22(c) and Fig. 2.22(d) present the measured S_{11} of the fixed band while the other band is being tuned. High-band tuning does not effect the low-band match significantly. On the other hand, the low-band tuning slightly disturbs the high-band impedance match (the bandwith is still wide enough for proper operation). This is beacuse the second resonance of the low-band arm coincides with the first resonance of the high-band arm and disturbs the impedance match at the feed.

Fig. 2.23 present the measured antenna radiation pattern at the low-band and high-band frequencies. The patterns are near isotropical and have both polarizations as expected from a low-profile antenna. The measured total efficiency is %25-%61 for the high-band and %7-%20 for the-low band. Similarly to the previous antennas, the efficiency can be increased by using RF MEMS devices instead of varactor diodes.

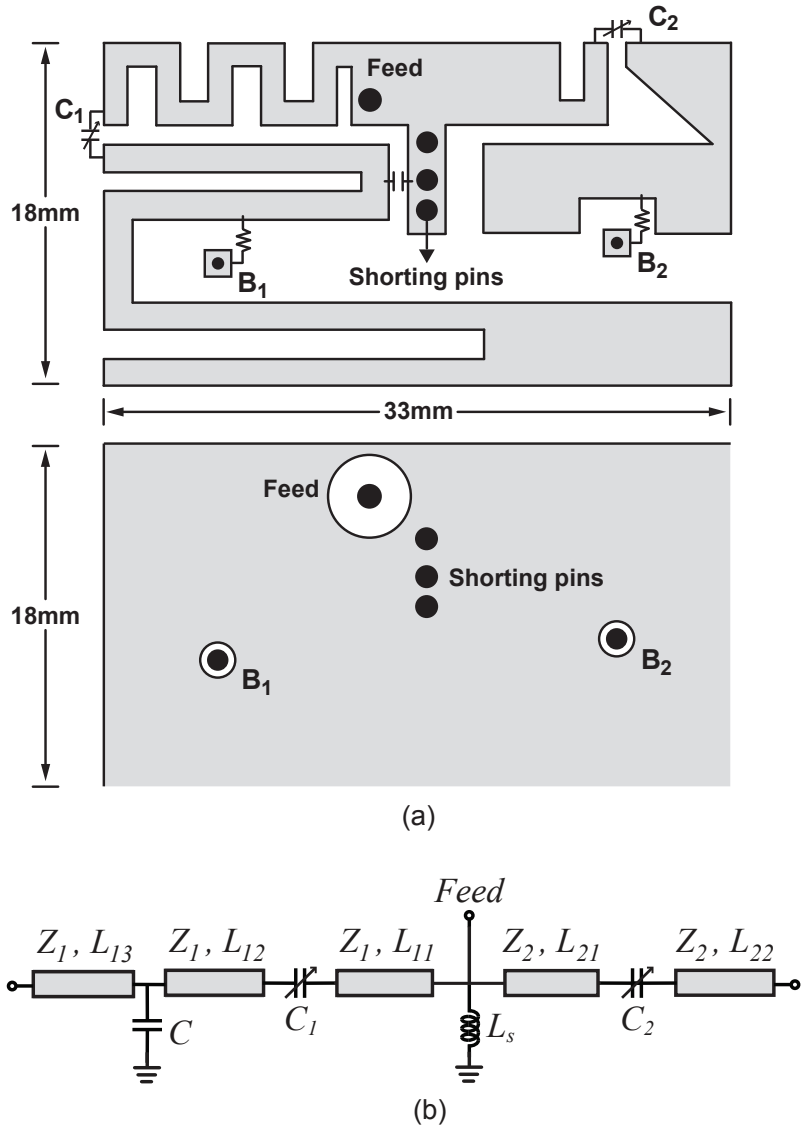

Figure 2.20: Single feed, dual-band antenna geometry: (a) top layer and ground plane, (b) equivalent transmission line model.

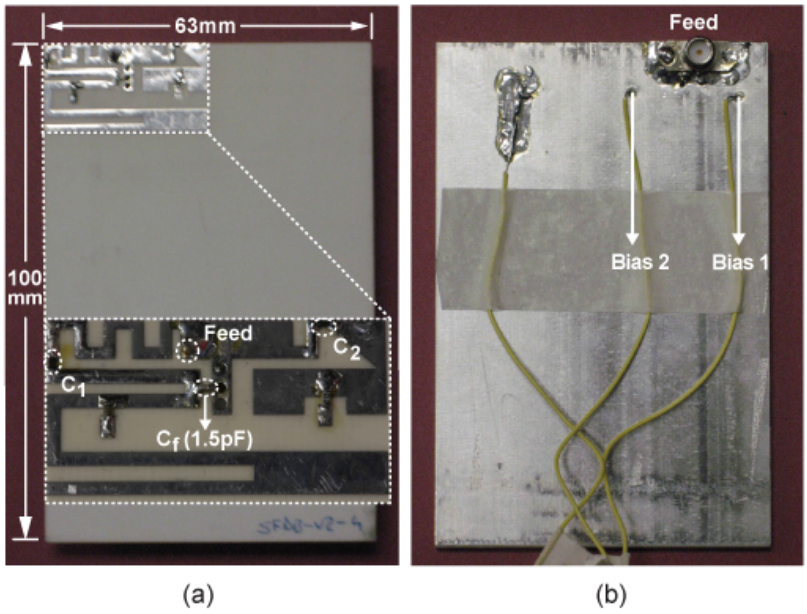

Figure 2.21: Fabricated single feed, dual-band antenna: (a) top and (b) ground layer.

2.6 Conclusion

A dual-feed dual-band PIFA covering the 0.7-1.1 GHz and 1.7-2.3 GHz bands has been demonstrated using varactor diodes. There exists a high isolation between the bands; hence the two resonance frequencies can be tuned independently without affecting each other. Using the same design principles, a single-feed dual-band PIFA covering the same frequency bands has been designed and demonstrated using varactor diodes. Similar to the dual-feed antenna, there exists a high isolation between the PIFA arms; hence allowing the two resonance frequencies to be tuned independently. Additionally, a single-feed antenna with two independently tunable resonant frequencies is demonstrated at 1.1-2.3 GHz using varactor diodes. The efficiencies of the antennas can be increased significantly by using RF MEMS varactors. In practice, and when these antennas are used in cell phones and with hand and body loading effects, the antennas will become more wideband and less efficient [38], and a lot of additional effort is needed to build a true working dual-band antenna on an actual platform. The goal of this work is to show that dual-tuned PIFAs are a promising candidate for increasing the performance of communications systems using the 3GPP LTE CA standard.

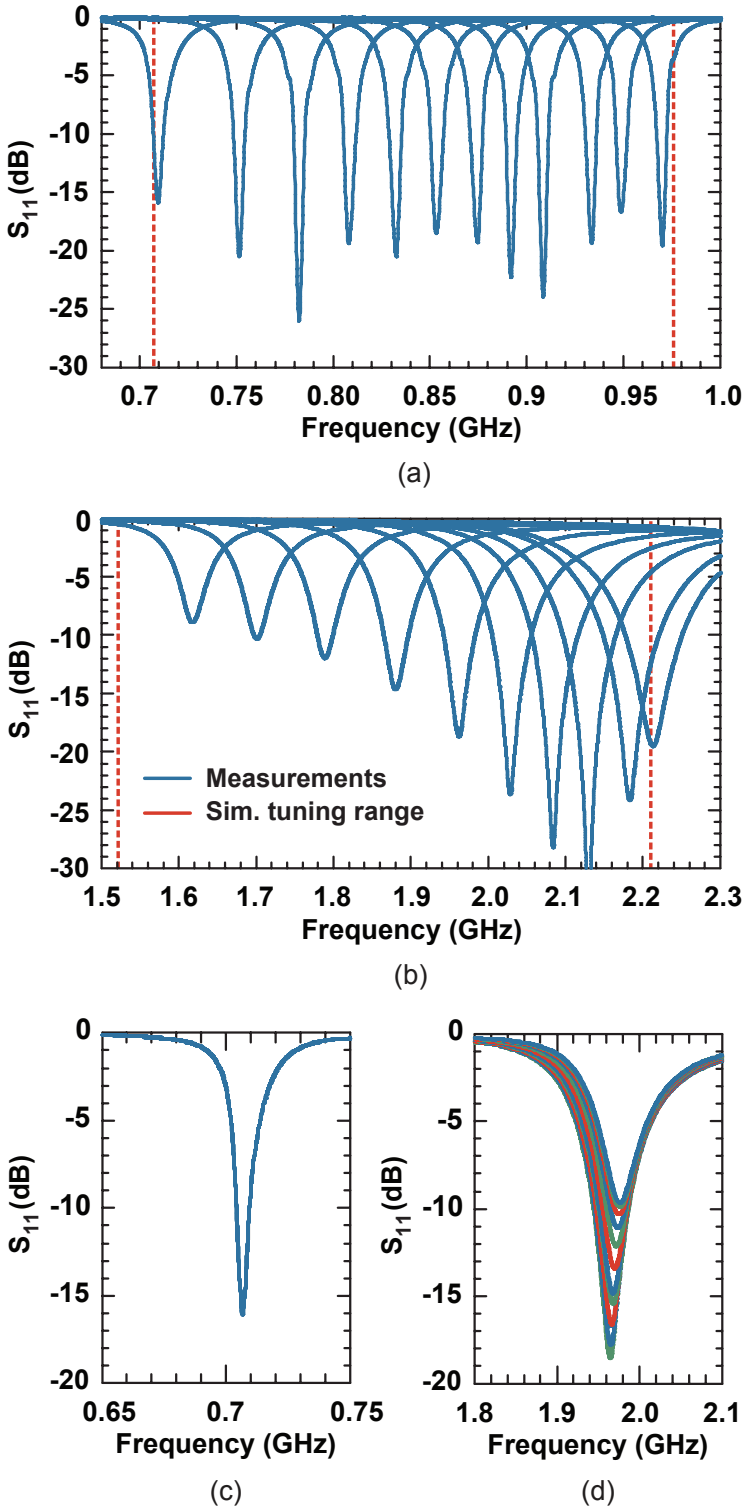

Figure 2.22: Measured S_{11} (a) at low band during low-band tuning, (b) at high band during high-band tuning, (c) at low band during high-band tuning and (d) at high band during low-band tuning.

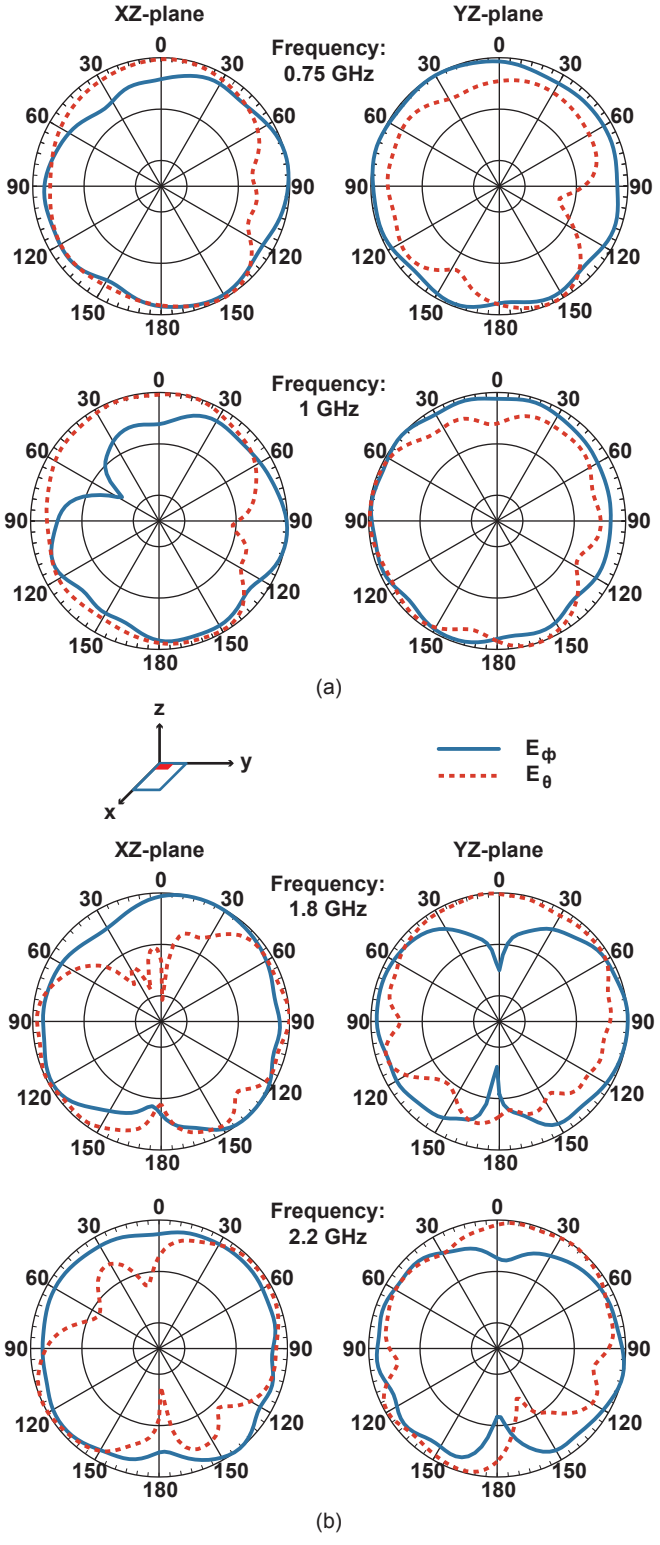

Figure 2.23: Measured radiation patterns at (a) low-band and (b) high-band.

2.7 Acknowledgement

This work was supported in part by the Center for Wireless Communications at the University of California, San Diego, and in part by the Defense Advanced Research Projects Agency (DARPA) N/MEMS S&T Fundamentals program under grant no. N66001-10-1-4006 issued by the Space and Naval Warfare Systems Center Pacific (SPAWAR). The authors would like to thank Qualcomm, Inc., San Diego, CA, for the use of their antenna pattern measurement system and to Dr. Kevin M. Ho for his kind assistance rendered with the pattern measurements.

Chapter 2 is mostly a reprint of the material as it appears in IEEE Transactions on Antennas and Propagation, 2015. Bilgehan Avser; Gabriel M. Rebeiz. The dissertation author was the primary author of this material.

Chapter 3

Random Feeding Networks for Reducing the Number of Phase Shifters in Limited-Scan Arrays

3.1 Introduction

Phased array systems have been widely used for radar and communications systems since the 1970s due to their ability to electronically scan the antenna beam [23]. The exponential increase in the computation power in the past decade has allowed for phased array designs using full-wave numerical techniques and computational optimization methods [24, 25]. On the hardware side, advances in the silicon RFIC and GaAs MMIC technologies resulted in reliable and relatively inexpensive phase shifters. Still, phase shifters and the underlying feed networks continue to be the most complex and expensive parts of phased array systems.

Phased array systems are usually employed in defense and satellite systems for high-data rate communications and radars [26–28]. These applications require narrow beams with low sidelobe levels that can scan in a wide field of view, and high performance is a more important design criteria than low-cost. However, in recent years, phased array systems are starting to be widely used for commercial applications such as automotive radars [29–31], landing systems [39, 40] and advanced robotic sensors. These applications usually require a narrower field of view and can tolerate higher sidelobe levels. However, due to the commercial nature of these applications, criteria such as low cost and low complexity are very important.

A conventional way to reduce the number of phase shifters for limited-scan applica-

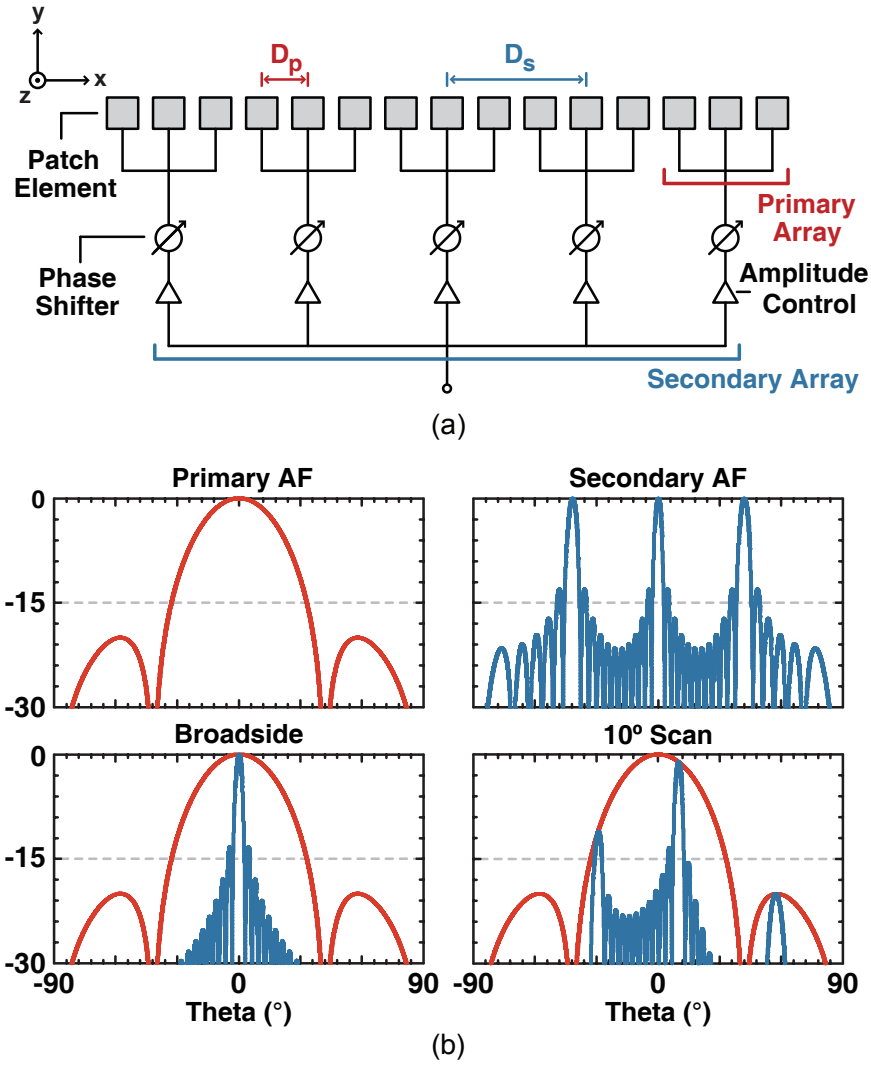

Figure 3.1: (a) Grouping of the elements in a uniform phased array and (b) primary array factor, secondary array factor, broadside scan total pattern and 10^o scan total pattern for a uniformly-grouped, 36 element linear array with $D_p = 0.5\lambda$ and $N_p = 3$.

tions is to divide the array into uniform sub-arrays and feeding each sub array with a single phase shifter [41, 42]. However, as the sub-array sizes are increased (i.e., less phase shifters are used), grating lobes start to enter the visible space and cause the side-lobe level to increase abruptly, and this results in poor scan performance. One way to overcome this problem is by using overlapping subarrays [43–46]. However planar implementation of phased arrays with overlapping sub-arrays is rather problematic due to the smaller inter-element spacing and multiple RF crossings in the feed network. These feed networks are lossy, relatively complex and not scalable to mm-wave frequencies.

In this chapter, a new method based on using non-uniform element grouping is proposed to increase the scanning performance of limited-scan arrays without a complex feed network. Instead of using a uniform sequence of identical primary arrays, a random sequence of primary arrays with different number of groupings is used. The order of the random sequences is optimized to result in the largest scan-angle with grating lobes less than a desired limit. Section II presents the theoretical analysis and design methodology of the random arrays. Optimized designs for multiple cases are presented to provide design guidelines. Section 3.3 presents a planar implementation of the random arrays at 7.9 GHz with 30 elements and 12 phase shifters. Compared to uniform arrays, the random arrays reduce the number of phase shifters by up to 40% and operate well over a wider bandwidth.

A method for synthesizing 2-D random arrays is also presented. The random 2-D arrays reduce the number of phase shifters by up to 60% compared to uniformly grouped 2-D arrays, while preserving the same performance over a limited scan angle.

3.2 Random Phase Grouping Arrays

3.2.1 Theory

An in-phase current distribution on a linear antenna array results in a symmetrical broadside array factor. If a linear-progressive phase is added on each antenna element along the array axis, the array factor may be scanned to virtually any angle, up to the grating lobes given by the element spacing. In general, the elements are spaced at 0.5λ-0.55λ so as to allow scanning $> 50^o$. A conventional way to reduce the number of phase shifters is to use the sub-arrays [41, 42].

Fig. 3.1(a) represents a 3-element sub-arraying configuration where the antennas are grouped into sub-arrays fed using a single phase shifter. The linear phase progression is herein

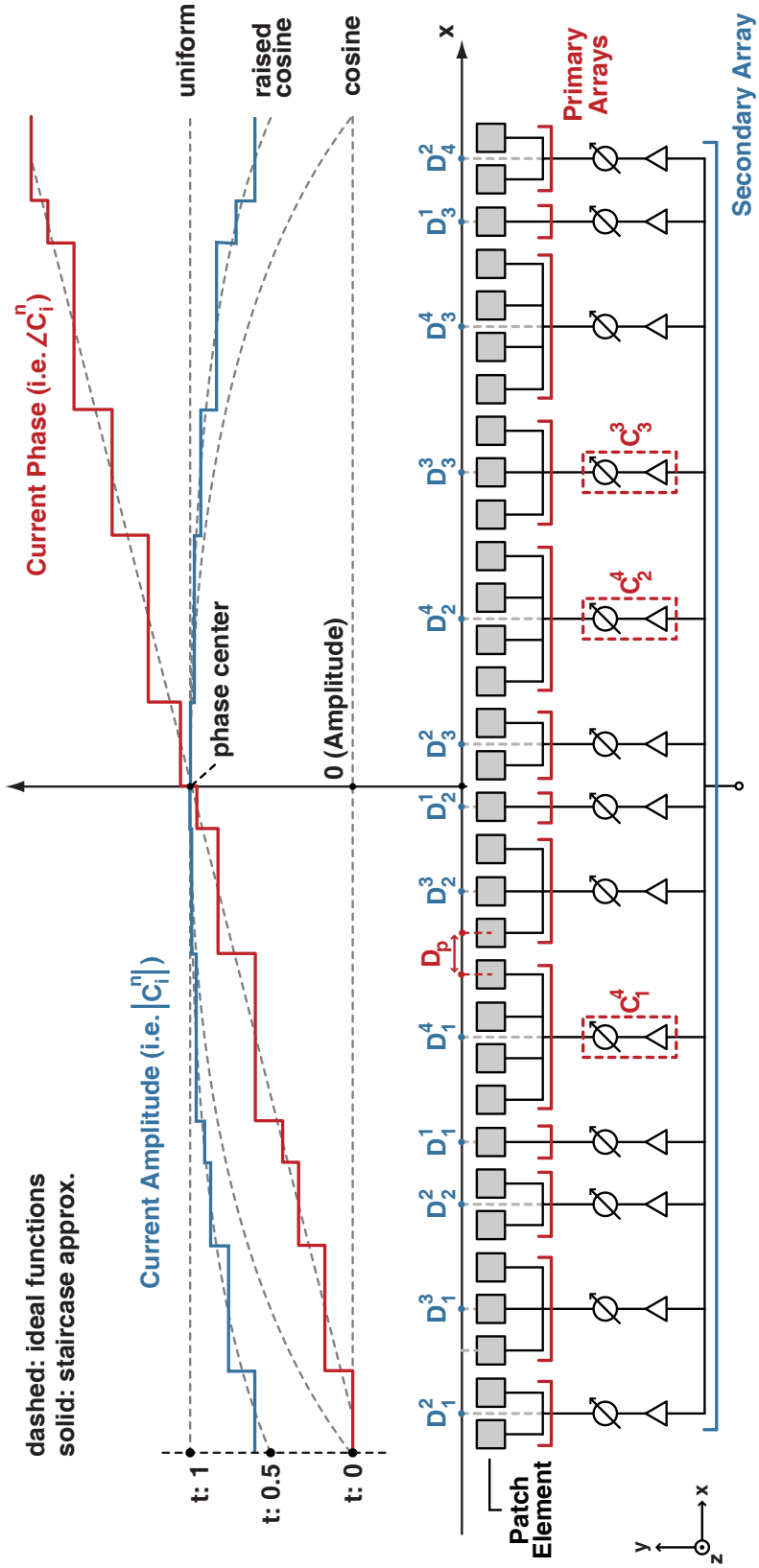

Figure 3.2: Grouping of the elements, amplitude tapering and beam steering in a non-uniform random phased array.

replaced with a staircase approximation. The array factor AF can be expressed as the product of two independent array factors AF_p and AF_s

$$AF(\theta, \phi) = AF_p(\theta, \phi) \times AF_s(\theta, \phi) \tag{3.1}$$

where θ represents the angle with respect to the z-axis. AF_p is the primary array factor representing the array group and is given by

$$AF_p(\theta, \phi) = \frac{sin\left(N_p \pi \frac{D_p}{\lambda} sin\theta cos\phi\right)}{N_p sin\left(\pi \frac{D_p}{\lambda} sin\theta cos\phi\right)} \tag{3.2}$$

where λ is the wavelength, N_p is the number of elements and D_p is the inter-element spacing in the primary array. AF_s is the secondary array factor representing the discretization of phase distribution at the phase centers of the primary arrays and is given by

$$AF_s(\theta, \phi) = \frac{sin\left(N_s\left(\pi \frac{D_s}{\lambda} sin\theta cos\phi + \alpha\right)\right)}{N_s sin\left(\pi \frac{D_s}{\lambda} sin\theta cos\phi + \alpha\right)} \tag{3.3}$$

where N_s is the number of elements, D_s is the inter-array spacing, and α is the progressive phase shift used to scan the beam to θ_{peak} and is given by

$$\alpha = \frac{-\pi D_s sin\theta_s}{\lambda}. \tag{3.4}$$

For a uniformly-grouped array

$$D_s = N_p \times D_p \tag{3.5}$$

and one phase shifter per D_s (i.e., primary array) is used. The overall radiation pattern of the whole system, $P(\theta, \phi)$, is calculated as

$$P(\theta, \phi) = AF(\theta, \phi) \times EP(\theta, \phi) \tag{3.6}$$

where $EP(\theta, \phi)$ is the element pattern of a single antenna.

Both $AF_p(\theta,\phi)$ and $AF_s(\theta,\phi)$ components of $AF(\theta,\phi)$ are periodic functions of θ, which causes grating lobes to occur when the array is scanned. However only a portion of these grating lobes fall into the visible space, $-\pi/2 \leq \theta \leq \pi/2$. For the secondary array, the inter-element spacing, D_s is proportional to the number of elements in the primary array, N_p. Thus, as more elements are grouped into the primary array (i.e., less phase shifters are used), the number of grating lobes inside the visible space increases in $AF_s(\theta,\phi)$. For the broadside condition ($\alpha = 0$), it is not possible to trigger grating lobes in the overall pattern since the primary AF_p nulls occur on the top of the secondary AF_s grating lobes. However, as a phase shift, α, is applied, $AF_s(\theta,\phi)$ scans to θ_s whereas the $AF_p(\theta,\phi)$ and $EP(\theta,\phi)$ remains constant with their peaks at broadside. This causes the cancellation effect to disappear and results in poor scan performance with high sidelobes (i.e., grating lobes). This is demonstrated in Fig. 3.1(b) for a 36-element linear array with $D_p = 0.5\lambda$, $N_p = 3$ ($D_s = 1.5\lambda$, $N_s = 12$). In this case the array can scan only $\pm 6^\circ$ before the grating lobes exceed $-15\,dB$.

For non-uniform primary arrays, the overall array factor can no longer be expressed as the multiplication of two array factors. Instead it must be calculated as a summation of multiple array factors, one for each type of primary array. If an array with equal spacing between individual antenna elements is considered, the overall array factor $AF(\theta,\phi)$ is given by

$$AF(\theta,\phi) = \sum_n AF_n^p(\theta,\phi) AF_n^s(\theta,\phi) \tag{3.7}$$

where

$$AF_n^p(\theta,\phi) = \frac{sin\left(n\pi\frac{D_p}{\lambda}sin\theta cos\phi\right)}{nsin\left(\pi\frac{D_p}{\lambda}sin\theta cos\phi\right)} \tag{3.8}$$

$$AF_n^s(\theta,\phi) = \sum_{i=1}^{K_n} C_i^n e^{j\frac{2\pi}{\lambda}D_i^n sin\theta cos\phi} \tag{3.9}$$

and n is the number of elements in a primary array, i is the index of the primary array, K_n is the number of primary arrays with n elements, D_i^n is the phase center of the i^{th} primary array group with n elements. The final radiation pattern of the array is given by the multiplication of the overall array factor $AF(\theta,\phi)$ and the element pattern of the individual antennas $EP(\theta,\phi)$. The total number of individual antennas, K_{tot}, is given by

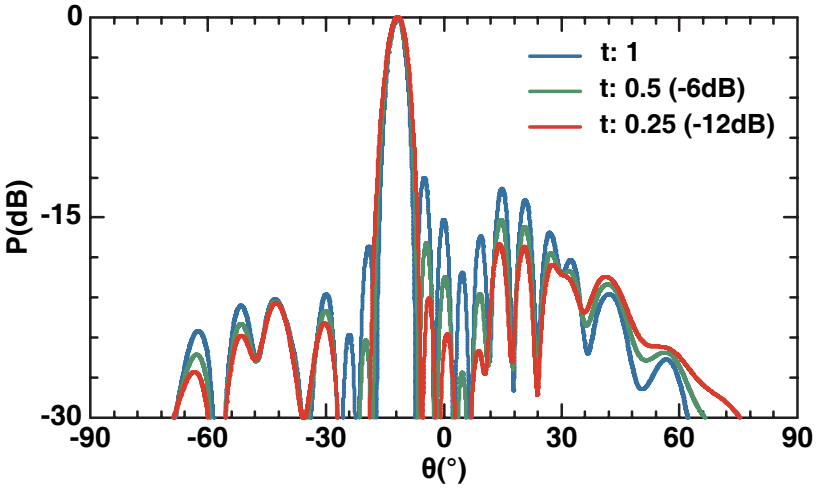

Figure 3.3: Normalized radiation patterns with different levels of raised cosine tapering for 10^o scan for a random grouping array of 1, 2 and 3 elements.

$$K_{tot} = \sum_n nK_n \tag{3.10}$$

the total number of phase shifters, PS, is given by

$$PS = \sum_n K_n \tag{3.11}$$

and the total aperture length of the array, L_{tot}, is given by

$$L_{tot} = K_{tot} * D_p. \tag{3.12}$$

A new parameter, equivalent sub-array size per shifter, ESS, is defined as

$$ESS = L_{tot}/PS \tag{3.13}$$

and provides a metric for comparison for the random array designs. $ESS = D_p$ corresponds to a standard array where each antenna is fed with one phase shifter whereas $ESS = 3D_p$ corresponds to a uniformly-grouped array with 3-element sub-arrays.

The main beam is scanned by applying a phase shift to the primary array groups (Fig. 3.2), and for a scan angle θ_{peak}, is calculated as

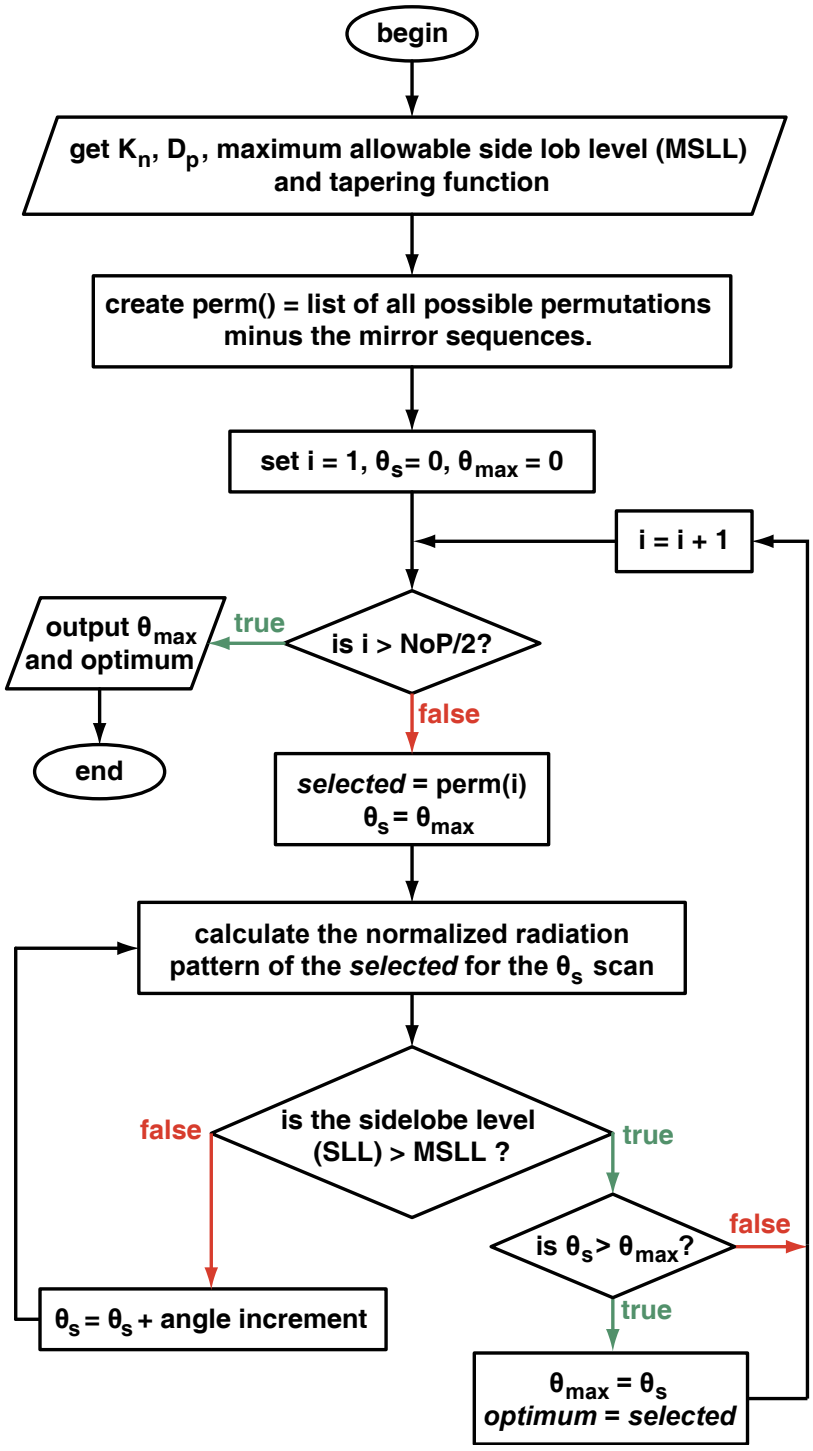

Figure 3.4: Flowchart of the optimization algorithm.

$$\angle C_i^n = -\frac{2\pi D_i^n sin(\theta_{peak})}{\lambda} \tag{3.14}$$

Amplitude tapering is applied by adjusting the power into each primary array. The power levels are determined by defining a taper function over the array and calculating its value at the center of the primary arrays. This creates a staircase approximation to the ideal taper function (Fig. 3.2). For a raised cosine taper, the current amplitude level at the primary arrays is calculated as

$$|C_i^n| = p\left(t + (1-t)\,cos\left(\frac{\pi D_i^n}{L_{tot}}\right)\right) \tag{3.15}$$

where t is the edge taper level ($t = 1$ uniform, $t = 0$ cosine distribution). The factor p in (3.15) is $\sqrt{n}$ for the equal power approach and n for the uniform current approach (See Section II. B.). Fig. 3.3 presents the effect of the raised cosine taper on the radiation pattern. For random arrays, the edge taper reduces both the sidelobes adjacent to the main beam and the spurious grating lobes that occur during scanning.

3.2.2 Random Array Design and Optimization

In our simulations, the primary array groups are composed of 1, 2, 3 and 4 elements, each with equal spacing D_p (Fig. 3.2). The resulting arrays can scan up to $\pm 20^\circ$ with grating lobes below -15 dB. This scan region is too small to trigger scan blindness modes, or to result in large variations in the active element S_{11}. Therefore, when calculating the array patterns, the mutual coupling between the antennas is not taken into account.

There are two ways to design arrays based on random grouping of primary-array groups.

Equal power for sub-arrays

If no edge taper is assumed (i.e. $t = 1$), each of the primary arrays is fed with equal power, $P_\circ$. In this case, the current magnitude on an individual antenna element is inversely proportional to$\sqrt{n}$ and the peak radiation intensity of a primary array is directly proportional to n (Directivity $\propto n$ for each primary array). Taper is applied as in (3.15) with $p = \sqrt{n}$.

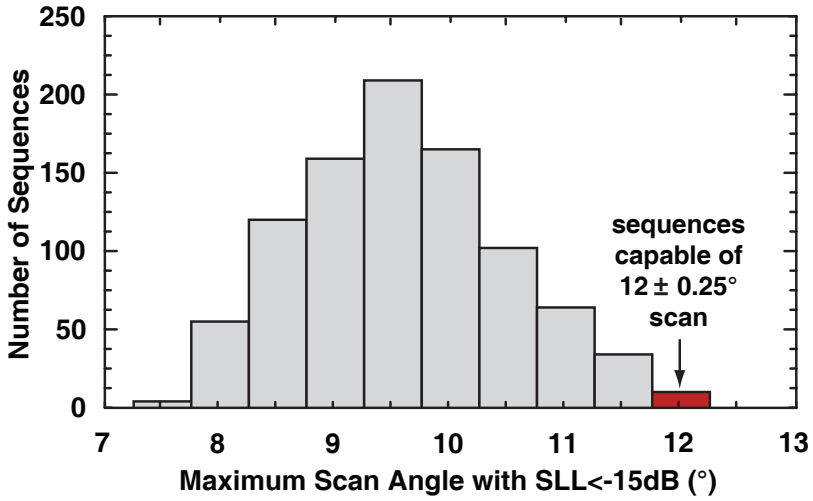

Figure 3.5: Histogram of all possible sequences for $K_{tot} = 30$, $D_p = 0.5\lambda$, $PS = 12$, $K_2 = 6$, $K_3 = 6$, $NoP = 924$.

Uniform current on each antenna

If no edge taper is assumed, each primary array is fed with a power $P_i^n = nP_\circ$. This creates a uniform current magnitude on each individual antenna. In this arrangement, the peak radiation intensity of a primary array is proportional to n^2 (Directivity $\propto n$, $P_i^n \propto n$ for each primary array). Taper is applied as in (3.15) with $p = n$.

The half-power beamwitdh (HPBW) and the array directivity is determined by the array size, L_{tot}. The first step in the design procedure is to determine the number of individual elements and inter-element spacing which results in the desired HPBW.

Then, the type and quantity of the primary array groups is chosen based on the desired number of phase shifters. The sequence of the primary array groups significantly affects the array performance, hence the best sequence needs to be determined for optimal performance (i.e. maximum scan angle with sidelobes below a desired limit). An algorithm which analyzes all possible combinations is developed in MATLAB, and its flow chart is shown in Fig. 3.4. The program takes the types and quantities of the primary array groups (i.e., K_n), inter-element spacing D_p, the taper function and the maximum allowable side-lobe level (MSLL) as inputs, and outputs the maximum allowable scan angle and the optimum sequence of the primary array groups. For the given set of primary arrays, all possible permutations are calculated. The total number of these permutations, NoP, is given by

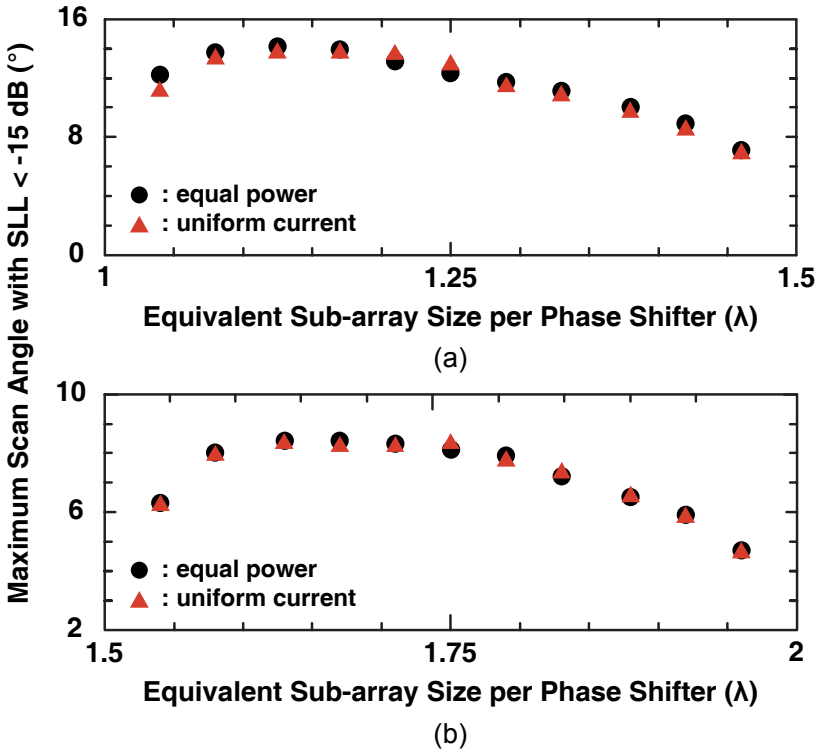

Figure 3.6: Maximum scan angle with sidelobes less than -15 dB versus equivalent sub-array size per phase shifter. Optimum sequences are composed of (a) 2 & 3-element primary array groups and (b) 3 & 4-element primary array groups. Calculations are for 12 phase shifters and $D_p = 0.5\lambda$.

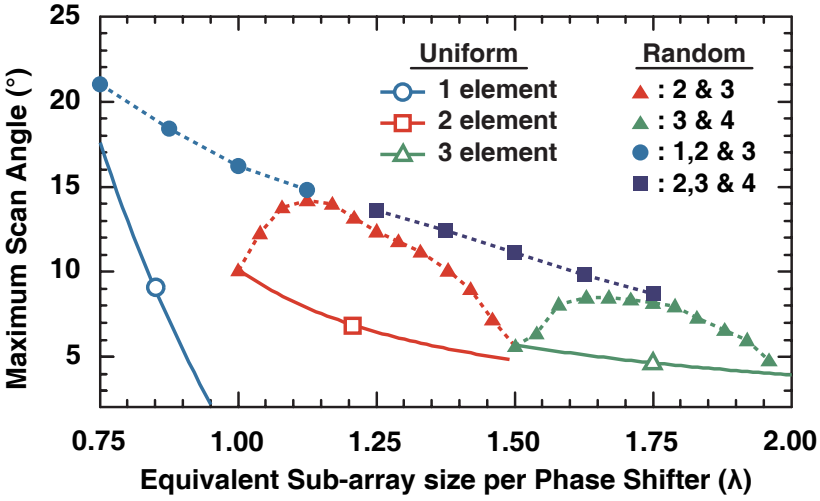

Figure 3.7: Maximum scan angle with sidelobes less than -15 dB versus equivalent sub-array size per phase shifter, for optimum sequence of arrays using a combination of 1,2,3 and 4 element sub-arrays with $D_p = 0.5\lambda$ and 12 phase shifters.

$$NoP = K_{tot}! \bigcup_{n} \frac{1}{(K_n)!}. \tag{3.16}$$

However, only the half these permutations need to be tested due to symmetry. This is due to the fact that an array and its mirror image with respect to the origin (such as arrays produced by sequences "2-3-2-4-2-2" and its mirror image "2-2-4-2-3-2") have identical patterns. After a list of all permutations is created, the first sequence (i.e. permutation) is selected, and its normalized radiation pattern is calculated for the broadside scan. Then the main beam is steered in small angle increments (typically 0.1^o) until the sidelobe level (SLL) exceeds the $MSLL$. This scan angle is recorded as the current maximum scan angle and the selected sequence is recorded as the current optimum sequence. Due to symmetry, $AF_n^p(\theta, \phi) = AF_n^p(-\theta, \phi)$ and AF_n^s produces mirror-image patterns when scanning $\pm\theta_{peak}$. Therefore, the overall radiation patterns when scanned $\pm\theta_{peak}$ are mirror-image patterns, and it is sufficient to test the array for only half of the space (i.e., $0 < \theta_s < \pi/2$). The same process is then run for all other random sequences. If a sequence that scans to a higher angle without exceeding the $MSLL$ is found, that scan angle is recorded as the current maximum scan angle and that sequence is recorded as the current optimum sequence. The SLL of the random arrays increase monotonically as the main beam is steered to higher angles. Hence, when the sequence which scans up to a maximum scan angle, θ_{max}, with $SLL < MSLL$ is found, the rest of the sequences only need to be calculated for scan angles $> \theta_{max}$. Thus, instead of starting the beam at broadside and steering to higher angles, the simulation can be started at θ_{max} and steered forward on. This method significantly reduces the computation time, since after a high performance array sequence is found, the poor performance sequences are quickly eliminated.

For an array built using microstrip patch antennas on $\epsilon_r = 3.55$ (Rogers RO4003) and with $K_{tot} = 30$ elements, $D_p = 0.5\lambda$, $PS = 12$, and $K_2 = 6$, $K_3 = 6$ (i.e., six 2-element sub-arrays, six 3-element sub-arrays, a phase shifter every 1.25λ), there is $NoP = 924$ possible sequences. The MATLAB program is run on a 64-bit Windows system with 8 GB of RAM and a 3.40 GHz CPU and requires 10 seconds to determine the optimum sequence which can scan up to 12.3^o with $SLL < -15$ dB (a -12 dB taper is used on the array). Fig. 3.5 presents the histogram of all possible primary array sequences: 5% of all sequences can scan up to 11.3^o and the 12% of all sequences can scan up to 10.8^o. If K_{tot} is increased to 40, $PS = 16$, $K_2 = 8$, $K_3 = 8$ are used, $NoP = 12,870$ and an optimum sequence is determined in 150 seconds. The computational load increases significantly when more than two types of primary arrays are used.

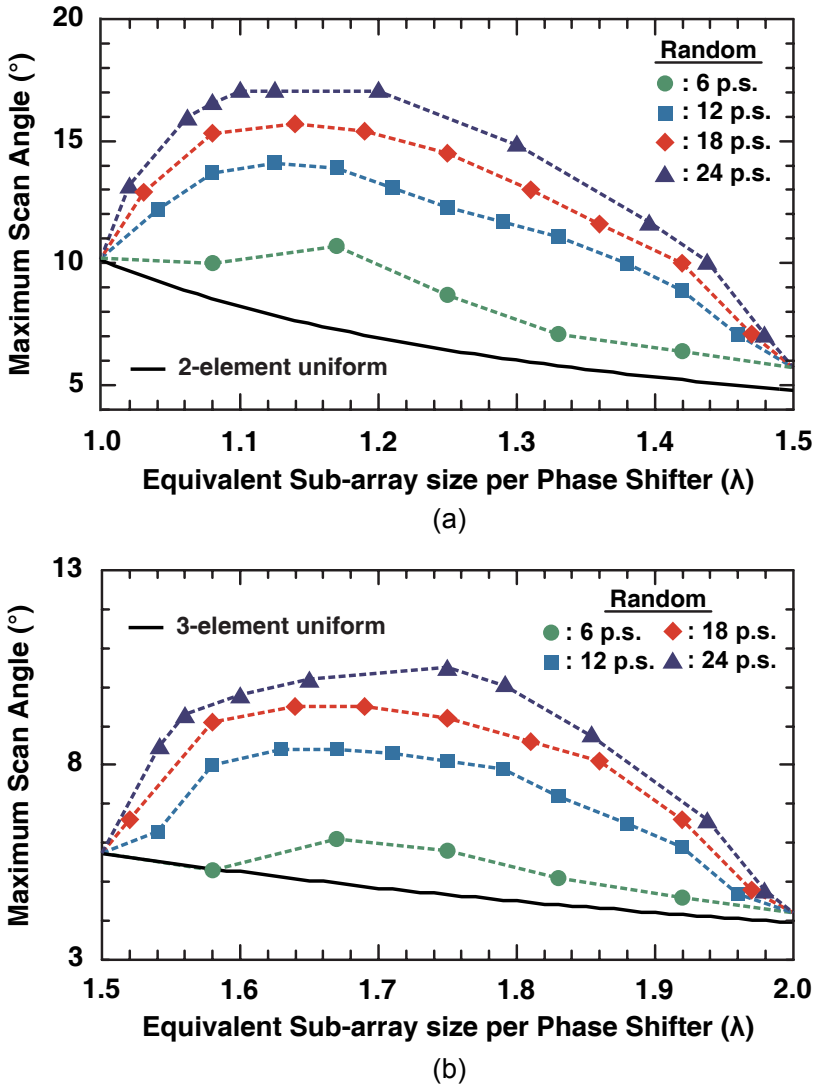

Figure 3.8: Maximum scan angle with sidelobes less than -15 dB versus equivalent sub-array size per phase shifter, for optimum sequence of arrays using a combination of (a) 2 and 3-element and (b) 3 and 4-element primary arrays with $D_p = 0.5\lambda$ and different number of phase shifters.

For an array with $K_{tot} = 36$, $D_p = 0.5\lambda$, $PS = 12$, $K_2 = 4$, $K_3 = 4$, $K_4 = 4$, $NoP = 34,650$ and a solution is found in 5.5 minutes. To push the computational limit, a case with $K_{tot} = 45$, $D_p = 0.5\lambda$, $PS = 15$, $K_2 = 5$, $K_3 = 5$, $K_4 = 5$ is optimized. For this case, $NoP = 756,756$ and the solution time is 2.5 hours.

3.2.3 Random Array Performance and Design Guidelines

The equal power excitation and the uniform current excitation are compared over two cases:

$Case\ I : PS = 12$ with 2 and 3-element primary arrays.
$Case\ II : PS = 12$ with 3 and 4-element primary arrays.

The phase shifters can be distributed in $NoP + 1$ ways, where two of these configurations corresponds to the uniform sub-arraying (i.e., the array is entirely composed of one kind of primary array). The maximum scan angle is computed for $MSLL = -15$ dB (a 12 dB amplitude taper is used). Each configuration corresponds to a different equivalent sub-array size per phase shifter (ESS) as described in (3.13). Fig. 3.6 presents the maximum scan angle versus ESS for cases with 2 and 3-element primary arrays and with 3 and 4-element primary arrays. Even tough the sequences of primary array groups resulting in the maximum scan angle are different for the equal power and uniform current excitations, the performance of the both excitations are similar. Throughout the paper, the focus is shifted towards the uniform current approach since it presents a more accurate comparison with a uniform array.

The uniform microstrip arrays are compared with random arrays over four cases with $PS = 12$:

$Case\ A$: 2 and 3-element primary arrays.
$Case\ B$: 3 and 4-element primary arrays.
$Case\ C$: 1, 2 and 3-element primary arrays.
$Case\ D$: 2, 3 and 4-element primary arrays.

Each case has multiple configurations depending on the number of different primary array groups ($Case\ A$ and $Case\ B$: 13 different configurations, $Case\ C$ and $Case\ D$: 91 different configurations). Each configuration has also multiple possible sequences, NoP, which are optimized

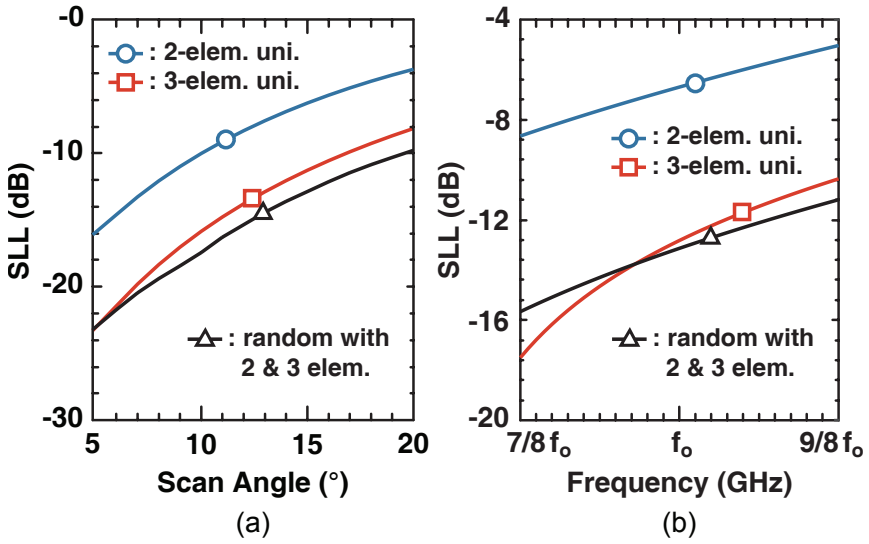

Figure 3.9: (a) SLL versus scan angle and (b) SLL versus frequency for the optimum random array with $N_{tot} = 30$, $PS = 12$ and $K_2 = 6$, $K_3 = 6$, the 30-element uniform array with $PS = 15$ and for the 30-element uniform array with $PS = 10$.

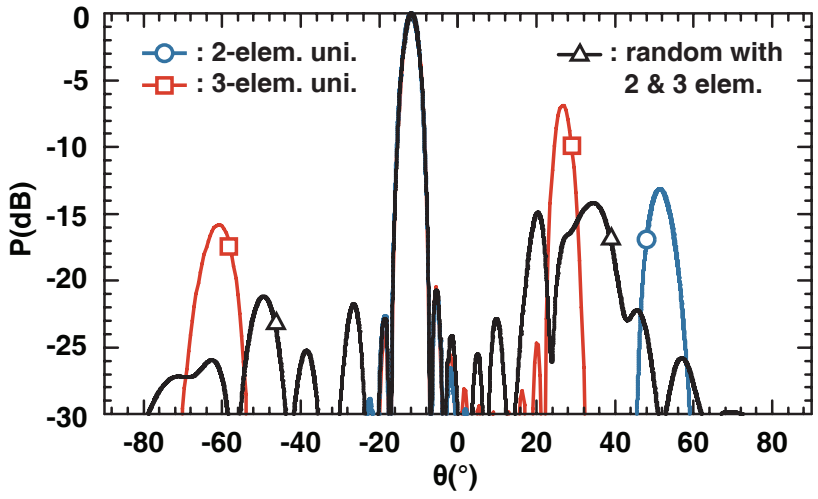

Figure 3.10: Radiation patterns for 12° degree scan of the optimum random array with $N_{tot} = 30$, $PS = 12$ and $K_2 = 6$, $K_3 = 6$, the 30-element uniform array with $PS = 15$ and for the 30-element uniform array with $PS = 10$.

using the MATLAB program.

Fig. 3.7 presents the maximum scan angle versus ESS for the uniform microstrip arrays and for the optimized random sequences. The best performance is obtained from the random arrays containing three primary arrays groups with (1, 2, 3) and (2, 3, 4) elements elements since these cases utilize the randomness factor the most. It is found that, random phase-grouping arrays reduce the number of phase shifters up to 40% when compared to uniformly-grouped designs.

$CaseA$ (2 and 3-element primary arrays) and $CaseB$ (3 and 4-element primary arrays) are also analyzed for different number of phase shifters as shown in Fig. 3.8. For $Case\ A$, the random array converges to the uniform microstrip array when ESS is 1 and 1.5. This is because at these ESS values, all of the primary arrays should have either 2 elements or 3 elements which correspond to the uniform grouping case. Similarly for $Case\ B$, the random arrays converge to the uniform case when ESS is 1.5 and 2. The maximum performance improvement is observed when the number of the different element primary array groups are approximately equal since these cases result in the most randomness. Also as the number of phase shifters increase, the scanning performance increases since these cases utilize randomness more effectively.

A 30-element random array with $PS = 12$, $K_2 = 6$, $K_3 = 6$ and an optimum sequence is compared to two different uniformly grouped arrays; a 30-element array using 2-element and 3-element sub-arrays with 15 and 10 phase shifters, respectively (Fig. 3.9). For these arrays, $D_p = 0.5\lambda$ and $L_{tot} = 15\lambda$.

The random array uses less phase shifters than the 2 and 3-element uniform arrays and has better performance versus scan angle. Also, the random array sidelobe levels increases versus frequency at a slower slope than the uniform 2 & 3-element arrays (Fig. 3.9 (b)). Fig. 3.10 presents the radiation patterns for 12° scan for these arrays with a -12 dB taper. As expected, the uniform arrays with 2 elements and 3 elements have higher SLL than the random array.

3.3 Planar Implementation

A 30-element linear array is fabricated at 7.9 GHz with 12 phase shifters using an equal number of 2- and 3-element primary arrays ($K_2 = 6, K_3 = 6$). The design frequency is selected as 7.9 GHz since it is 1:10 ratio of 79 GHz band, which is allocated to automotive radar systems. The random grouping used is "2-2-2-3-2-2-3-3-2-3-3-3", and results in 0.5 dB higher SLL than the optimum grouping "3-2-2-3-2-2-2-2-3-3-3-3". This choice is due to using an earlier version of the optimization program which used a larger angle increment. The spacing

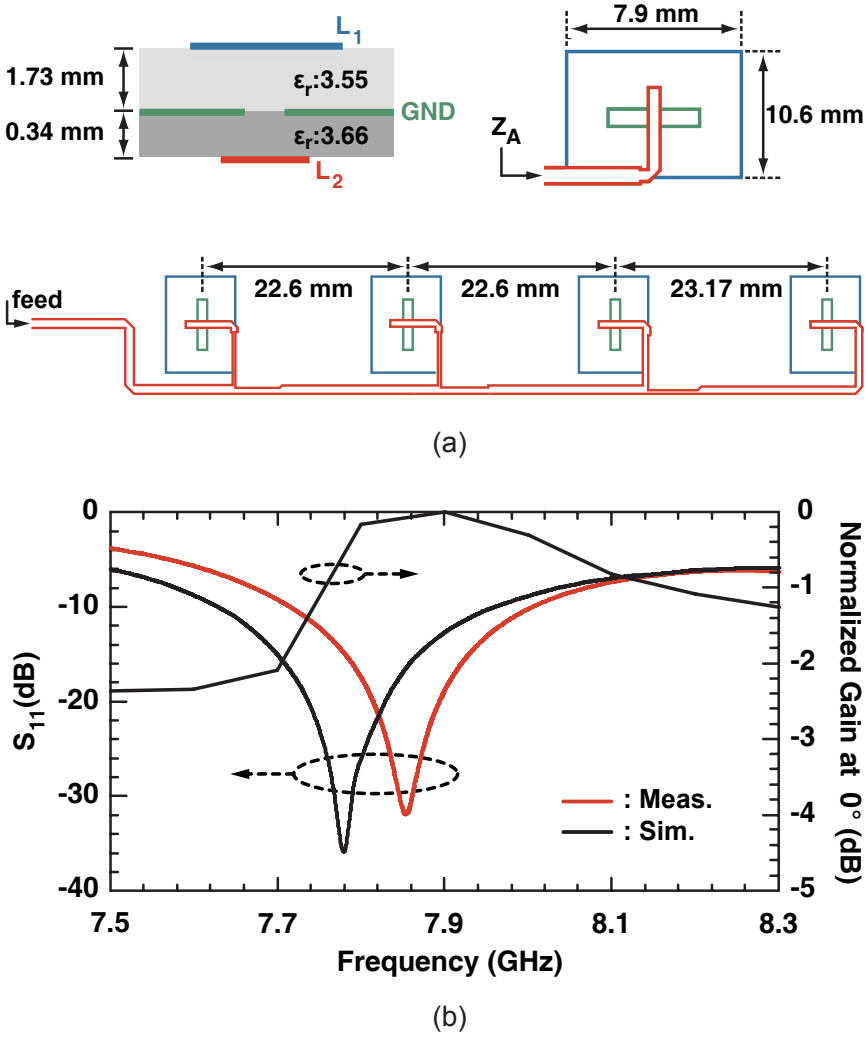

Figure 3.11: (a) Board stack-up, single antenna and series element geometry and (b) impedance match and normalized gain for the 4-element antenna.

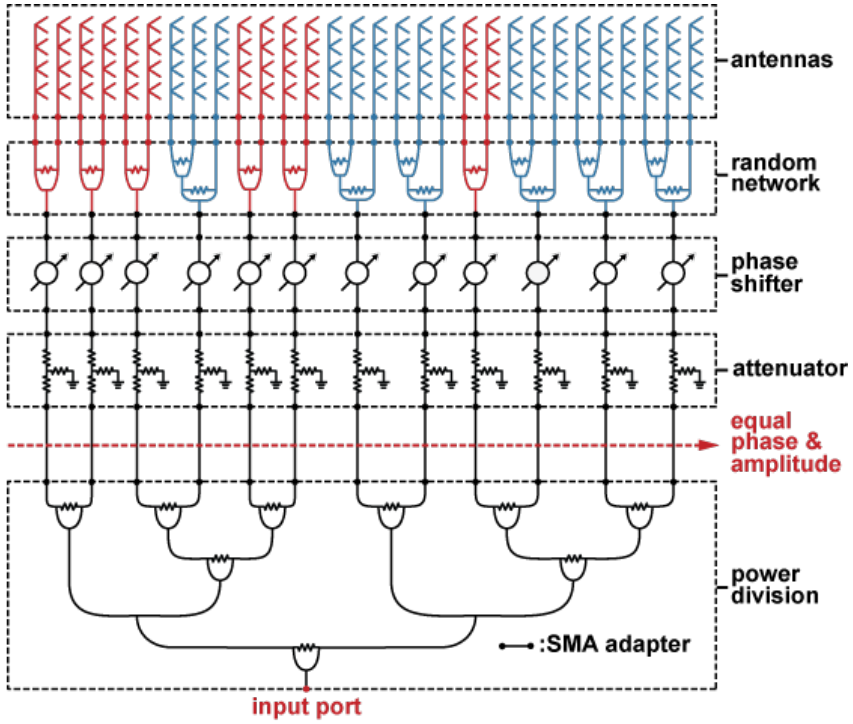

(a)

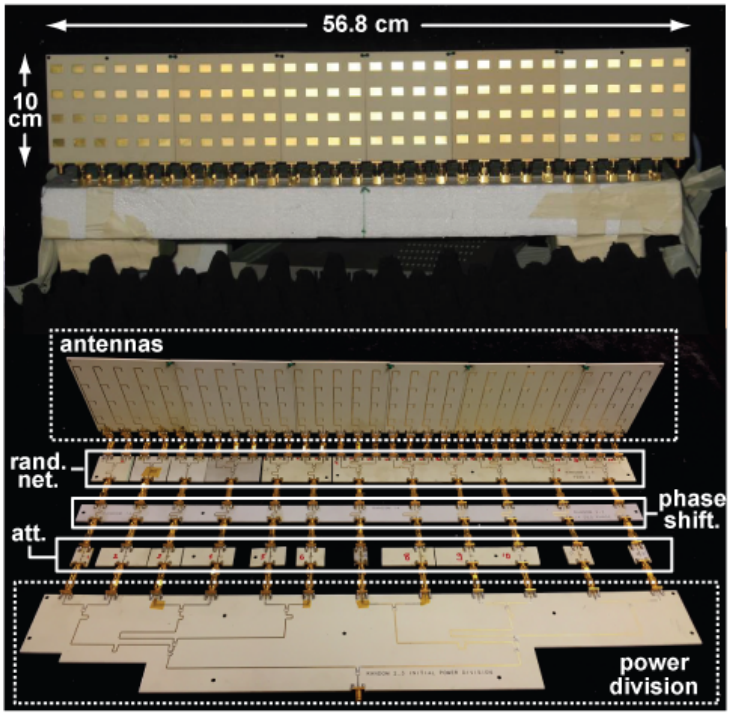

(b)

Figure 3.12: (a) Schematic for the planar implementation of the selected random array, (b) fabricated array.

between individual antennas, D_p, is 0.5λ and the equivalent sub-array size, ESS, is 1.25λ (on average one phase shifter feeds 2.5 antennas), resulting in a total aperture length, L_{tot}, of 15λ.

3.4 Experimental Results

The linear array elements are based on four series-fed microstrip antennas on the vertical axis built on a stack of 1.73 mm-thick RO4003 ($\epsilon_r = 3.55$) and 0.34 mm-thick RO4350 ($\epsilon_r = 3.66$) with a ground plane in between (Fig. 3.11(a)). The phase shifters, attenuators and power dividers are constructed on a 0.34 mm-thick RO4350 using the L_2 layer. The simulated and measured antenna impedance and measured normalized gain at broadside for the series-fed array are shown in Fig.3.11(b). The bandwidth is limited by the impedance match and by the beam squint versus frequency due to the 360^o transmission-line sections between patches. The 30-element array can only scan in the horizontal plane and has a fixed beam in the vertical plane (4-elements). The array is designed with uniform current excitation as described in Section 3.2.2 and a raised cosine tapering of $-12dB$ (i.e., $t = 0.25$) is used.

Fig. 3.12 (a) presents the general structure of the test array. The input power is divided using a 1-to-12 power divider board consisting of a cascaded un-equal Wilkinson network. The board outputs have equal magnitude and equal phase. The taper is then applied using a 12-to-12 attenuator board with 12 matched T-pad attenuators realized using 0402 resistors. The output of the attenuator board is connected to a 12-to-12 phase-shifter board. The phase shifts are realized using different length transmission lines, and are therefore true-time delay units. There are six different phase shifter boards that result in fixed 0°, 3°, 6°, 9°, 12° and 14° scans. The outputs of the phase shifter board are connected to the 12-to-30 random feeding board which contains the random sequence of 1-to-2 and 1-to-3 equal power dividers. Finally the output of the random feeding board is connected to the antenna board. The fabricated prototype array is shown in Fig. 3.12 (b).

Radiation pattern measurements are performed in an anechoic chamber where the distance between the DUT and the measurement antenna is 7.5 m and corresponds to half of the far-field limit. However, far-field simulations are performed and it is concluded that the patterns and peak power measurements will be nearly equal to the actual far field-patterns. Fig. 3.13 presents the measured and simulated normalized patterns for 0°, 3°, 6°, 9°, 12° and 14° scans. The array can scan up to $\pm 14^\circ$ with grating lobes lower than -15 dB. In comparison, a 30 element uniformly-grouped array with 12 phase shifters (using 2-element primary array groups with $D_p = 0.625\lambda$ to result in the same $L_{tot} = 15\lambda$) can only scan up to $\pm 6.5^\circ$.

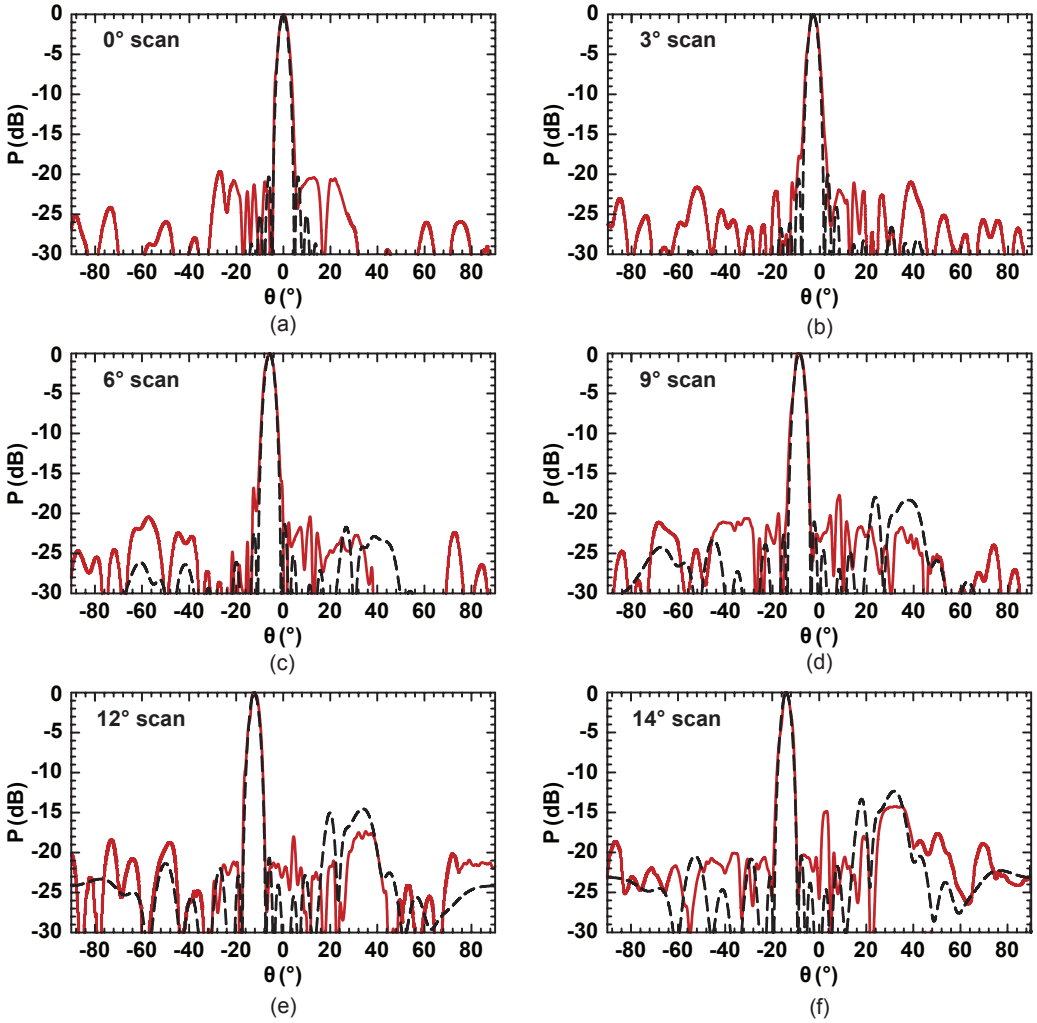

Figure 3.13: Normalized measured and calculated radiation patterns versus θ for (a) 0^o, (b) 3^o, (c) 6^o, (d) 9^o, (e) 12^o, and (f) 14^o scans. Solid lines are measured and dashed lines are calculated.

Table 3.1: Loss of the Fabricated Random Array at 7.9 GHz

Part	**Loss (dB)**
Power divider board	5.55
Attenuators (incl. 12 dB taper)	3.8
Phase shifters	0.85
Random feeding network	1.1
4-Element vertical patch array	2.0
Total loss without phase shifters (0° scan)	12.35
Total loss with phase shifters	13.2

Fig. 3.14 presents the measured antenna system gain referenced to the input port for 0°, 3°, 6°, 9°, 12° and 14° scans at 7.9 GHz. The received peak powers drop by 2 dB due to the 2 and 3-element primary-array patterns. Due to this effect, it is not practical to use sub-array groups larger than 4-elements.

The losses for each board is extracted from individual S-parameter measurements and are presented in Table 3.1. The total measured loss is 12.35 dB at the broadside scan and is 13.2 dB at other scan angles, since the phase shifters are not used at the broadside scan. The measured antenna gain at 0° scan, referenced to the input power, is 10 dB at 7.9 GHz. If the measured loss of 12.35 dB is extracted from this value, the measured directivity is found to be 22.35 dB. This agrees well with the simulated directivity of 22.63 dB. The random feeding network has a loss of 1.1 dB due to the power dividers. However, this loss will still exist in a conventional 2 or 3-element uniform-array design, since power dividers are still needed after the phase shifters (see Fig. 3.1 (a)).

Fig. 3.15 presents the normalized measured peak powers versus frequency for 0°, 3°, 6°, 9°, 12° and 14° scans. The normalized peaks powers are > -2 dB at 7.6-8.1 GHz. The drop outside of this band is due to the inherent bandwidth of the 4-element vertical antenna (see Fig. 3.11).

Fig. 3.16 presents the normalized radiation patterns at 7.6 GHz and 8.1 GHz for the 14^o degree scan. The main beam gets sharper for the higher frequencies since the aperture size increases electrically. Since the inter-element spacing also increases, the grating lobes are observed more strongly for the high frequencies. Still, these results are much better than uniform

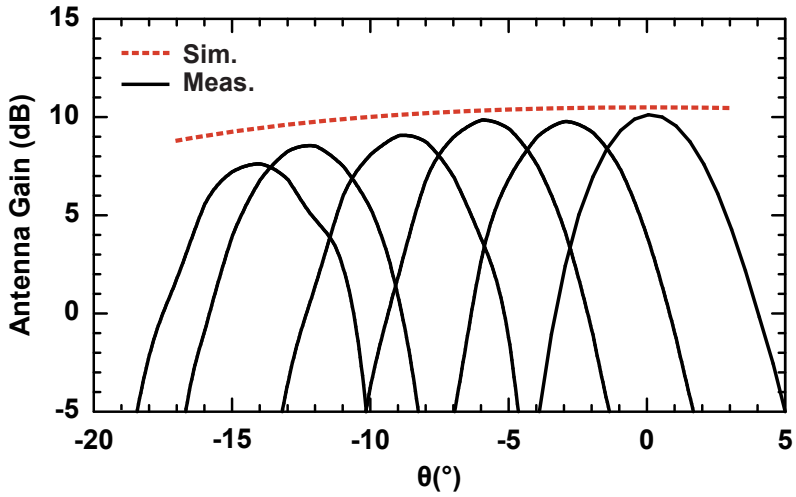

Figure 3.14: Measured antenna system gain at 7.9 GHz, referenced to the input port for 0^o, 3^o, 6^o, 9^o, 12^o and 14^o scans. All losses are included.

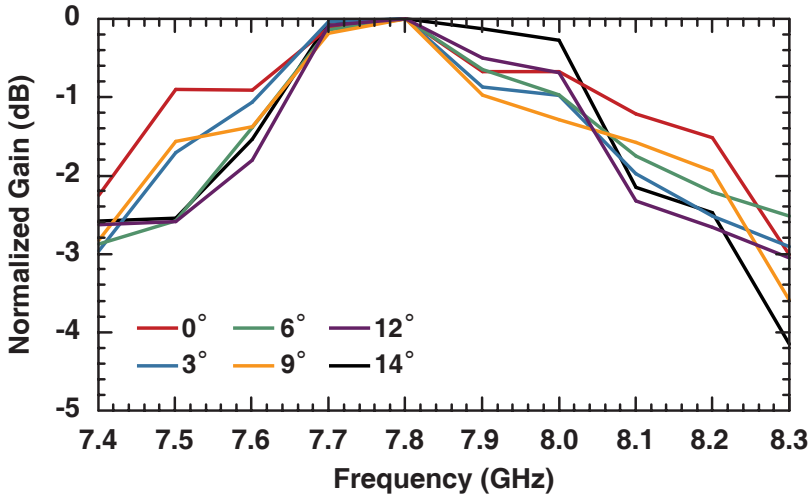

Figure 3.15: Normalized measured peak power versus frequency for 0^o, 3^o, 6^o, 9^o, 12^o and 14^o scans.

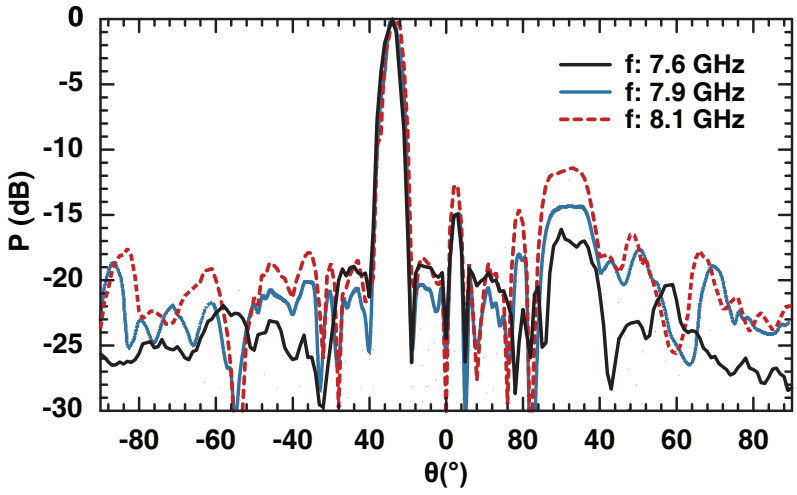

Figure 3.16: Normalized measured radiation patterns versus θ at 7.6 GHz, 7.9 GHz and 8.1 GHz for 14^o scan.

2 or 3-element arrays with the same L_{tot}.

3.5 2-D Random Arrays

It is possible to expand a 1-D random array design into a 2D random array design that can scan in both elevation and azimuth planes. The 1-D array is composed of PS primary arrays each centered at points D_i^n on the x axis and fed with a current C_i^n (Section II). For a given 1-D random array with K_{tot} antennas grouped into an optimized sequence of PS primary arrays, a 2-D array with $K_{tot} \times K_{tot}$ antennas is created. First, both the x-axis and the y-axis are sampled at points which corresponds to the center of the primary array groups of the 1-D arrays (i.e., $x_n^i = D_i^n$, $y_m^j = D_j^m$). Then by intersecting the parallel lines passing through these points, a 2-D grid composed of PS^2 points is defined on the XY plane. Fig. 3.17 presents a 2-D grid created using a 1-D random array with $K_{tot} = 30$, $PS = 12$, $K_2 = 6$, $K_3 = 6$, and with the best scanning performance (i.e., 3-2-2-3-2-2-2-2-3-3-3-3). Each point $(x, y) = (D_i^n, D_j^m)$ on this 2-D grid is the center of a $n \times m$ primary-array group which is fed by the current $C_{i,j}^{n,m}$. Therefore, if a 1-D random array has n different types of primary arrays, a 2-D random array synthesized using the 1-D array will have n^2 different types of primary arrays. The feed current, $C_{i,j}^{n,m}$, is calculated as

$$\left|C_{i,j}^{n,m}\right| = p_{xy}\left(t+(1-t)\,cos\left(\frac{\pi D_i^n}{L_{tot}}\right)\right)\left(t+(1-t)\,cos\left(\frac{\pi D_j^m}{L_{tot}}\right)\right) \tag{3.17}$$

$$\angle C_{i,j}^{n,m} = -\frac{2\pi}{\lambda}D_i^n sin(\theta_s)cos(\phi_s) - \frac{2\pi}{\lambda}D_j^m sin(\theta_s)sin(\phi_s) \tag{3.18}$$

where θ_s and ϕ_s are the scan angles. The factor p_{xy} in (3.17) is $\sqrt{nm}$ for equal power excitation and nm for uniform current excitation (see Section 3.2.2).

The total pattern is calculated as the multiplication of the horizontal array factor, $AF_x(\theta,\phi)$, vertical array factor, $AF_y(\theta,\phi)$, and the element pattern, $EP(\theta,\phi)$.

$$P(\theta,\phi) = AF_x(\theta,\phi) \times AF_y(\theta,\phi) \times EP(\theta,\phi) \tag{3.19}$$

$AF_x(\theta,\phi)$ is calculated as (7) and

$$AF_y(\theta,\phi) = \sum_n AF_n^a(\theta,\phi)AF_n^b(\theta,\phi) \tag{3.20}$$

where

$$AF_n^a(\theta,\phi) = \frac{sin\left(n\pi\frac{D_p}{\lambda}sin\theta sin\phi\right)}{nsin\left(\pi\frac{D_p}{\lambda}sin\theta sin\phi\right)} \tag{3.21}$$

$$AF_n^b(\theta,\phi) = \sum_{i=1}^{K_n} C_i^n e^{j\frac{2\pi D_i^n sin\theta sin\phi}{\lambda}}. \tag{3.22}$$

$AF_x(\theta,\phi)$ is uniform over the YZ-plane and $AF_y(\theta,\phi)$ is uniform over the XZ-plane. Hence, the sidelobes resulting from $AF_x(\theta,\phi)$ and $AF_y(\theta,\phi)$ are lower or equal than the sidelobes of both $AF_y(\theta,\phi)$ and $AF_y(\theta,\phi)$. Therefore, if a 1-D random array than can scan up to θ_{max} with $SLL < MSLL$ is used to synthesize a 2-D random array, the 2-D array can scan to any direction (θ_s,ϕ_s) with $SLL < MSLL$ where $(-\theta_{max} \le \theta_s \le \theta_{max})$ and $(0^o \le \theta_s < 180^o)$.

Fig. 3.18 presents the radiation patterns of the array depicted in Fig. 3.17 for $(\theta_s : 0^o, \phi_s : 0^o)$, $(\theta_s : 12^o, \phi_s : 0^o)$, $(\theta_s : 12^o, \phi_s : 90^o)$ and $(\theta_s : 12^o, \phi_s : 45^o)$ scans. The SLL of

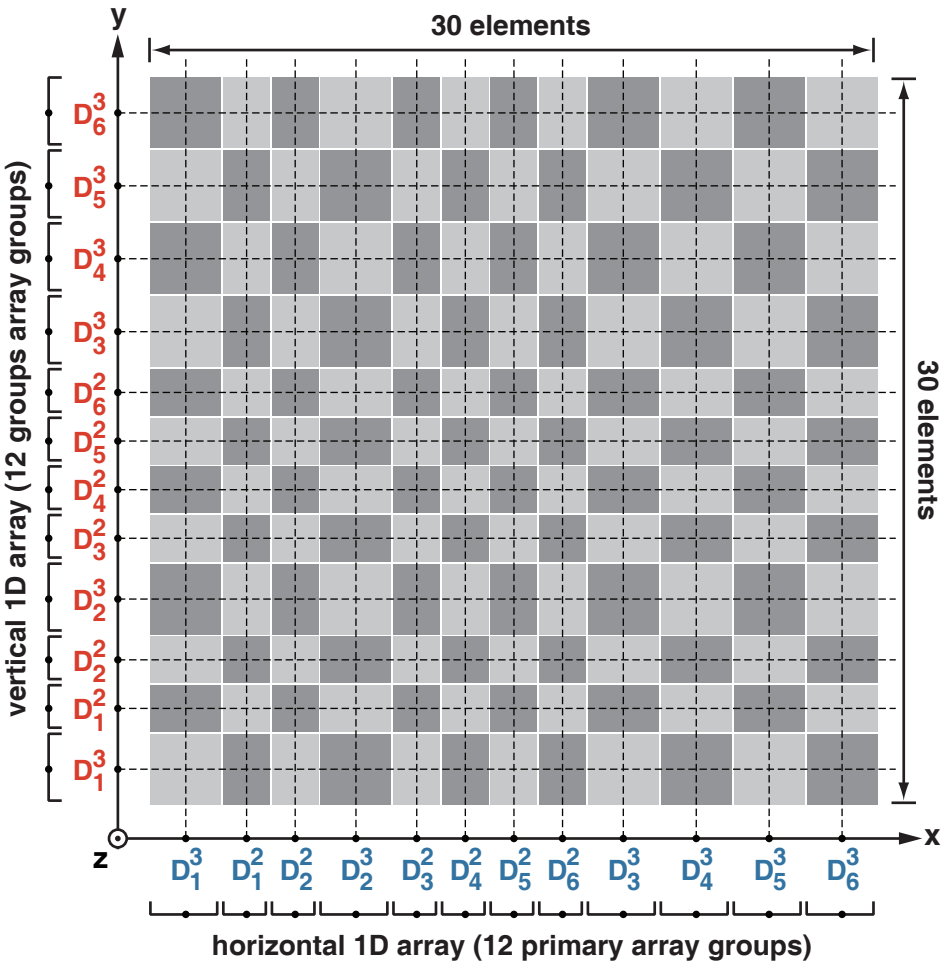

Figure 3.17: Grouping of a 30×30 2-D random array using 144 phase shifters.

the $(\theta_s : 12^o, \phi_s : 90^o)$ scan is 0.5 dB higher than the SLL of $(\theta_s : 12^o, \phi_s : 0^o)$ scan, since the element pattern $EP(\theta, \phi)$ is not symmetrical. The array has 144 phase shifters and 900 antennas, and on average, one phase shifter feeds 6.25 antennas. Compared to a uniformly-grouped array of 900 antennas with the same performance, the number of phase shifters are reduced by 45%. If more types of primary-array groups are used when designing the 1-D arrays such as 2,3 & 4 as in Fig. 3.7, the number of phase shifters can be reduced by up to %60 for the expanded 2-D random array designs.

The 2-D random array synthesis method described in this chapter uses a grid based on a 1-D array, hence it has only one level of flexibility. If the elements of the 2-D array are allowed to be grouped into primary arrays with arbitrary sizes in x and y directions and placed randomly on the XY-plane, it may be possible to obtain better results. This is the goal of a future work.

3.6 Conclusion

In this chapter, a new phased array feeding network that can scan a limited region in space with low sidelobe levels was presented. In this approach, the individual antennas are grouped into random sequences of non-uniform sub-arrays and a single phase shifter is used to feed each sub-array. The problem is reduced to a low number of variables and a simple search algorithm that searches all possible cases quickly finds the optimal design.

The performance of the random feeding scheme was compared to the conventional uniform sub-arraying over multiple cases. It is shown that the number of phase shifters can be reduced up to 40% as compared to uniformly grouped arrays.

A method for synthesizing 2-D random arrays with 1-D random array designs was also presented and can reduce the number of phase shifters by up to 60% compared to uniformly grouped 2-D arrays.

3.7 Acknowledgement

This work was supported by Toyota Research Institute of North America, Ann Arbor, Michigan.

Chapter 3 is mostly a reprint of the material as it is submitted for publishing to IEEE Antennas and Propagation, 2015. Bilgehan Avser; John Pierro; Gabriel M. Rebeiz. The dissertation author was the primary author of this material.

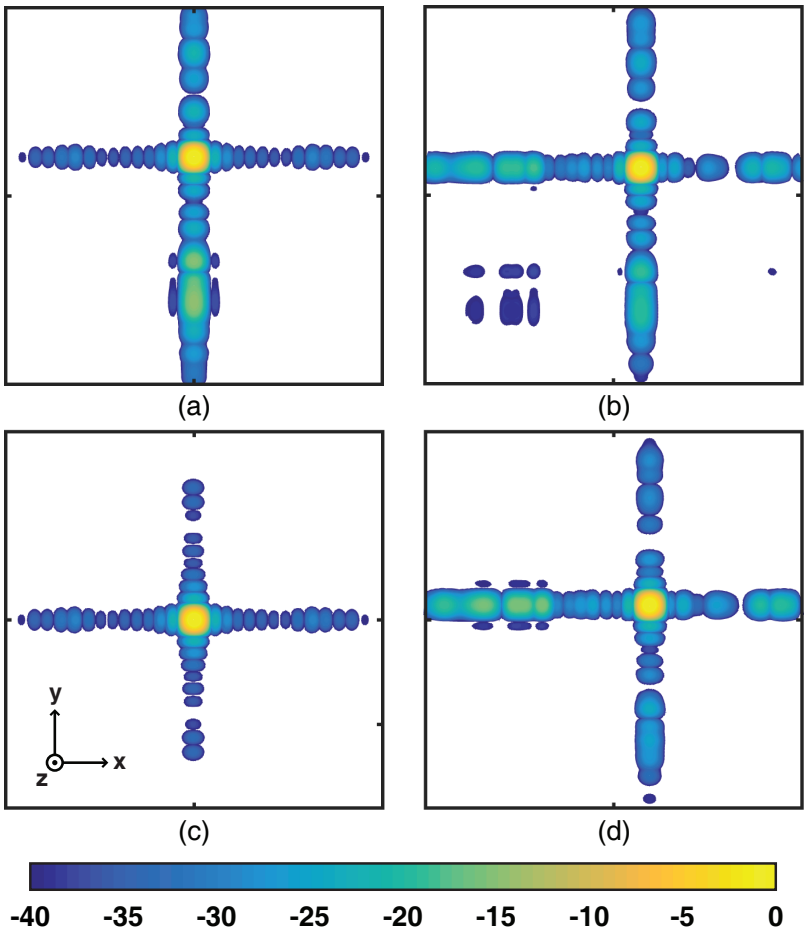

Figure 3.18: Normalized radiation patterns for scanning (a) $\theta = 12^o, \phi = 0^o$, (b) $\theta = 12^o, \phi = 45^o$, (c) $\theta = 0^o, \phi = 0^o$ and (d) $\theta = 12^o, \phi = 90^o$.

Chapter 4

Interwoven Feeding Networks with Aperture Sinc-Distribution

4.1 Introduction

Phased array systems with electronic beam scanning have been used for radar and communications systems since the 1970s [23] and with application areas such as satellite systems for high-data rate communications [27, 28]. These systems require narrow beams with low sidelobe levels that can scan in a wide field of view. In recent years, phased array systems have been in commercial applications such as automotive radars [29–31], landing systems [39, 40] and advanced robotic sensors. These systems usually require a narrower field of view and can tolerate higher sidelobe levels. However, due to the commercial nature of these applications, criteria such as low cost and low complexity are critical for wide adoption.

Uniform sub-arraying, the conventional way of reducing the number of phase shifters by dividing the phased array into uniform sub-arrays and feeding each sub-array with a single phase shifter, is relatively simple to implement and reduces the number of phase shifters up to a limited level with low sidelobes [41, 42]. However, if the number of phase shifters are further reduced (i.e., the sub-array sizes are large), grating lobes start to enter the visible space and this causes the side-lobe level to significantly increase. This problem can be solved by increasing the size of the sub-arrays (i.e, grouping more elements into the each sub-array) while keeping the center of sub-arrays at the same positions. However, increasing the sub-array sizes without moving the phase centers causes the sub-arrays to overlap and the planar implementation of such overlapping arrays poses multiple challenges [47].

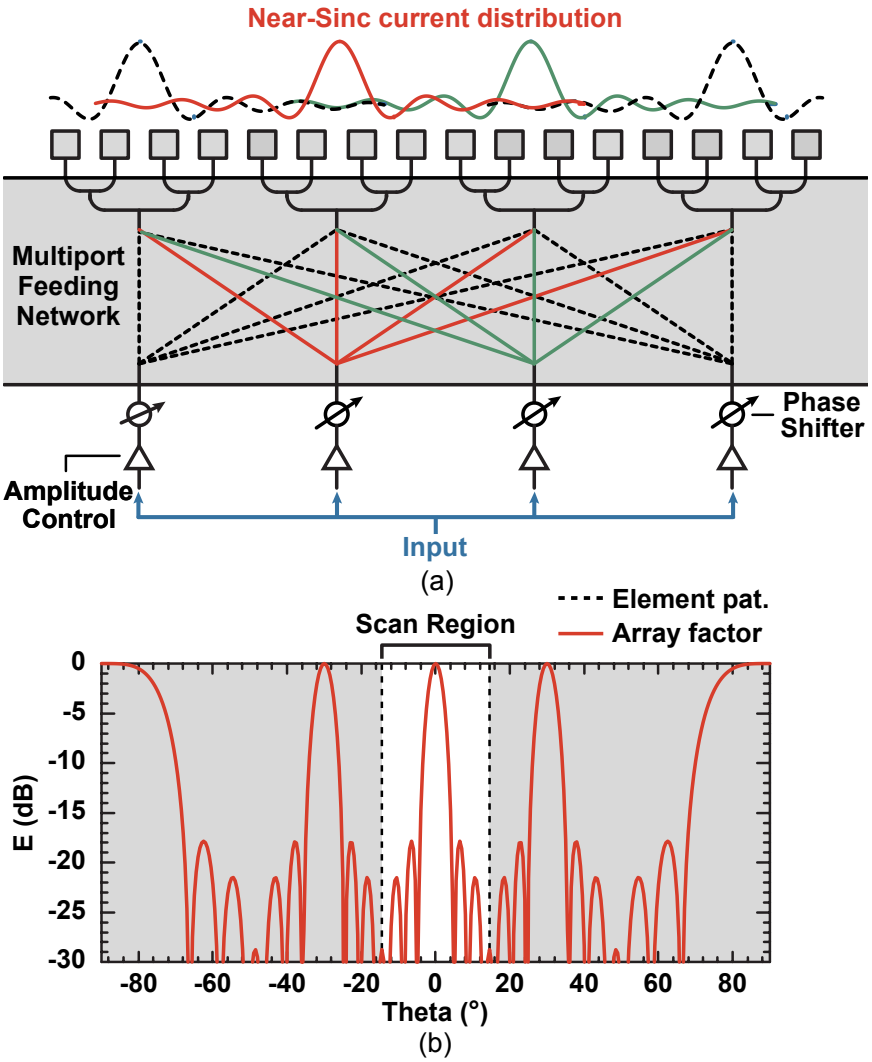

Figure 4.1: (a) Passive multi-port feeding network that creates a near-sinc current distribution over the whole array, and (b) resulting array factor and element patterns.

A common way of implementing overlapping arrays is using interleaved arrays [46]. In this configuration, the inter-element distance inside the sub-arrays is increased and the sub-arrays are placed with a small offset so that the individual antennas in the adjacent sub-array groups do not overlap. However, when low directivity elements are placed that closely to each other, the mutual coupling effects between the antennas lends to poor scan performance. Furthermore, the sub-array sizes still cannot exceed a certain limit, since there is not enough space to overlap more than two sub-arrays.

Another way of implementing overlapping arrays is using partial overlapping sub-arrays [41]. In this configuration, the overlapping antennas of adjacent sub-array groups are fed using power combiners from different overlapping sub-arrays. These networks work well for smaller sub-array sizes. However, their loss and complexity increases significantly when more than two sub-arrays start to overlap at one time (i.e., when an individual antenna is fed with more than two sub-array groups). Therefore, the benefit of using large sub-arrays is not fully realized.

A promising approach for implementing larger sub-arrays is using a multi-port interwoven feeding network, where each phase shifter feeds all of the array elements (Fig. 4.1). Such a network can be realized using hybrid-couplers, Wilkinson dividers and attenuators [48]. An ideal element pattern (near-uniform in the scan region and sharply decreasing outside) can be synthesized using the entire array aperture. This chapter presents the theory, design and planar implementation of such feeding networks for arbitrary scan regions. Two 28-element arrays are built at 7.9 GHz to demonstrate the interwoven feeding networks and with state-of-the-art results in terms of reduced number of phase shifters, scan angles and grating lobes.

4.2 Interwoven Feeding Networks

4.2.1 Theory

If an infinite array is fed using a multi-port feeding network such as in Fig. 4.1(a), each phase-shifter creates an identical current distribution over the array aperture centered at the phase shifter position. When multiple phase shifters are used to feed the array, the resulting current distribution is calculated by using superposition of the individual current distributions. Hence the array pattern is a multiplication between an element pattern, $EP(\theta, \phi)$, resulting from the individual current distribution and an array factor, $AF(\theta, \phi)$, resulting from a linear array with elements located at the phase shifter positions as:

$$P(\theta, \phi) = AF(\theta, \phi) \times EP(\theta, \phi). \tag{4.1}$$

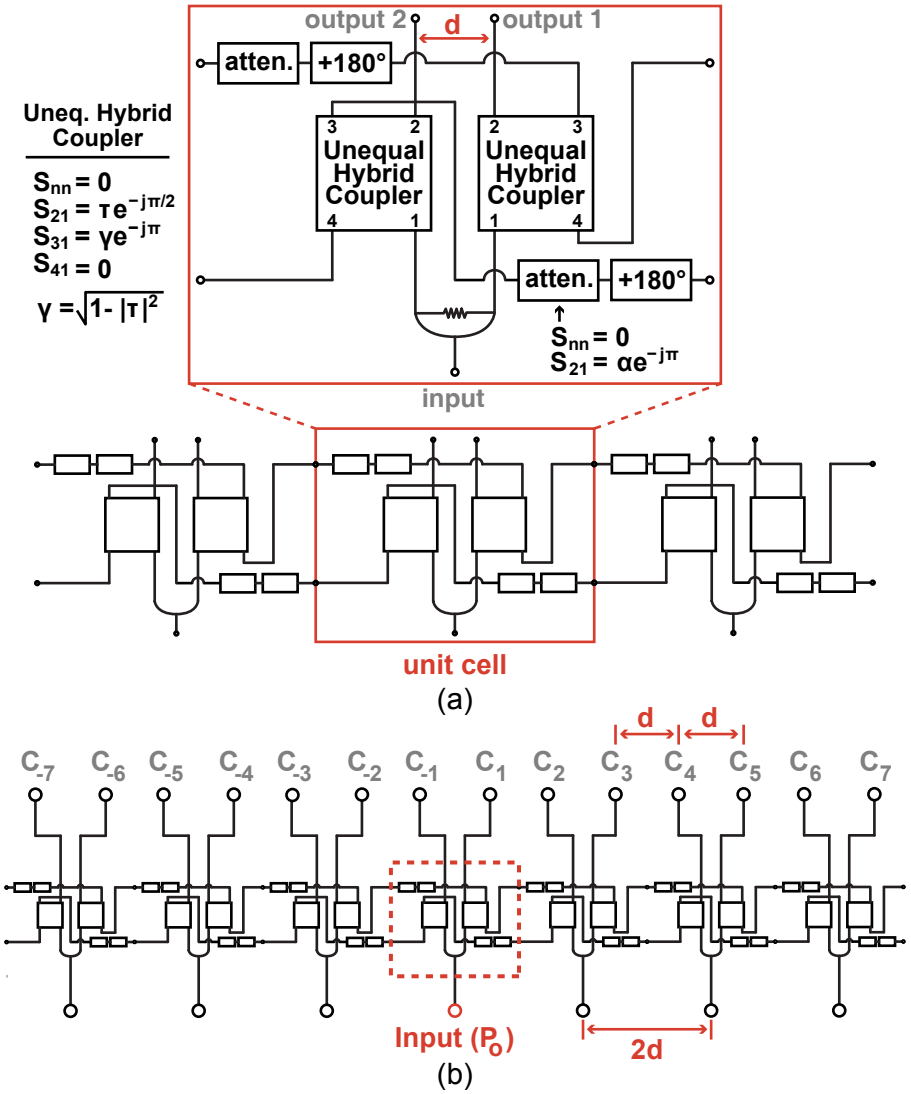

Figure 4.2: (a) Unit cell of a passive multi-port feeding network and (b) naming of the network outputs for an input port in the middle of the array.

The ideal element pattern that cancels the grating lobes outside of the scan-region without suppressing the main beam inside the scan-region is a box-car function which is equal to 1 up to the edge of the scan-region and is 0 outside. To create such an element pattern, a continuous Sinc-function current distribution is required over an infinite aperture. However, a finite and discrete approximation to the Sinc distribution also results in a sharp element pattern that cancels the grating lobes without suppressing the main beam in the scan region.

Fig. 4.2 presents the passive feed network used to create a near-Sinc distribution over the array elements. Each unit cell in the feed network has one input port and two output ports with a spacing d, and when the ports are uniformly spaced, the distance between adjacent input ports is $2d$. Note that for $d = 0.5\lambda_\circ$ and $d = 0.75\lambda_\circ$, each output port is connected to a single antenna. However, for $d = \lambda_\circ$ and larger, two antenna elements with a separation of $d/2$ are connected to each output port.

If a single input is excited and all other ports are terminated with matched loads, a symmetrical current distribution around the input port is created at the output ports. For the feed network in Fig. 4.2(b), the current distribution is

$$C_k = \begin{cases} \tau & ;\ |k| = 1 \\ 0 & ;\ |k| \neq 1 \text{ and } |k| \text{ is odd} \\ \gamma^2\alpha(-\alpha\tau)^{\frac{|k|-2}{2}} & ;\ |k| \text{ is even} \end{cases} \tag{4.2}$$

where τ, γ and α are defined in Fig. 4.2(a). C_3 and C_5 are zero independent of the design variables and C_1 and C_2 always have positive values with

$$\frac{C_1}{C_2} = \frac{\tau}{(1-\tau^2)\alpha}. \tag{4.3}$$

Using this feeding network over many elements, C_1 and C_2 approximate the Sinc-function main lobe, while C_3 and C_5 lie on the Sinc-function first and second nulls (Fig. 4.3(a)). C_4 becomes a negative value and lies on the first negative peak of the Sinc-function. Fig. 4.3(a) presents the entire current distribution over an infinite array for a single input with $\alpha = 0.78$ and $\tau = 0.79$. It is shown that the first five current values, C_1, C_2, C_3, C_4 and C_5, approximate the Sinc-function very closely. The rest of the points (i.e, C_k where $k \geq 6$) lie roughly on the Sinc-function, but they do not have a large effect on the element pattern since their amplitudes are very small.

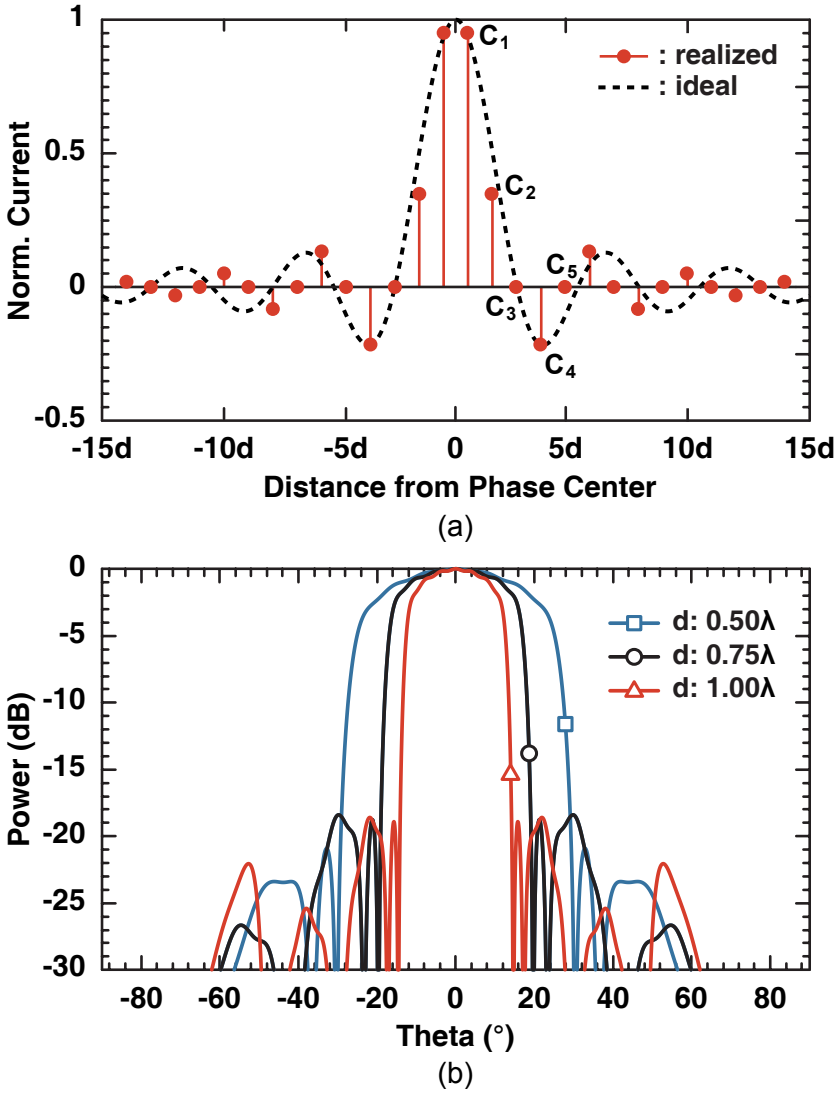

Figure 4.3: (a) Current distribution over array elements and (b) element pattern of the interwoven feeding network with $\alpha = 0.69$ and $t = 0.77$ when a single input is excitedfor different values of d.

The distance between the output ports, d, is chosen to adjust the width of the scan-region. Fig. 4.3(b) presents the element patterns resulting from the near-Sinc current distribution for different d values. When $d = \lambda_\circ$, a Wilkinson divider is used, and each output port feeds two antennas with a seperation of $\lambda_\circ/2$. This method introduces an extra array factor ($AF^*(\theta) = cos(\pi d sin\theta/\lambda_\circ)$) due to the in-phase antenna elements and significantly decreases the grating lobes at $> 50^o$. The $d = \lambda_\circ$ curve in Fig. 4.3 (b) is constructed using this additional array factor.

For a scan angle, θ_s, the phase difference between adjacent interwoven network inputs, β, is

$$\beta = -\frac{2\pi}{\lambda_\circ}(2d)sin(\theta_s) \tag{4.4}$$

For an infinite array, if same current amplitude ($C_{in} = 1$) is applied to each input, all outputs will have the same current magnitude, $C_{tot}(\theta_s)$, where

$$C_{tot}(\theta_s) = \frac{1}{\sqrt{2}}\left|C_1 + \sum_{k=1}^{\infty}\left(C_{2k}e^{jk\beta} + C_{2k+1}e^{-jk\beta}\right)\right|. \tag{4.5}$$

Since C_{2k+1} values are all zero, the second term inside the summation is zero. If the C_k values in (4.2) are expanded in (4.5), one gets

$$C_{tot}(\theta_s) = \frac{1}{\sqrt{2}}\left|\tau + \gamma^2\alpha e^{j\beta}\sum_{k=0}^{\infty}(-\alpha\tau e^{j\beta})^k\right|. \tag{4.6}$$

The geometric series converges to $1/(1 + \alpha\tau e^{j\beta})$ since $|-\alpha\tau e^{j\beta}| < 1$ and

$$C_{tot}(\theta_s) = \frac{1}{\sqrt{2}}\left|\tau + \gamma^2\alpha e^{j\beta}\frac{1}{1+\alpha\tau e^{j\beta}}\right|. \tag{4.7}$$

Since the number of outputs is twice the number of inputs, $P_{out}/P_{in} = 2C_{tot}^2$. It is known that $P_{out} < P_{in}$ due to the attenuators used in the feeding network. The loss, calculated as P_{out}/P_{in}, is

$$L(\theta_s) = \left|\tau + \gamma^2\alpha e^{j\beta}\frac{1}{1+\alpha\tau e^{j\beta}}\right|^2. \tag{4.8}$$

At broadside ($\theta_s = 0°$), $L(\theta_s)$ is

$$L(0) = \left| \frac{\alpha + \tau}{1 + \alpha\tau} \right|^2 . \tag{4.9}$$

For the ideal case in Fig. 4.3(a) with zero (or very low) transmission-line loss, $\tau = 0.79$, $\alpha = 0.78$ and $L(0) = 0.25$ dB. The loss increases to $L(22^\circ) = 1.5$ dB and $L(10^\circ) = 1.5$ dB for $d = 0.5\lambda_\circ$ and $d = \lambda_\circ$, respectively, at the edge of the scan region. However, if the system is implemented using microstrip lines, the total line loss becomes part of the attenuation coefficient, α, and in order to compensate for the higher α, a lower τ should be used. This causes the overall loss to increase as shown in Sections 4.4 and 4.5.

When designing finite interwoven arrays, the unit cells at the ends of the array are terminated with $50\ \Omega$ loads. In this case, the current distributions created by the different input ports are not exactly identical. However, since the Sinc function decreases significantly after a few unit cells, it is safe to assume that most of the power is radiated by the adjacent unit cells. Therefore, the element pattern is also close the infinite array cases even in finite arrays.

Amplitude taper is applied by adjusting the power into each input of the feeding network. The power levels are determined by defining an ideal taper function over the whole array and calculating its value at points where the input ports are located. This creates a staircase approximation to the ideal taper function but still works well and results in reduced sidelobe levels next to the main beam.

4.2.2 Bandwidth of Interwoven Arrays

Fig. 4.4(a) and (b) present the element pattern versus frequency for 28 element ideal interwoven arrays fed with 14 and 7 phase shifters, respectively. The design parameters are $\tau = 0.79$, $\alpha = 0.78$ and $d = 0.5\lambda_\circ$ for the 1:2 array and $\tau = 0.79$, $\alpha = 0.72$ and $d = \lambda_\circ$ for the 1:4 array. The element patterns hold their boxcar-like shape for a fractional bandwidth of $\pm 10\%$. At wider bandwidths, the sidelobe levels increase and the element factor loses its box-car characteristics.

In ideal simulations or if the array is constructed using non-planar coaxial lines, the unit cells can be connected using very short transmission lines. However, this is not possible in a microstrip implementation since the distance between the unit cells is $> \lambda_g$. To preserve the 180° phase progression between the unit cells, multiple 360° transmission-line section are used. Fig. 4.5(a) and (b) present the element pattern versus frequency for 28 element ideal interwoven arrays, with additional 720° transmission-line sections between the unit cells, fed with 14 and 7

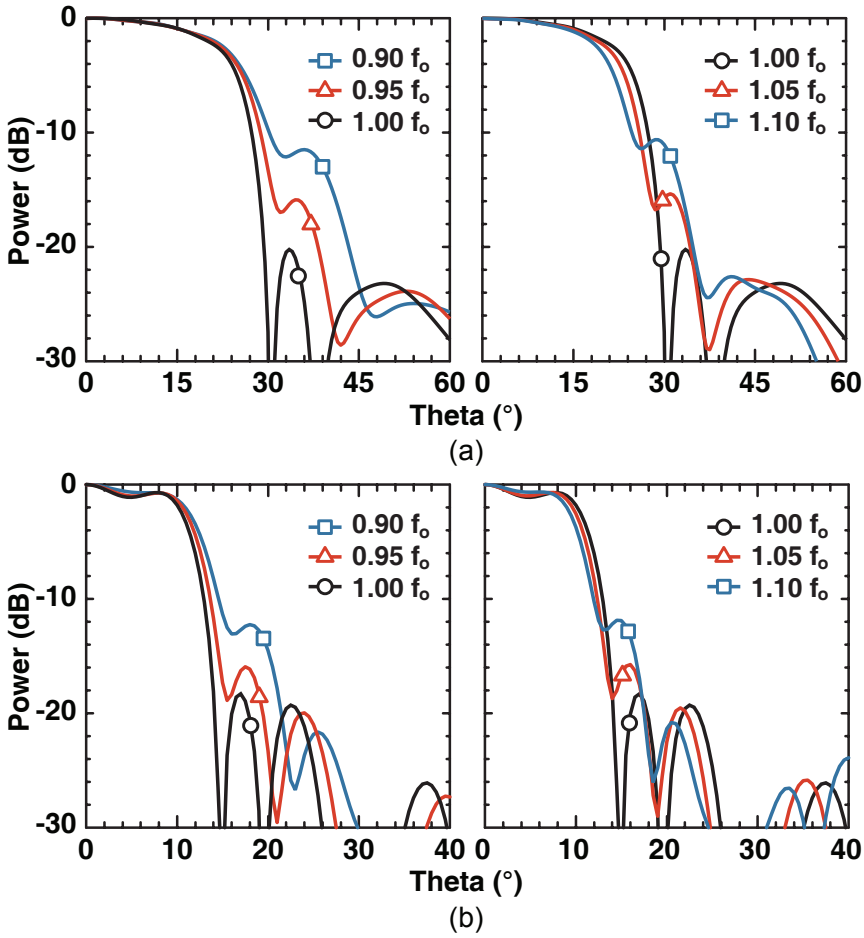

Figure 4.4: Simulated element pattern versus frequency for (a) ideal 1:2 interwoven array ($\tau = 0.79$, $\alpha = 0.72$, $d = 0.5\lambda_\circ$) and (b) ideal 1:4 interwoven array ($\tau = 0.79$, $\alpha = 0.78$, $d = \lambda_\circ$) with 0° transmission-line sections between the unit cells.

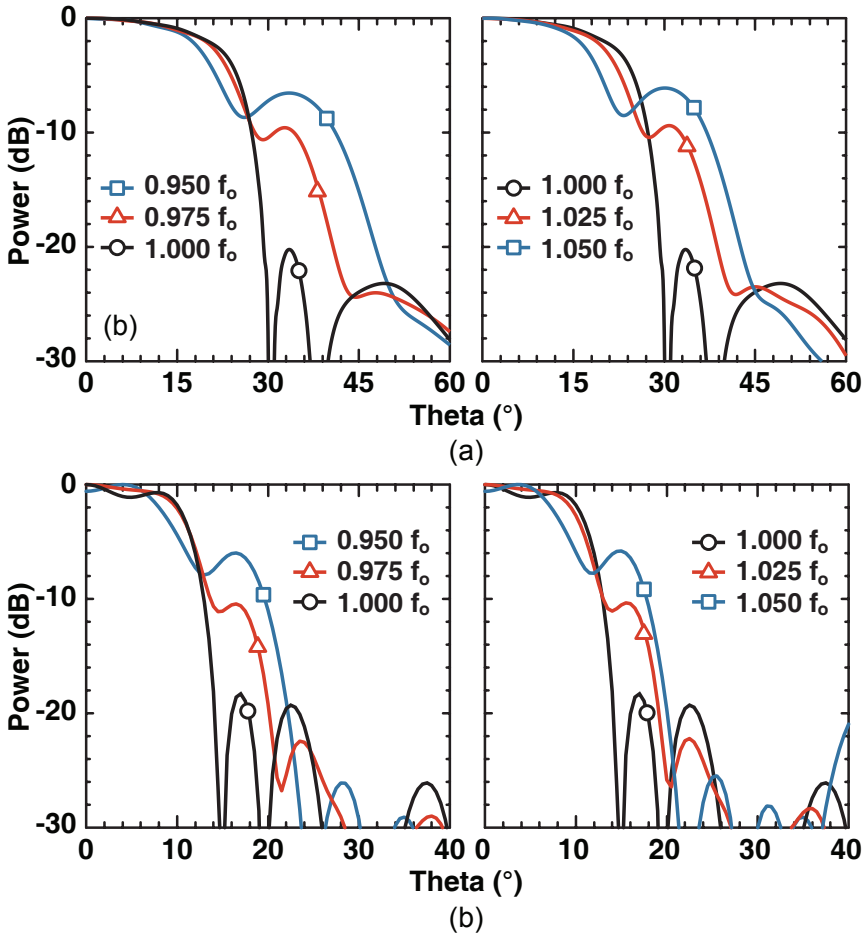

Figure 4.5: Simulated element pattern versus frequency for (a) ideal 1:2 interwoven array ($\tau = 0.79$, $\alpha = 0.72$, $d = 0.5\lambda_\circ$) and (b) ideal 1:4 interwoven array ($\tau = 0.79$, $\alpha = 0.78$, $d = \lambda_\circ$) with 720° transmission-line sections between the unit cells.

phase shifters, respectively. The same design parameters in Fig. 4.4 are used. It is seen that the additional line sections limit the bandwidth to $\pm 2.5\%$.

4.3 Planar Implementation of a 1-to-2 Interwoven Feeding Network

A 28-element array with 14 phase shifters and a spacing of $d = 0.5\lambda_\circ$ is designed at 7.9 GHz using a 1:2 (i.e., one phase shifter per every two antennas) interwoven feeding network, to demonstrate the concept. The design frequency is selected as 7.9 GHz to present a 1:10 scale to the 79 GHz band which is heavily used for automotive radar applications [29–31].

4.3.1 Design

The network is built on a 0.34 mm thick RO4350 substrate ($\epsilon_r = 3.66$) where the loss of a $50\ \Omega$ transmission line is 0.17 dB/cm at 8 GHz. When the unit cells are placed $2d = \lambda_\circ$ apart, the loss for the shortest possible line connecting adjacent unit cells is simulated as 2 dB. This value corresponds to α in Section 4.2. To create a Sinc-like current distribution, $\tau = 0.75$ ($|S_{21}| = 2.5$ dB), $\gamma = 0.59$ ($|S_{31}| = 4.9$ dB) are chosen in the quadrature coupler. Note that the lumped element attenuators in Fig. 4.2 are not present since the attenuation, α, is in the transmission lines.

The geometry of the feeding network board is presented in Fig. 4.6 and the simulated 1:2 array loss versus scan angle is presented in Fig. 4.7. This loss is calculated in Agilent ADS and takes into account the microstrip the feeding network loss with 14 input ports [24]. The loss increases as the beam is scanned, and agrees with the predictions of (4.8) except for higher values due to the microstrip line implementation.

Since the network is implemented using a two-layer microstrip configuration, the transmission lines need to cross each other at the intersection points (Fig. 4.8). The design is matched at all ports with an isolation > 23 dB over a wide bandwidth (7-9 GHz).

Fig. 4.9(a) presents the geometry of an individual array element consisting of 4 series-fed antennas aligned in the vertical (elevation) plane. The antennas are built on a stack of 1.73 mm thick RO4003 ($\epsilon_r = 3.55$) and 0.34 mm thick RO4350 ($\epsilon_r = 3.66$) with a ground plane in-between. Fig. The 4-element antenna impedance and measured normalized gain at broadside re presented in 4.9(b). The bandwidth of the vertical array element is limited by the impedance match and by the beam squint versus frequency due to the 2π transmission-line sections.

Fig. 4.10 illustrates the general structure of the test array. The input power is divided

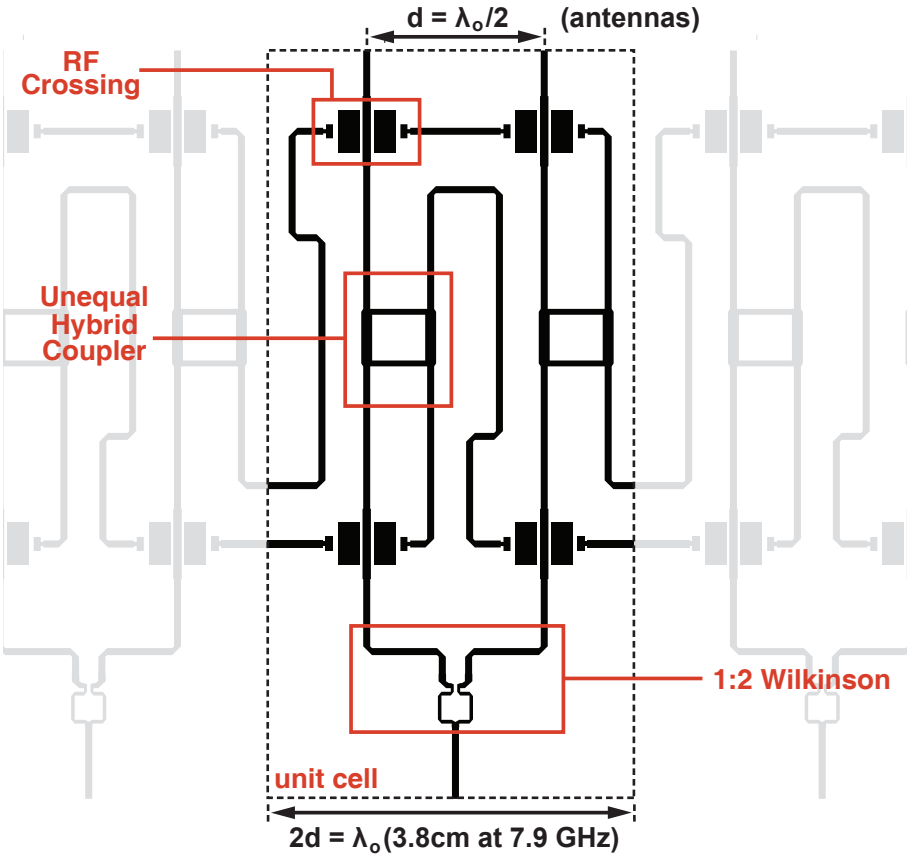

Figure 4.6: The geometry of the 1:2 feeding network.

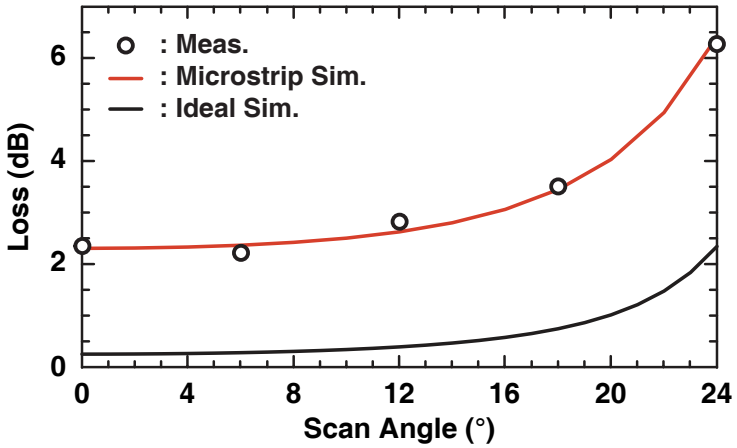

Figure 4.7: Simulated and measured loss of the 1:2 feeding network versus scan angle.

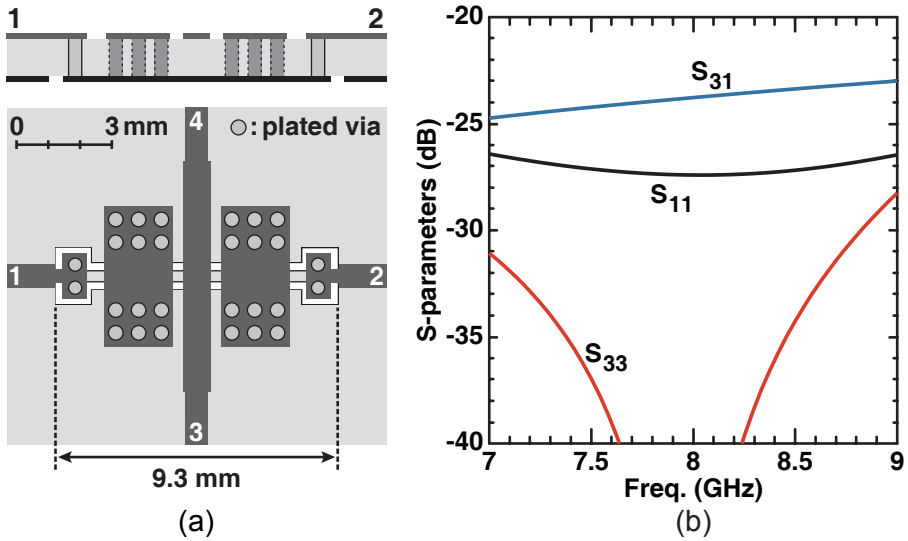

Figure 4.8: (a) Geometry and (b) simulated S-parameters of the two-layer RF-crossing structure.

by a 1-to-14 power divider board consisting of a cascaded Wilkinson networks. The board outputs have equal magnitude and equal phase. A 6 dB edge taper is then applied using 14 coaxial attenuators. The outputs of the attenuators are connected to a 14-to-14 phase-shifter board. The phase shifts are realized using different lengths of transmission lines, and are therefore true-time delay units. There are five different phase shifter boards that result in a fixed θ_s of 0°, 6°, 12°, 18° and 24°. Each of the phase shifter boards are symmetrical and hence, they are flipped and connected to the array to result in $\theta_s = -6^\circ$, -12°, -18° and -24° scan angles. The outputs of the phase shifter board are connected to the interwoven feeding board as in Fig. 4.10. Finally the output of the interwoven feeding board is connected to the 4-element vertical antennas. Fig. 4.10 presents the fabricated array.

4.3.2 Experimental Results and Discussions

Fig. 4.12 presents the simulated and measured normalized patterns of the array at 7.8 GHz when a single port is excited in the middle of the interwoven network. The measured pattern agrees well with the simulated element pattern. The pattern is near-uniform up to $\pm 20^\circ$ (-1.5 dB) and rapidly decrease outside. As discussed in Section II, these patterns are ideal for canceling the grating lobes outside the scan region.

Fig. 4.13-4.17 present the measured patterns and the simulated grating lobes without the interwoven feeding networks at $\theta_s = 0^\circ$ and 6°, 12°, 18°, 24°. The element factor of the interwoven network successfully cancels the grating lobes outside the scan-region. The fabri-

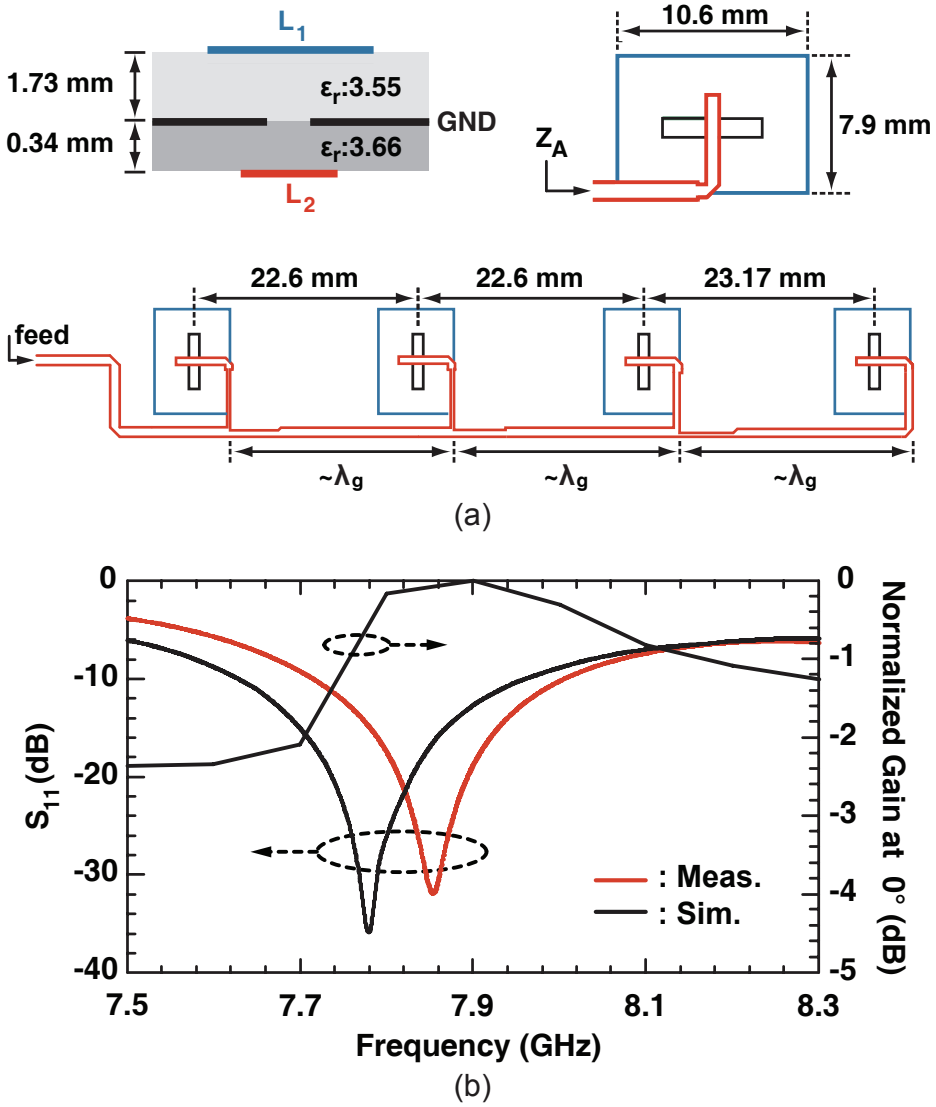

Figure 4.9: (a) Board stack-up, single antenna and series element geometry and (b) impedance match and normalized gain for the 4-element antenna.

cated array can scan $\pm 24^{\circ}$ while keeping the grating lobes under -15 dB. However after $\pm 22^{\circ}$, the element pattern start to suppress the main beam and this causes the peak power to drop approximately 3 dB compared to the 0° scan. Fig. 4.19 present the normalized measured peak power versus frequency. The 1:2 array has a 2 dB bandwidth of 300 MHz (7.7-8.0 GHz) which is mainly limited by the 4-element vertical antenna (see Fig. 4.9).

Fig. 4.20(a) presents the measured element pattern for the 28-element 1:2 interwoven array at different frequencies. As discussed in Section II.B, the extra $2n\pi$ transmission-line sections degrade the element pattern versus frequency. However, up to the $\pm 18^{\circ}$ scan, the element pattern still successfully suppresses the grating lobes (Fig. 4.20(a)). Measurements at $\pm 24^{\circ}$ scan angle shows severe degradation at 7.7 and 7.9 GHz with grating lobes at the -10 dB level. Therefore, this implementation with the extra $2n\pi$ transmission-lines can scan to $\pm 18^{\circ}$ with 1 dB loss while keeping the grating lobes $<$ -10 dB over the 7.7-7.9 GHz bandwidth.

Table 4.1 presents the loss breakdown of the 1:2 interwoven array at 7.8 GHz. The total measured loss is $\sim$ 14.0 dB at the broadside scan and is $\sim$ 14.8 dB at other scan angles, since the phase shifters are not used at the broadside scan. The measured antenna gain at broadside, referenced to the input power, is 12.4 dB at 7.8 GHz. If the measured loss of 14.0 dB is added to this value, the measured directivity is found to be 26.4 dB. This agrees well with the simulated directivity of 26.5 dB.

4.4 Planar Implementation of a 1-to-4 Interwoven Feeding Network

Using a 1:4 interwoven feeding network (i.e., one phase shifter per every four antennas), a 28-element array with 7 phase shifters and a spacing of $d = \lambda_{\circ}$ (antenna spacing of $0.5\lambda_{\circ}$) is designed at 7.9 GHz.

4.4.1 Design

The network is built on the same 0.34 mm thick RO4350 substrate ($\epsilon_r = 3.66$) as Section 4.3. When the unit cells are placed $2d = 2\lambda_{\circ}$ apart, the loss for the shortest possible line connecting adjacent unit cells is simulated as 2.5 dB. This value corresponds to α in Section 4.2 and presents enough attenuation so that lumped-element attenuators are not needed. The quadrature couplers are chosen as $\tau = 0.72$ ($|S_{21}| = 2.9$ dB), $\gamma = 0.68$ ($|S_{31}| = 3.4$ dB) to create a Sinc-like current distribution.

Fig. 4.21 presents the geometry of the feeding network board and Fig. 4.22 presents

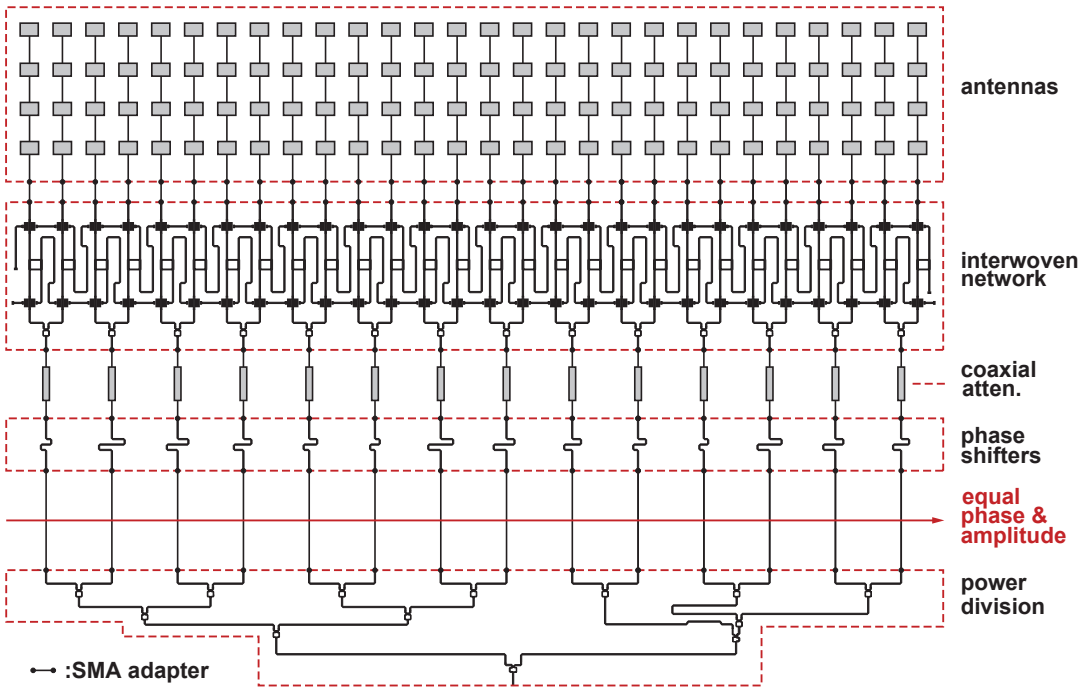

Figure 4.10: Schematic representation of the 1:2 interwoven array at 7.8 GHz

Table 4.1: Loss of the Fabricated 1:2 Interwoven Array at 7.8 GHz

Part	Loss (dB)
Power divider board	5.6
Attenuators (incl. 6 dB taper)	4.1
Phase shifters	0.8
Interwoven feeding network	2.3
4-Element vertical patch array	2.0
Total loss without phase shifters (0° scan)	14.0
Total loss with phase shifters	14.8

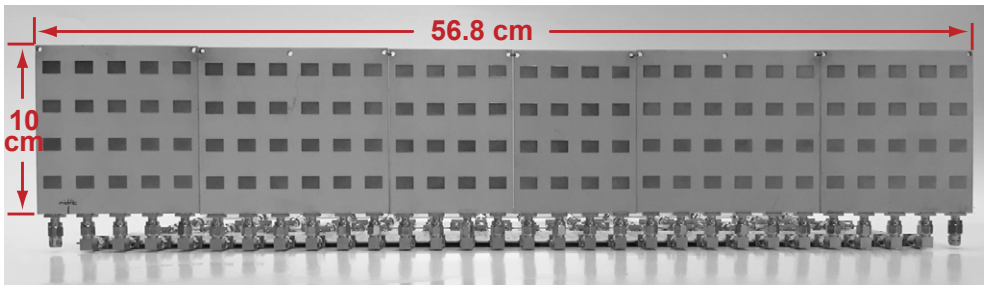

(a)

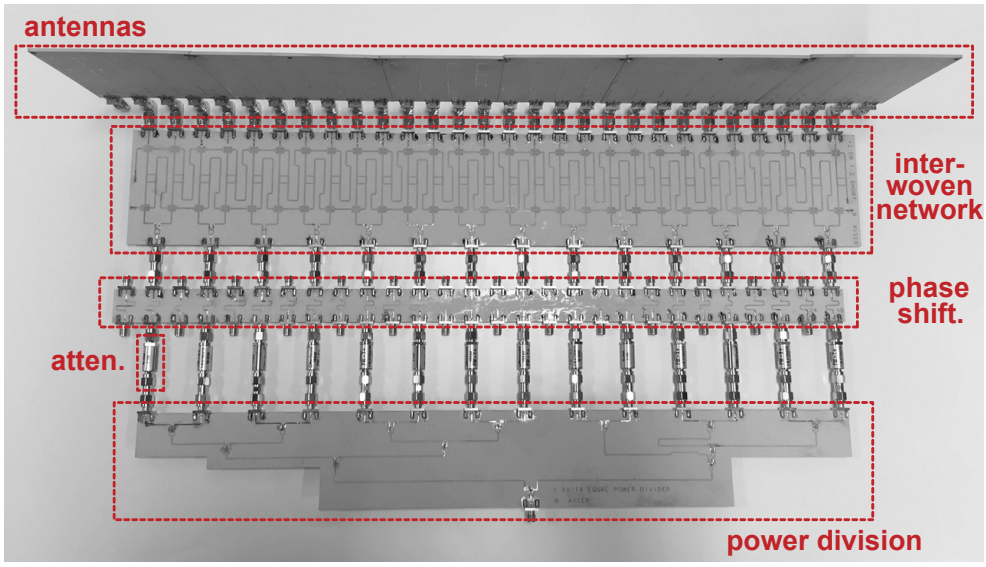

(b)

Figure 4.11: Fabricated 1:2 interwoven array with 28 elements: a) front view, b) back view.

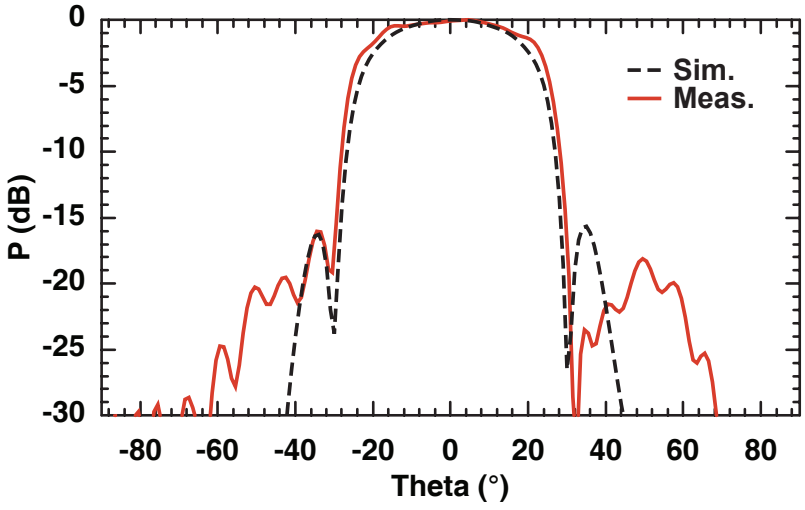

Figure 4.12: Simulated and measured normalized element patterns of the 1:2 array.

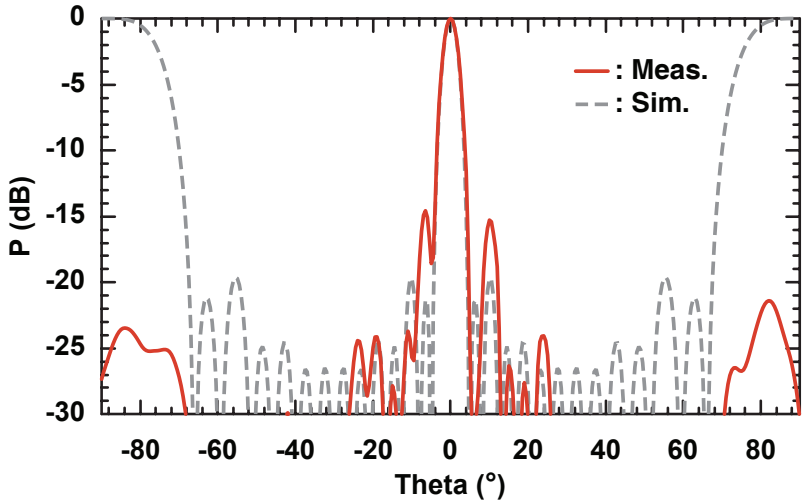

Figure 4.13: Measured radiation pattern of the 1:2 array and the simulated grating lobes without the interwoven feeding networks at 0° scan.

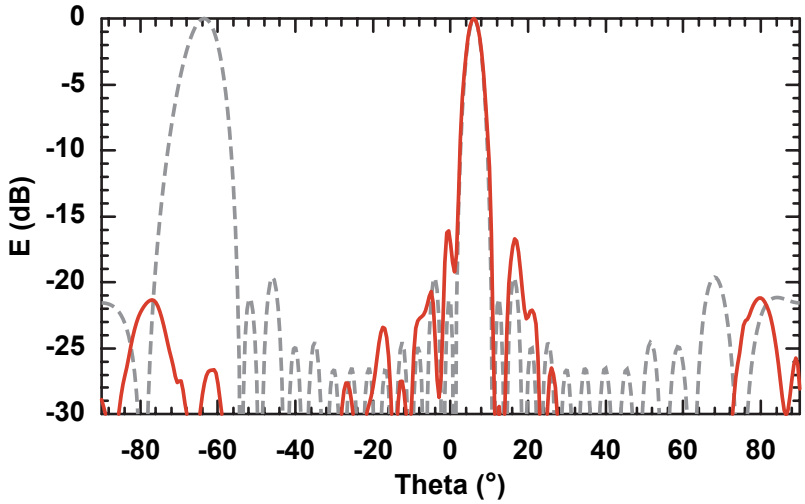

Figure 4.14: Measured radiation pattern of the 1:2 array and the simulated grating lobes without the interwoven feeding networks at 6° scan.

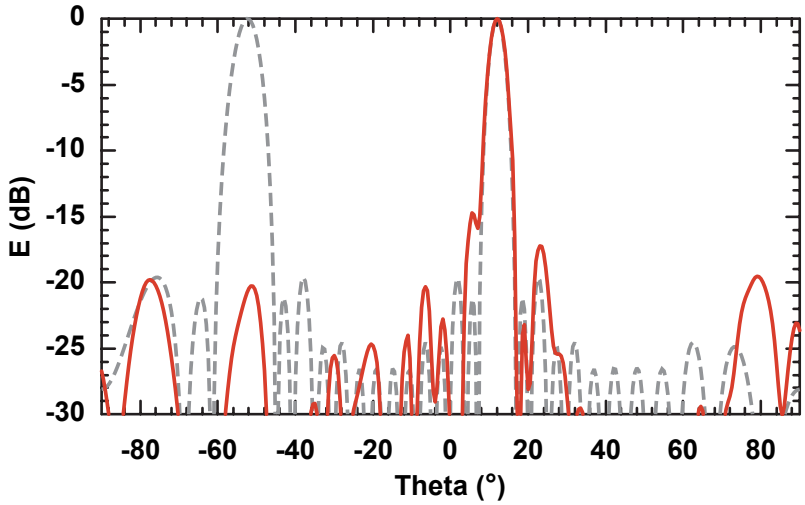

Figure 4.15: Measured radiation pattern of the 1:2 array and the simulated grating lobes without the interwoven feeding networks at 12° scan.

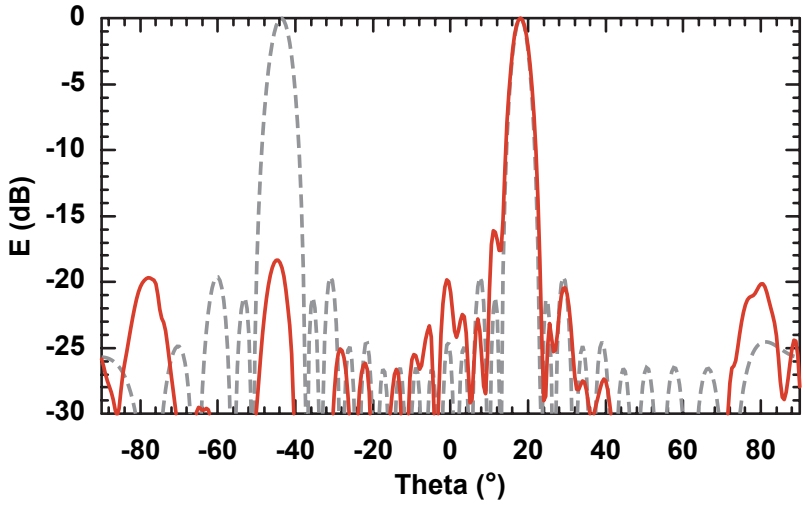

Figure 4.16: Measured radiation pattern of the 1:2 array and the simulated grating lobes without the interwoven feeding networks at 18° scan.

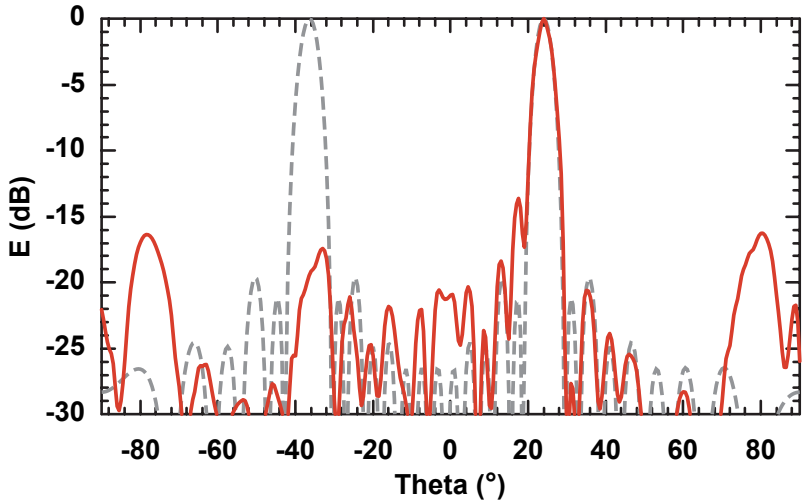

Figure 4.17: Measured radiation pattern of the 1:2 array and the simulated grating lobes without the interwoven feeding networks at 24° scan.

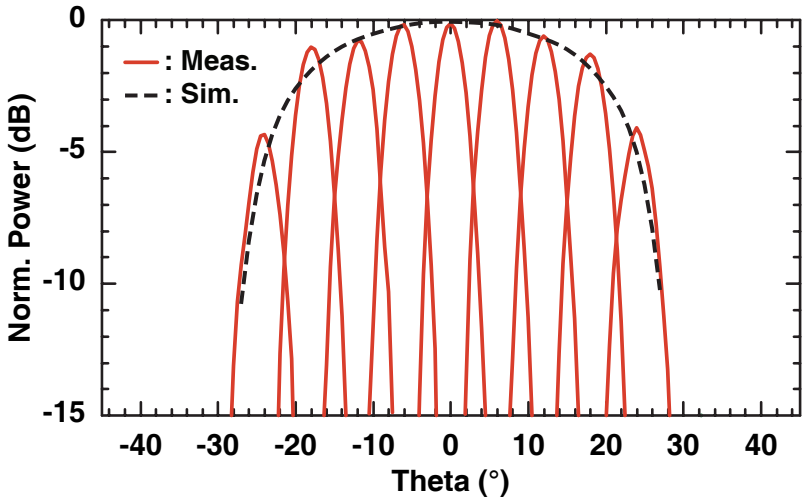

Figure 4.18: Measured array pattern and simulated gain drop of the 1:2 array at 7.8 GHz.

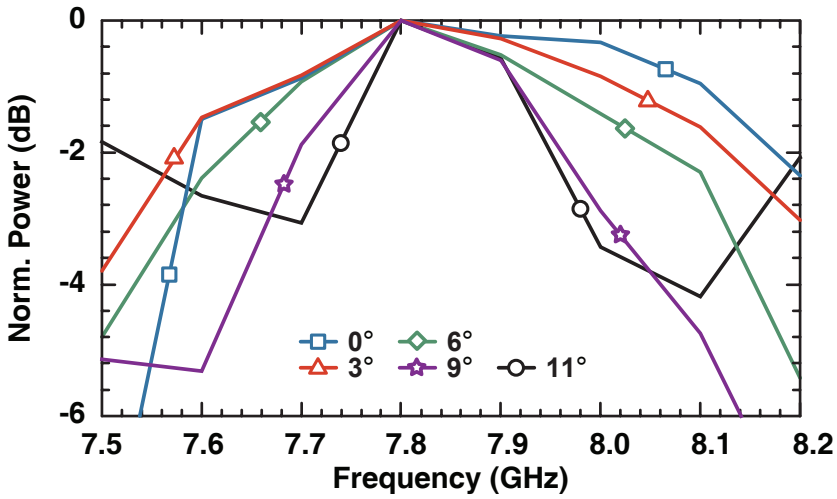

Figure 4.19: Measured normalized peak power of the 1:2 array versus frequency and different scan angles.

the simulated 1:2 array loss versus scan angle. This loss is calculated in Agilent ADS and takes into account the microstrip the feeding network loss with 7 input ports. Similar to the 1:2 array, the loss increases as the beam is scanned away from broadside, and agrees with the predictions of (4.8) except for higher values.

Fig. 4.23 illustrates the general structure of the 1:4 test array. The input power is divided by a 1-to-7 power divider board consisting of a cascaded Wilkinson networks where all outputs have equal magnitude and equal phase. A 6 dB edge taper is then applied using 7 coaxial attenuators. The outputs of the attenuators are connected to a 7-to-7 true-time delay phase-shifter board. There are five different phase shifter boards that result in a fixed θ_s of 0°, $\pm 3^\circ$, $\pm 6^\circ$, $\pm 9^\circ$ and $\pm 11^\circ$. The outputs of the phase shifter board are connected to the interwoven feeding board as in Fig. 4.23. Finally, the outputs of the interwoven feeding board is connected to the 4-element vertical antennas. The fabricated array is presented in Fig. 4.24.

4.4.2 Experimental Results and Discussion

The simulated and measured normalized patterns of the array when a single port is excited in the middle of the interwoven network is presented in Fig. 4.25. The pattern is near-uniform up to the $\pm 10^\circ$ (-2.4 dB) and rapidly decrease outside of this region.

The measured patterns and the simulated grating lobes without the interwoven feeding networks at $\theta_s = 0^\circ$ and 3°, 6°, 9°, 11° are presented in Fig. 4.26-4.30. Since the phase shifters are $2\lambda_\circ$ apart, even at the broadside scan there exists two grating lobes in the visible space (at 30°

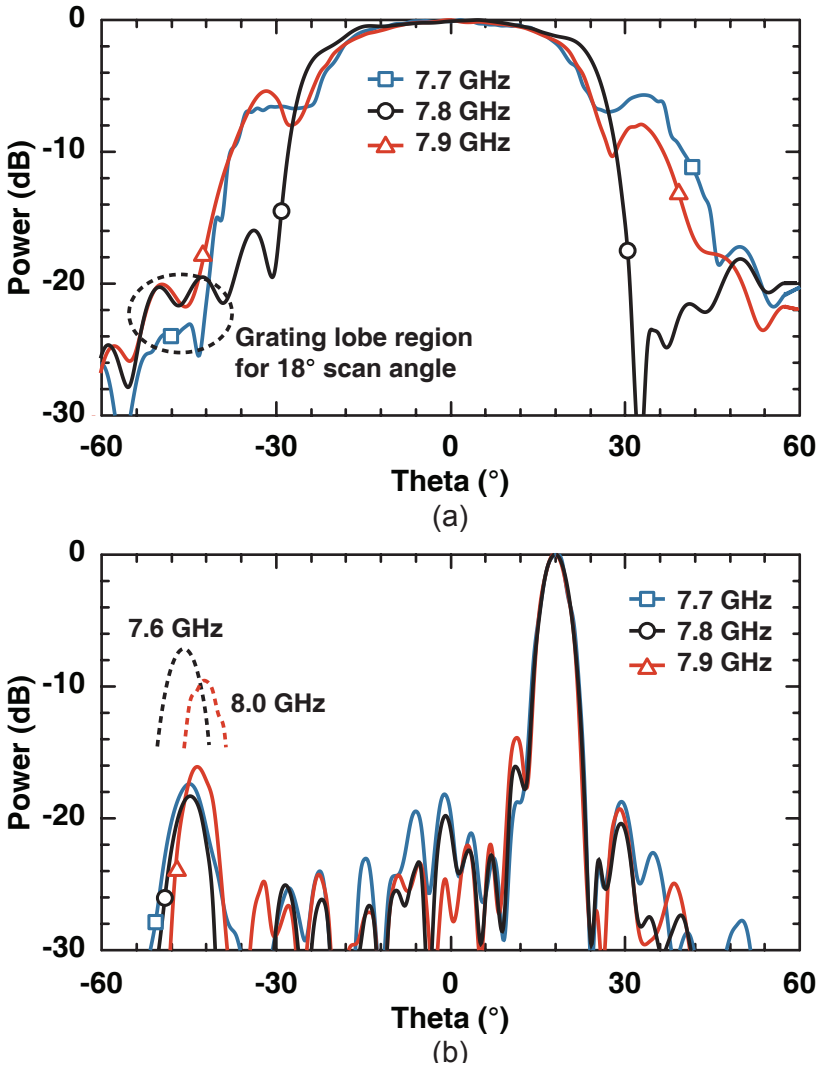

Figure 4.20: (a) Measured element pattern and (b) radiation pattern at $\theta_s = 18^\circ$ scan for the 1:2 interwoven array at different frequencies.

and -30° degrees). However these grating lobes are successfully canceled by the sharp element factor of the interwoven network. The fabricated array can scan $\pm 9^\circ$ while keeping the grating lobes under -12 dB. However after $\pm 9^\circ$, the element pattern start to suppress the main beam and this causes the peak power to drop by approximately 3 dB compared to the 0° scan (Fig. 4.31).

Fig. 4.32 present the normalized measured peak power versus frequency. The 1:4 array has a 2 dB bandwidth of 250 MHz (7.75-8.0 GHz). Similar to the 1:2 array this bandwidth is mainly limited by the array elements (see Fig. 4.9).

Table 4.2 presents the loss breakdown of the 1:4 interwoven array at 7.9 GHz. The total measured loss is 15.4 dB at the broadside and is 16.2 dB at other scan angles, since the phase

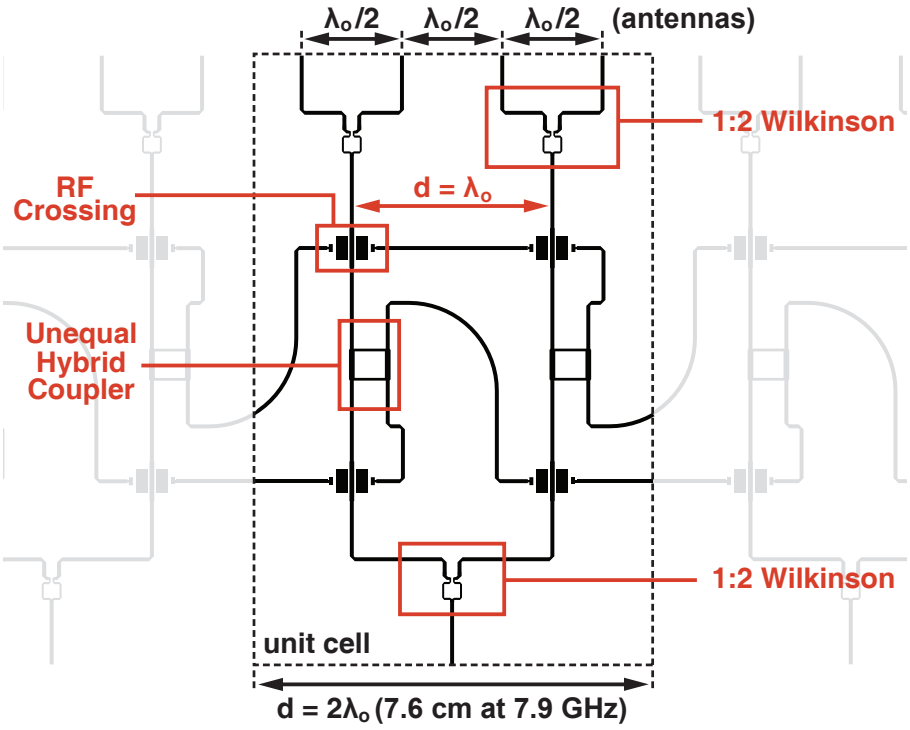

Figure 4.21: The geometry of the 1:4 feeding network board.

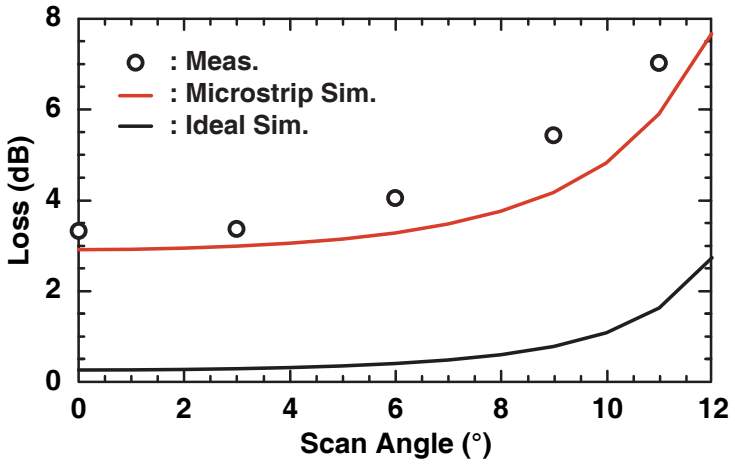

Figure 4.22: Simulated and measured loss of the of the 1:4 feeding network versus scan angle.

shifters are not used at the broadside scan. The measured antenna gain at broadside, referenced to the input power, is 10.5 dB at 7.9 GHz. If the measured loss of 15.4 dB is added to this value, the measured directivity is found to be 25.9 dB. This agrees well with the simulated array directivity of 26.5 dB.

Fig. 4.33(a) presents the measured element pattern for the 28-element 1:4 interwoven array at different frequencies. Similar to the 1:2 array, the extra $2n\pi$ transmission-line sections degrade the element pattern versus frequency. However, up to the $\pm 9^{\circ}$ scan, the element pattern still successfully suppresses the grating lobes (see Fig. 4.33(b)), with a sidelobe level $<$ -10 dB.

4.4.3 Zig-Zag Array Elements

When the output of the standard 1:4 interwoven network is modified as in Fig. 4.21 by adding a Wilkinson divider, an extra array factor ($AF^{*}(\theta) = cos(\pi sin\theta/2)$) is introduced. Even though this additional array factor is required for suppressing the side lobes, the sidelobe levels are still relatively high outside the $\pm 30^{\circ}$ angular region. To further reduce the sidelobe level, the straight antenna elements shown in Fig. 4.9 are replaced with the zig-zag antenna designs (Fig. 4.34). In this case, the element pattern of a single array element on the $\phi = \pi/2$ plane will consist of two microstrip antennas at two different phase centers. This introduces an extra array factor ($AF^{**}(\theta) = cos(\pi sin\,\theta/2)$), which is near unity over the scan region but decreases outside. The measured radiation patterns of the 1:4 interwoven array with zig-zag antennas up to $\pm 11^{\circ}$ is presented in Fig. 4.34(b). As expected, the element pattern of the zigzag antennas successfully reduces the grating lobe levels outside $\pm 30^{\circ}$ region. The scan region up to $\pm 11^{\circ}$ is not affected by the zig-zag antennas and shows the same results as Figs. 4.31-4.33.

4.5 Conclusion

This chapter presented a multi-port passive feeding network that can reduce the number of phase shifters in arrays for limited-scan applications. The feeding network employs power dividers, couplers and attenuators to distribute the output of each phase shifter to all elements of the array. When the components are chosen correctly, a sinc-like current distribution is obtained over the whole array, and current distribution results in a boxcar function-like element pattern which is ideal for canceling the grating lobes outside of the scan region.

Two prototype linear arrays with 28 elements are fabricated to demonstrate the interwoven networks at 7.8-7.9 GHz. Both of these arrays show state-of-the-art performance in terms

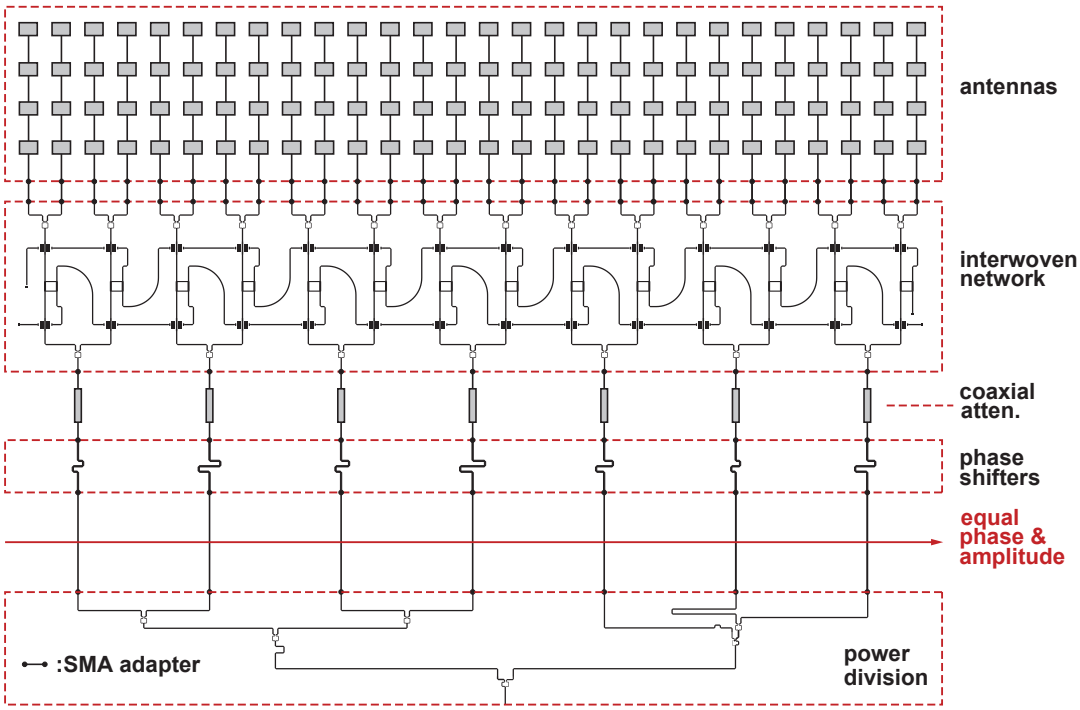

Figure 4.23: Schematic representation of the 1:4 interwoven array at 7.9 GHz.

Table 4.2: Loss of the Fabricated 1:4 Interwoven Array at 7.9 GHz

Part	Loss (dB)
Power divider board	5.6
Attenuators (incl. 6 dB taper)	4.5
Phase shifters	0.8
Interwoven feeding network	3.3
4-Element vertical patch array	2.0
Total loss without phase shifters (0° scan)	15.4
Total loss with phase shifters	16.2

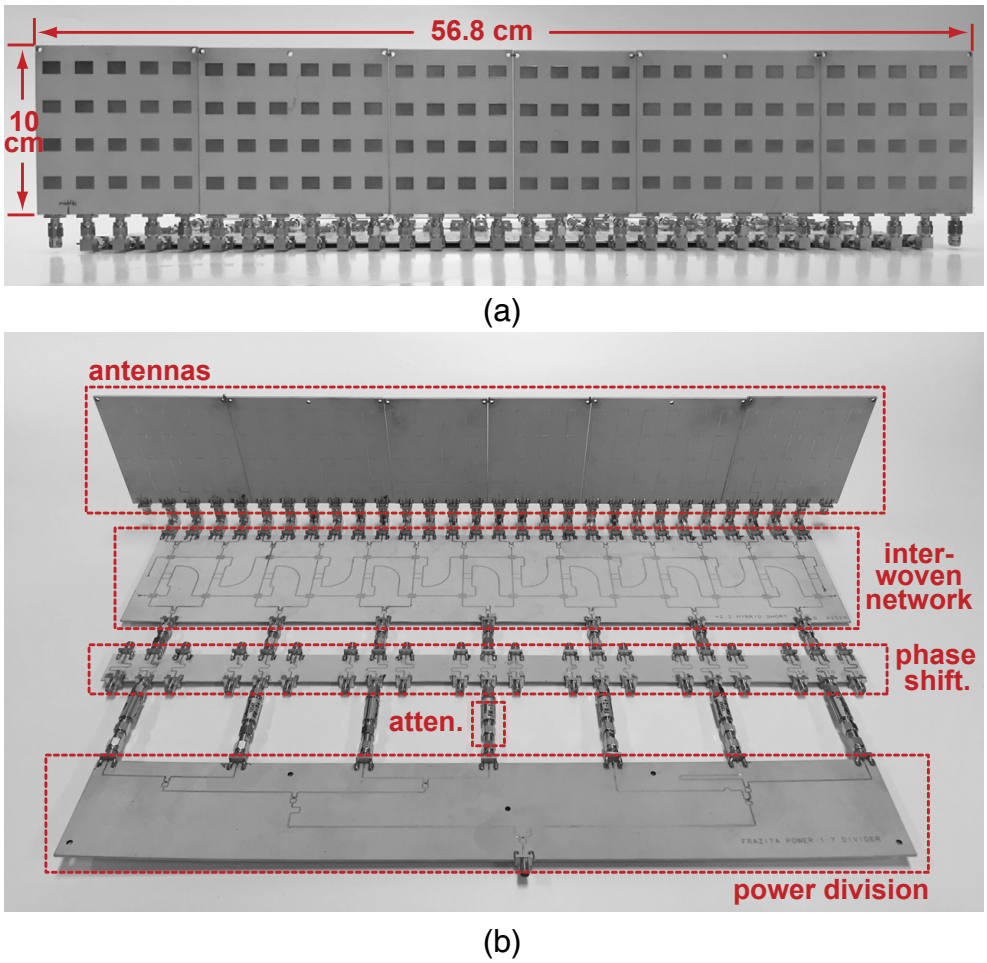

Figure 4.24: Fabricated 1:4 interwoven array with 28 elements: a) front view, b) back view.

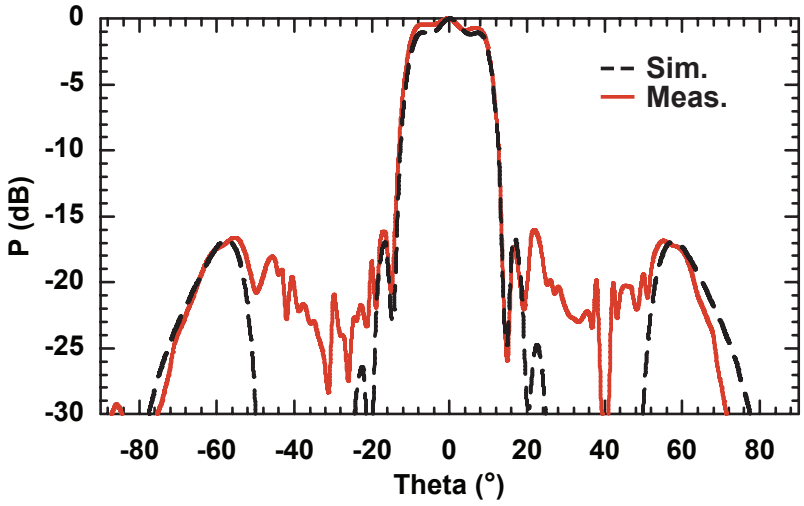

Figure 4.25: Simulated and measured normalized element patterns of the 1:4 array.

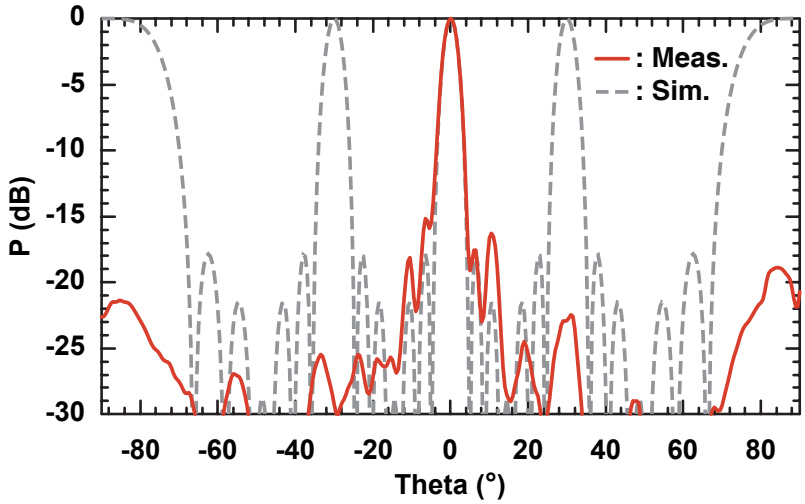

Figure 4.26: Measured radiation pattern of the 1:4 array and the simulated grating lobes without the interwoven feeding networks at 0° scan.

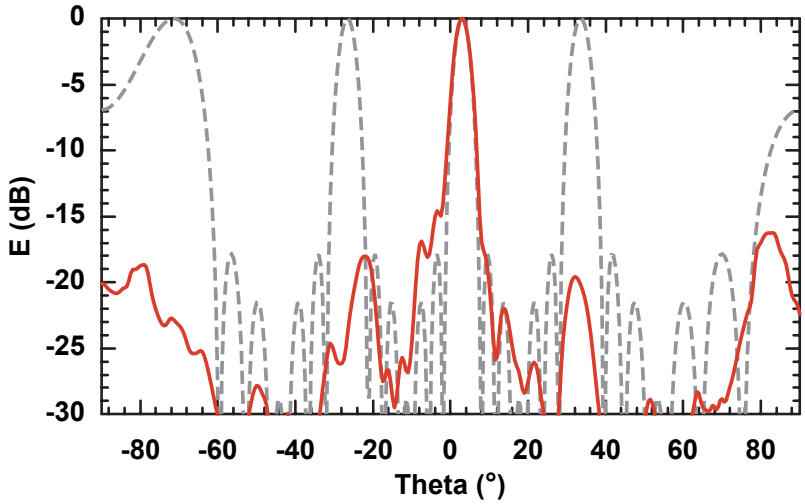

Figure 4.27: Measured radiation pattern of the 1:4 array and the simulated grating lobes without the interwoven feeding networks at 3° scan.

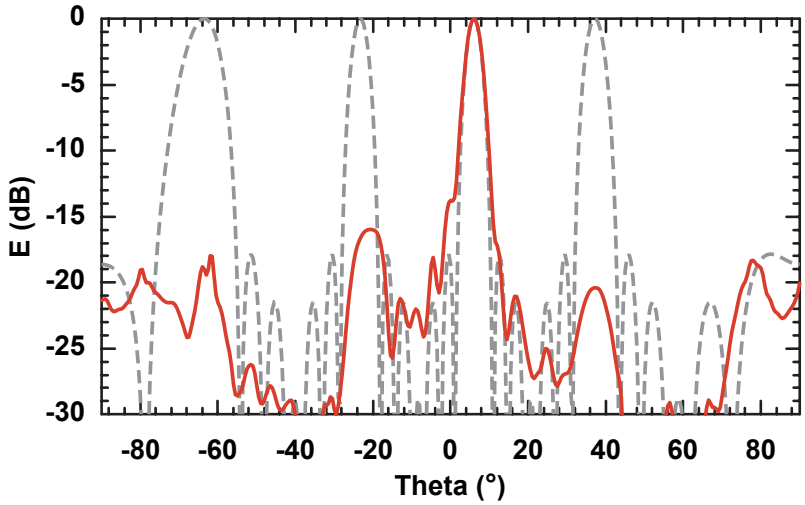

Figure 4.28: Measured radiation pattern of the 1:4 array and the simulated grating lobes without the interwoven feeding networks at 6° scan.

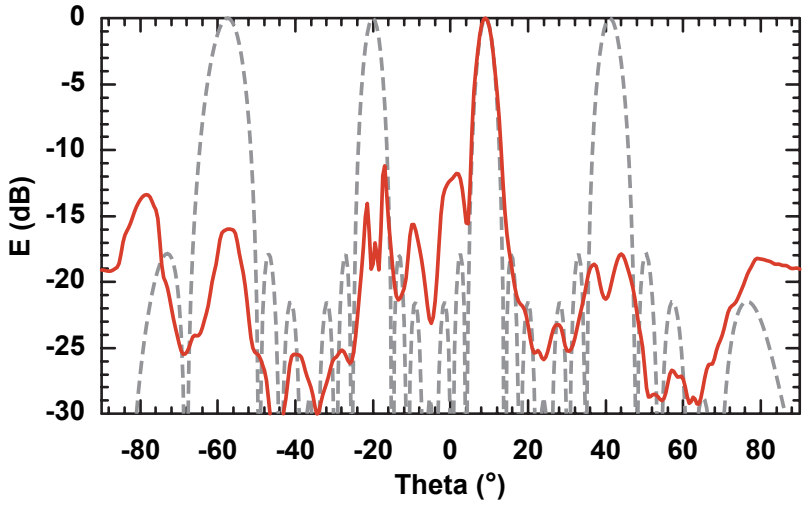

Figure 4.29: Measured radiation pattern of the 1:4 array and the simulated grating lobes without the interwoven feeding networks at 9° scan.

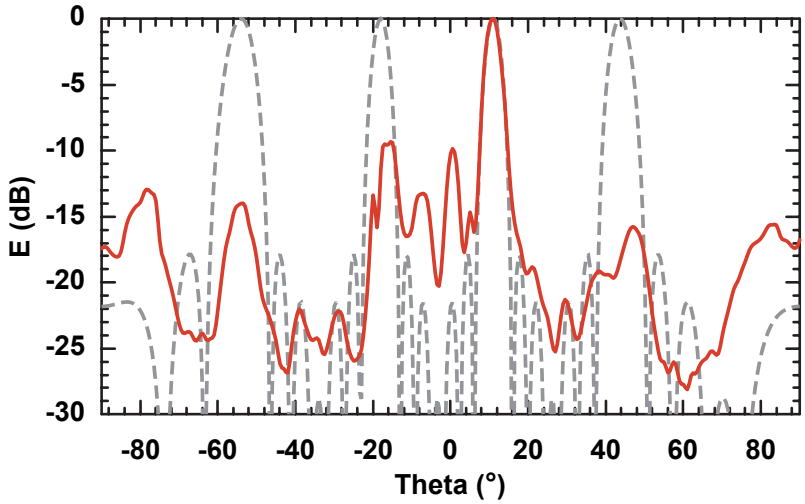

Figure 4.30: Measured radiation pattern of the 1:4 array and the simulated grating lobes without the interwoven feeding networks at 11° scan.

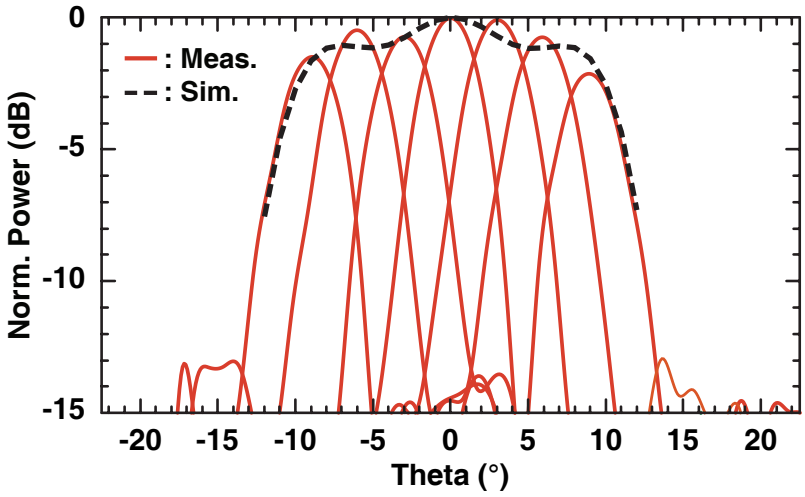

Figure 4.31: Measured array pattern and simulated gain drop of the 1:4 array at 7.9 GHz.

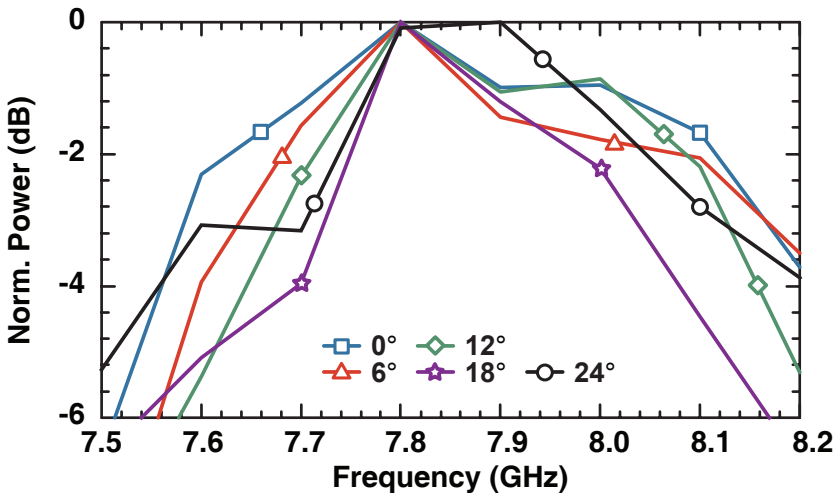

Figure 4.32: Measured normalized peak power of the 1:4 array versus frequency and different scan angles.

of reducing the number of phase shifters while still keeping a low sidelobe level and reducing the effect of the grating lobes. Interwoven arrays present an easily implementable solution for reducing the number of phase shifters in limited-scan arrays. This allows the production of affordable phased-array systems for commercial applications.

4.6 Acknowledgement

This work was supported by Toyota Research Institute of North America, Ann Arbor, Michigan.

Chapter 3 is mostly a reprint of the material as it is submitted for publishing to IEEE Antennas and Propagation, 2015. Bilgehan Avser; Richard Frazita; Gabriel M. Rebeiz. The dissertation author was the primary author of this material.

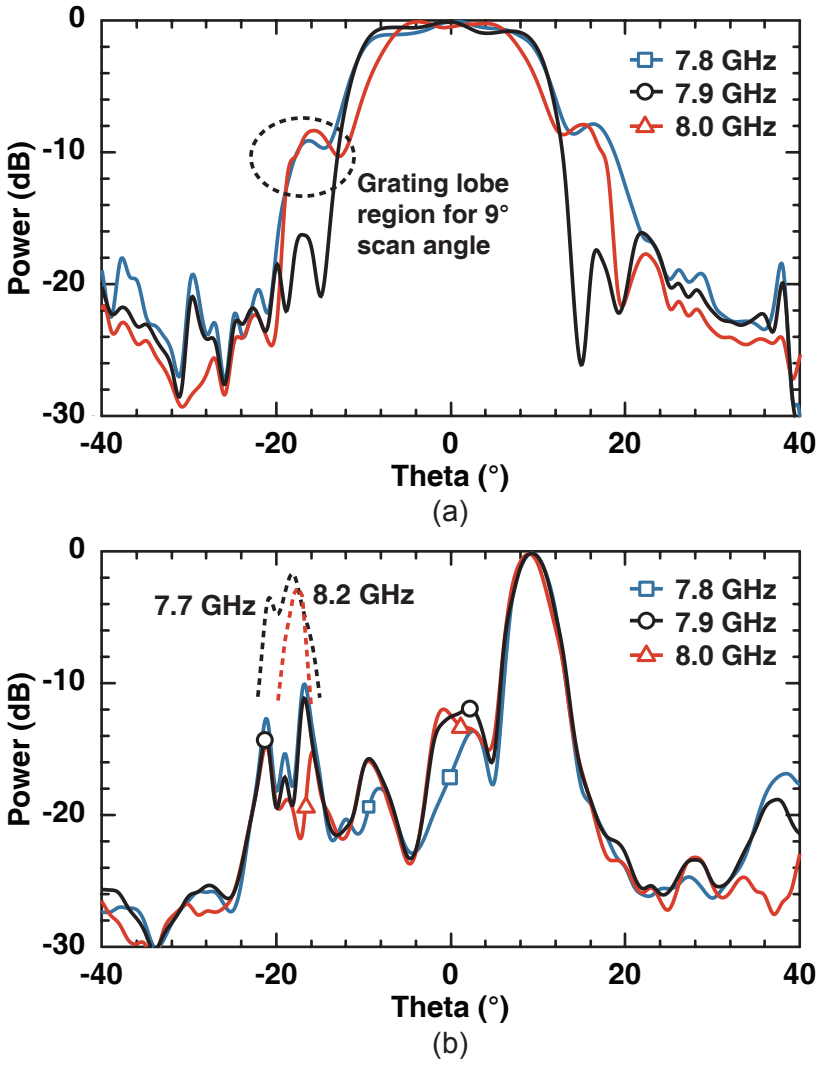

Figure 4.33: (a) Measured element pattern and (b) radiation pattern at $\theta_s = 9°$ for the 1:4 interwoven array at different frequencies.

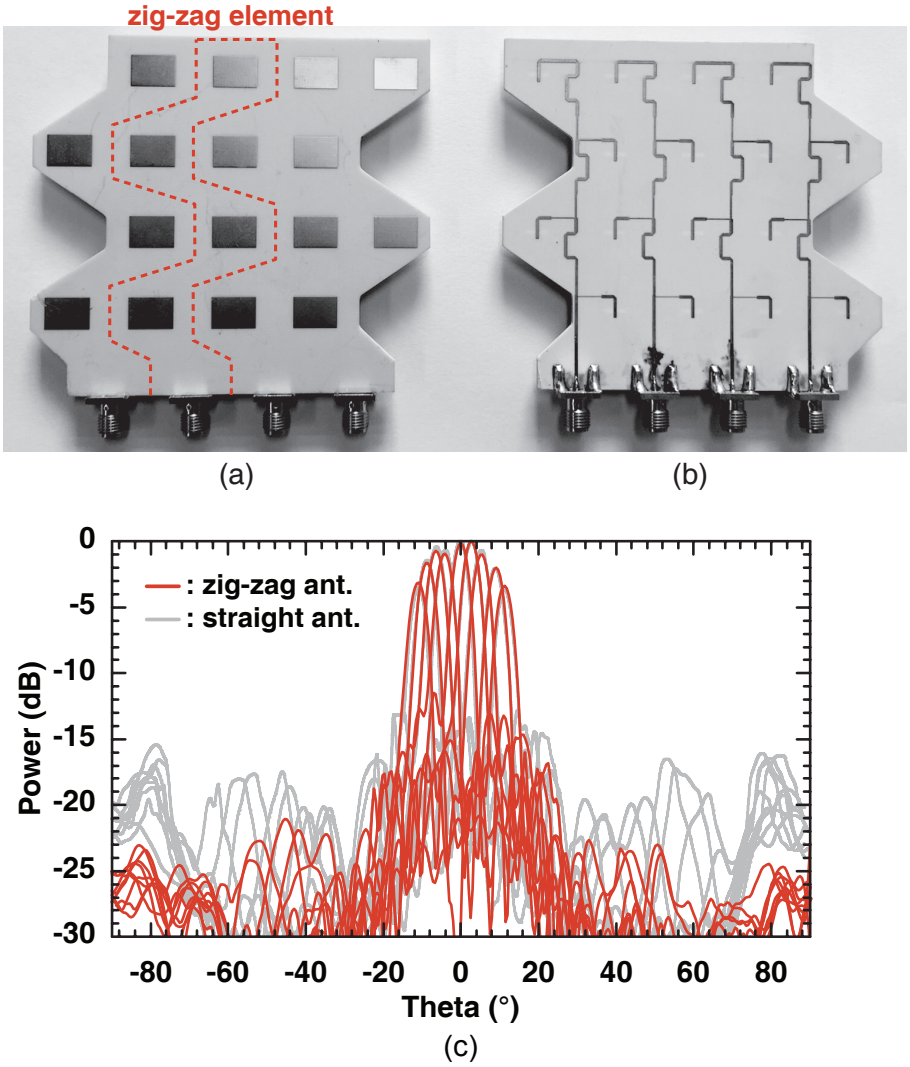

Figure 4.34: Fabricated zig-zag antennas. (a) L1 layer and (b) L2 layer. (c) Measured radiation patterns of the 1:4 array scanning $\pm 11^{\circ}$ with zig-zag antenna elements.

Chapter 5

Conclusion

The thesis presented three dual-band frequency tunable antennas for carrier aggregation systems and two new feeding networks for reducing the number of phase shifters in limited-scan arrays. Single- and dual-feed, dual-frequency, frequency tunable antennas with low-profile are presented in Chapter 2. Varactor diodes with a capacitance range from 0.8 to 3.8 pF are used in series configuration to independently tune the two resonance frequencies (one in each band). The capacitance values of the varactor diodes are compatible with RF MEMS devices. The antenna volumes are $63 \times 100 \times 3.15mm^3$ on $\epsilon_r = 3.55$ substrates. The application areas are in carrier aggregation systems for fourth generation (4G) wireless systems.

A new phased array feeding network that can feed the array elements with less number of phase shifters using random sequences of non-uniform sub-arrays (and a single phase shifter for each sub-array) was presented in Chapter 3. When these sequences are optimized, the resulting phased arrays can scan over a wide region in space with low sidelobe levels. Analysis and design method for random arrays are presented. The performance of the random array feeding scheme is compared to the conventional uniform sub-arraying for multiple cases. It was shown that the number of phase shifters can be reduced up to 30% with the random feeding networks, while the system performance is preserved. The resulting arrays are more affordable and more reliable. The proposed feeding network is demonstrated for a 30 element array of slot-fed patch antennas at 7.9 GHz. The fabricated array uses 12 phase shifters, has a half power beamwidth (HPBW) of 4^o and can scan up to $\pm 14^o$ with sidelobe levels less than -15 dB.

Another phased array feeding network that reduces the number of phase shifters, interwoven feeding network with aperture sinc-distribution, is presented in Chapter 4. This passive feeding network is composed of power dividers, couplers and resistive attenuators and uses each

of the phase shifters to feed all of the array elements. The coupling and attenuation coefficients are chosen to create a sinc-like current distribution over the array elements when the network is fed through a single input. This current distribution results in a boxcar function-like element pattern which lets the main beam to radiate inside the scan-region and suppresses the grating lobes outside. It is possible to adjust the width of the scan region by changing the inter-element spacing and adjusting the network coefficients. Different network configurations along with theoretical limitations are investigated to determine the scanable region, side-lobe level and power loss limits. Two prototype linear arrays with 28 elements are fabricated at 7.9 GHz to demonstrate the concept. The first array employs 14 phase shifters, has a half power beamwidth (HPBW) of 4^o and can scan up to $\pm 24^o$ with sidelobe levels less than -15 dB. The second array uses 7 phase shifters, has a half power beamwidth (HPBW) of 4^o and can scan up to $\pm 11^o$ with sidelobe levels less than -15 dB. Both of these arrays show state-of-the-art performance in terms of reducing the number of phase shifters while still keeping a low sidelobe level and reducing the effect of the grating lobes.

5.1 Future Work

In Chapter 2, dual-band frequency tunable antennas were demonstrated for CA systems. In these implementations, the frequency tuning was achieved using varactor diodes. The Q of the varactor diodes drops significantly when the antennas are tuned to the lower end of the bands. This results in lower antenna efficiency. Furthermore, if a large amount of power is applied to the antennas, the voltage swing on the varactor diodes causes the bias state to shift (Fig. 2.11, Fig. 2.18). This problem can be solved by using RF MEMS devices instead of varactor diodes. The high Q of the RF MEMS devices ($Q \sim 200$) will also increase the efficiency of the antennas significantly (Fig. 2.10, Fig. 2.17).

In Chapter 3, a new phased array feeding network employing random sequences of non-uniform sub-arrays was presented. During the analysis and design of the random arrays the inter-element spacing, D_p, was assumed to be the same for all of the primary arrays. If the optimization process is altered such that different element-spacings are allowed for different primary array groups, random array performance might be increased more. Chapter 3 also presented 2D random arrays that are synthesized using the 1D random array designs. The 2D random arrays can scan in both vertical and horizontal planes with low sidelobe levels. However, the array performance can be further increased if arbitrary 2D primary array groups are allowed to be placed randomly over the array instead of using a grid based on a 1D array.

Bibliography

[1] K. R. Boyle, M. Udink, A. de Graauw, and L. P. Ligthart, "A dual-fed, self-diplexing pifa and rf front-end," *IEEE Trans. Antennas Propag.*, vol. 55, no. 2, pp. 373–382, 2007.

[2] C. R. Rowell and R. D. Murch, "A capacitively loaded PIFA for compact mobile telephone handsets," *IEEE Trans. Antennas Propag.*, vol. 45, no. 5, pp. 837–842, 1997.

[3] Z. D. Liu, P. S. Hall, and D. Wake, "Dual-frequency planar inverted-F antenna," *IEEE Trans. Antennas Propag.*, vol. 45, no. 10, pp. 1451–1458, 1997.

[4] K. L. Virga and Y. Rahmat-Samii, "Low-profile enhanced-bandwidth PIFA antennas for wireless communications packaging," *IEEE Trans. Microw. Theory Techn.*, vol. 45, no. 10, pp. 1879–1888, 1997.

[5] J.-H. Lim, Z.-J. Jin, C.-W. Song, and T.-Y. Yun, "Simultaneous frequency and isolation reconfigurable mimo pifa using pin diodes," *IEEE Trans. Antennas Propag.*, vol. 60, no. 12, pp. 5939–5946, Dec 2012.

[6] R. Caso, A. D'Alessandro, A. Serra, P. Nepa, and G. Manara, "A compact dual-band pifa for dvb-t and wlan applications," *Antennas and Propagation, IEEE Transactions on*, vol. 60, no. 4, pp. 2084–2087, April 2012.

[7] P. J. Soh, G. A. Vandenbosch, S. L. Ooi, and N. H. M. Rais, "Design of a broadband all-textile slotted pifa," *Antennas and Propagation, IEEE Transactions on*, vol. 60, no. 1, pp. 379–384, 2012.

[8] J. Anguera, I. Sanz, J. Mumbru, and C. Puente, "Multiband handset antenna with a parallel excitation of pifa and slot radiators," *Antennas and Propagation, IEEE Transactions on*, vol. 58, no. 2, pp. 348–356, Feb 2010.

[9] G. K. Lui and R. D. Murch, "Compact dual-frequency PIFA designs using LC resonators," *IEEE Trans. Antennas Propag.*, vol. 49, no. 7, pp. 1016–1019, 2001.

[10] H.-T. Chen, K.-L. Wong, and T.-W. Chiou, "PIFA with a meandered and folded patch for the dual-band mobile phone application," *IEEE Trans. Antennas Propag.*, vol. 51, no. 9, pp. 2468–2471, 2003.

[11] D. F. Sievenpiper, D. C. Dawson, M. M. Jacob, T. Kanar, S. Kim, J. Long, and R. G. Quarfoth, "Experimental validation of performance limits and design guidelines for small antennas," *IEEE Trans. Antennas Propag.*, vol. 60, no. 1, pp. 8–19, 2012.

[12] P. Panayi, M. Al-Nuaimi, and L. Ivrissimtzis, "Tuning techniques for the planar inverted-F antenna," in *Antennas and Propagat., 1999. IEE National Conference on.*, vol. 52, no. 11, April 1999, pp. 259–262.

[13] N. C. Karmakar, "Shorting strap tunable stacked patch PIFA," *IEEE Trans. Antennas Propag.*, vol. 52, no. 11, pp. 2877–2884, 2004.

[14] N. C. Karmakar, L. Firmansyah, and P. Hendro, "Tunable PIFA using low cost band switch diodes," in *IEEE Antennas Propagat. Soc. Int Symp. San Antonio, TX, July 2002*, vol. 4, pp. 516–519.

[15] J.-H. Park, Y.-D. Kim, Y.-H. Park, H.-C. Lee, H. Kwon, H.-J. Nam, and J.-U. Bu, "Tunable planar inverted-F antenna using rf MEMS switch for the reduction of human hand effect," in *Proc. IEEE Int. MEMS Conf., Jan. 2007*, pp. 163–166.

[16] S.-K. Oh, H.-S. Yoon, and S.-O. Park, "A PIFA-type varactor-tunable slim antenna with a PIL patch feed for multiband applications," *Antennas and Wireless Propagation Letters, IEEE*, vol. 6, pp. 103–105, 2007.

[17] iFixit, "Samsung Galaxy S5 teardown." [Online]. Available: http://www.ifixit.com/Teardown/Samsung+Galaxy+S5+Teardown/24016

[18] ——, "iPhone 5 teardown." [Online]. Available: http://www.ifixit.com/Teardown/iPhone+5+Teardown/10525

[19] ——, "HTC One (M8) teardown." [Online]. Available: http://www.ifixit.com/Teardown/HTC+One+(M8)+Teardown/23615

[20] G. Yuan, X. Zhang, W. Wang, and Y. Yang, "Carrier aggregation for LTE-advanced mobile communication systems," *IEEE Commun. Mag.*, vol. 48, no. 2, pp. 88–93, 2010.

[21] M. Iwamura, K. Etemad, M.-H. Fong, R. Nory, and R. Love, "Carrier aggregation framework in 3GPP LTE-advanced [WiMAX/LTE Update]," *IEEE Commun. Mag.*, vol. 48, no. 8, pp. 60–67, 2010.

[22] K. I. Pedersen, F. Frederiksen, C. Rosa, H. Nguyen, L. G. U. Garcia, and Y. Wang, "Carrier aggregation for LTE-advanced: functionality and performance aspects," *IEEE Commun. Mag.*, vol. 49, no. 6, pp. 89–95, 2011.

[23] G. Rebeiz and K.-J. Koh, "Silicon RFICs for phased arrays," *Microwave Magazine, IEEE*, vol. 10, no. 3, pp. 96–103, May 2009.

[24] Advanced Design System, Agilent Technologies, Santa Clara, CA, 2002.

[25] IED3 7.0, Zeland Software Inc., TX, USA.

[26] E. Brookner, "Phased-array radars," *Scientific American*, vol. 252, no. 2, pp. 94–102, 1985.

[27] S. Y. Kim and G. M. Rebeiz, "A low-power bicmos 4-element phased array receiver for 76–84 ghz radars and communication systems," *Solid-State Circuits, IEEE Journal of*, vol. 47, no. 2, pp. 359–367, 2012.

[28] C. S. Anselmo, S. W. Houston, and D. P. Sullivan, "Method and system for communicating high rate data in a satellite-based communications network," Sep. 26 2000, uS Patent 6,125,261.

[29] B.-H. Ku, O. Inac, M. Chang, and G. M. Rebeiz, "75–85 ghz flip-chip phased array rfic with simultaneous 8-transmit and 8-receive paths for automotive radar applications," in *Radio Frequency Integrated Circuits Symposium (RFIC), 2013 IEEE*. IEEE, 2013, pp. 371–374.

[30] M. Schneider, "Automotive radar–status and trends," in *German microwave conference*, 2005, pp. 144–147.

[31] S. Tokoro, K. Kuroda, A. Kawakubo, K. Fujita, and H. Fujinami, "Electronically scanned millimeter-wave radar for pre-crash safety and adaptive cruise control system," in *Intelligent Vehicles Symposium, 2003. Proceedings. IEEE*. IEEE, 2003, pp. 304–309.

[32] HFSS. ANSYS, Inc., Pittsburgh, PA, 2008.

[33] S. Zhang, S. N. Khan, and S. He, "Reducing mutual coupling for an extremely closely-packed tunable dual-element PIFA array through a resonant slot antenna formed in-between," *IEEE Trans. Antennas Propag.*, vol. 58, no. 8, pp. 2771–2776, 2010.

[34] SATIMO Corporate, France. [Online]. Available: http://www.satimo.com/

[35] C. R. White and G. M. Rebeiz, "Single-and dual-polarized tunable slot-ring antennas," *IEEE Trans. Antennas Propag.*, vol. 57, no. 1, pp. 19–26, 2009.

[36] WiSpry, Inc., Irvine, CA. [Online]. Available: http://www.wispry.com/

[37] Cavendish Kinetics, Inc., San Jose, CA. [Online]. Available: http://www.cavendish-kinetics.com/

[38] M. Okoniewski and M. A. Stuchly, "A study of the handset antenna and human body interaction," *IEEE Trans. Microw. Theory Techn.*, vol. 44, no. 10, pp. 1855–1864, 1996.

[39] L. Bui, D. Uecker, E. Loose, and Y. Alon, "Test results of an experimental autonomous aircraft landing system utilizing a 94 ghz fm-cw imaging radar," in *IEEE MTT-S Int. Microw. Symp, Atlanta, GA, June 1993*. IEEE, 1993, pp. 857–860.

[40] L. Q. Bui, M. R. Franklin, C. Taylor, and G. Neilson, "Autonomous landing guidance system validation," in *AeroSense'97*. International Society for Optics and Photonics, 1997, pp. 19–25.

[41] J. Nemit, "Network approach for reducing the number of phase shifters in a limited scan phased array," Apr. 9 1974, uS Patent 3,803,625.

[42] R. J. Mailloux, "A low-sidelobe partially overlapped constrained feed network for time-delayed subarrays," *Antennas and Propagation, IEEE Transactions on*, vol. 49, no. 2, pp. 280–291, 2001.

[43] R. Fante, "Systems study of overlapped subarrayed scanning antennas," *IEEE Trans. Antennas Propag.*, vol. 28, pp. 668–679, 1980.

[44] R. J. Mailloux, "A low-sidelobe partially overlapped constrained feed network for time-delayed subarrays," *IEEE Trans. Antennas Propag.*, vol. 49, no. 2, pp. 280–291, 2001.

[45] S. M. Duffy, F. Willwerth, L. Retherford, and J. S. Herd, "Results of x-band electronically scanned array using an overlapped subarray architecture," in *Phased Array Systems and Technology (ARRAY), 2010 IEEE International Symposium on*. IEEE, 2010, pp. 713–718.

[46] A. Abbaspour-Tamijani and K. Sarabandi, "An affordable millimeter-wave beam-steerable antenna using interleaved planar subarrays," *IEEE Trans. Antennas Propag.*, vol. 51, no. 9, pp. 2193–2202, 2003.

[47] S. P. Skobelev, "Methods of constructing optimum phased-array antennas for limited field of view," *Antennas and Propagation Magazine, IEEE*, vol. 40, no. 2, pp. 39–50, 1998.

[48] R. F. Frazita, A. R. Lopez, and R. J. Giannini, "Limited scan array antenna systems with sharp cutoff of element pattern," Aug. 9 1977, uS Patent 4,041,501.